

國立臺灣大學理學院大氣科學研究所



碩士論文

Department of Atmospheric Sciences

College of Science

National Taiwan University

Master Thesis

2021 年 6 月 4 日臺北午後對流個案之系集預報研究

Ensemble Prediction of the

Afternoon Thunderstorm System at Taipei on 4 June 2021

余世暘

Shih-Yang Yu

指導教授：楊明仁 博士

Advisor: Ming-Jen Yang Ph.D.

中華民國 111 年 7 月

July, 2022



國立臺灣大學碩士學位論文
口試委員會審定書

本論文係余世暘君（學號 R09229011）在國立臺灣大學大氣科學學系、所完成之碩士學位論文，於民國 111 年 7 月 20 日承下列考試委員審查通過及口試及格，特此證明

口試委員：

楊明仁

（簽名）

（指導教授）

陳正午

王重光

郭鴻基

游政吉

系主任、所長

（簽名）

誌謝



兩年的碩士時光轉瞬即逝，但留下許多生活中的寶藏。能從大學所讀的土木工程跨足進入大氣科學，並在超乎我預期的時間內完成碩士學業，首先當感謝我的指導教授楊明仁老師，在我當初僅懷抱對大氣的熱忱而缺乏實質訓練時，包容並接納我進入這嶄新的領域，除了在專業知識的教導外，也在我研究上偏向「解決問題」的工程思維下，領導我如何兼容「探究原因」的科學思考模式，使我在遇到問題時，能有更完善的思路；老師在研究上的審慎且踏實的態度，也使我在研究過程中能始終抱持正確的學術觀念。

接著我要感謝口試委員郭鴻基老師、陳正平老師以及王重傑老師，謝謝三位老師的鼓勵以及在研究上寶貴的建議，使論文內容能更加完整且詳盡。

感謝對流與降水實驗室的夥伴們，讓我在大氣研究以及碩士班生活的路上能夠更加順利且多彩：教我本來完全看不懂的 WRF 的曜竹學長、給予轉換跑道的我許多鼓勵的偉庭學長、教我天氣分析及進入風迷思維的茂正學長、在研究上給予許多建議及交流想法的炯恩學長、在處理資料和程式計算上給予許多幫助的尚恩學長、在生活及未來規劃上互相交換意見的玉來學長、一起在學業和生活上努力的若瑜、以及每天講五四三舒緩我壓力的詣軒。

感謝土木工程系的兄弟們：幾乎天天吃飯一起做事分享生活的柏志、懂得如何開心過生活的翌鈞、世界第一大暖男梁維、一學期見一次但感情依然好的奕達、離開學校仍然關心我的杰祺、以及受過教育的柏硯。

感謝我的家人，在我忙碌的碩士生涯中包容接納我的情緒以及寥寥可數回家次數，讓我無後顧之憂地繼續向前邁進。

最後，感謝世暘，你努力完成了曾經的夢想。



摘要

短延時強降雨為使臺北都會區淹水的主要因子之一。2021年6月4日的梅雨鋒前午後對流事件，於臺北盆地東南側降下破百毫米的時雨量，使都市排水系統宣洩不及，造成多處淹水。本研究透過系集預報模式進行分析，欲了解不同模式設定對於事件中各個重要物理過程的影響。系集預報系統由兩種初始邊界條件、四種積雲參數法、以及四種微物理參數法組成32個系集成員，欲探討的對象則由綜觀環境至中尺度過程，最後探討定量降雨預報結果。

在綜觀環境方面，北側海面的梅雨鋒面非常接近臺灣，因此本個案並非弱綜觀環境下的午後對流事件，雖然觀測資料顯示當天臺北盆地的風場仍由局部環流主導，但梅雨鋒面於模式中的南移速度可能影響降雨型態。研究結果顯示，地面梅雨鋒面位置主要為初始場主導，ECMWF系集成員的鋒面移速偏慢，而NCEP成員的移速偏快，臺灣北部陸地周邊的水氣、溫度受鋒面位置的差異影響，使對流發展時的ECMWF成員環境較為暖濕、NCEP成員較為冷乾。

中尺度的物理過程除了探討日間輻射加熱之外，亦參考Jou (1994)及Miao and Yang (2020)的研究，著重分析日間淡水河海風帶來的水氣以及對流肇始後的冷池行為。日間短波輻射加熱對於盆地上空的高雲雲量敏感，因此主要由微物理參數法主導，高雲含量過多的Morrison參數法使該組系集成員的加熱時序較其他成員晚約一個小時，此系集差異向下傳遞至由海陸加熱對比造成的海風，Morrison參數法系集成員中的海風亦較其他系集成員延遲約一個小時。冷池方面，除了Morrison參數法的整體時間延遲之外，初始場所帶來的環境差異亦顯著影響。ECMWF成員的環境暖濕，有利於冷池發展，因此冷池於對流前緣沿著雪山山脈下山，並於臺北盆地內部與海風輻合，激發顯著的對流訊號；相對的，NCEP成員的環境冷乾，不利冷池發展，其訊號僅在山區強降雨區出現，因此對流胞發展侷限於雪山山脈上。

系集降雨預報的校驗則透過Fractions Skill Score (FSS; Roberts and Lean 2008)和Method for Object-Based Diagnostic Evaluation (MODE; Davis et al. 2006)兩種方



法進行分析。FSS 校驗結果顯示，雖然模式的水平解析度高達 1 公里，其能有效給予的降雨資訊僅介於 1 公里至 21 公里，為對流在空間上的不確定性所造成。FSS 的三種衍生指數 (dFSS, eFSS, 及 LFSS) 指出：系集在 1 公里解析度時的降雨區域發散程度不足，因大部分雨量都集中於雪山山脈山區，此現象亦透過 MODE 校驗可見，模式降雨中心由臺北盆地向東南側的山區偏離 2 至 27 公里。

最後由層次聚類法 (Hierarchical Clustering) 分析 32 組降雨結果的相關性，降雨結果主要由初始場主導，而積雲參數法及微物理參數法則在此框架下提供更高的多樣性，此分析結果與前述的物理過程相符。

關鍵字：臺北午後對流、系集預報、淡水河谷海風、冷池、降雨校驗

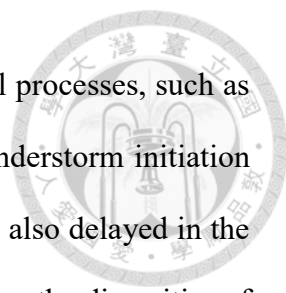
Abstract



The short-duration high-intensity precipitation is one of the factors that can cause the inundation in the Taipei urban area. On 4 June 2021, an afternoon thunderstorm happened, and the rainfall intensity exceeded 100 mm/hour in the southeast corner of the city, causing severe flooding in the urban area. In this study, an ensemble prediction was conducted to figure out the factors in the model that affected the physical processes in this event. The ensemble members were established by the variations of two initial conditions, four cumulus parameterizations, and four microphysics schemes. The physical processes analyzed included the synoptic environment, mesoscale processes, and the resulting precipitation.

For the synoptic conditions, the Mei-Yu front was about 50 km to 100 km offshore of northern Taiwan, so this event cannot be considered “weak synoptic.” Instead, the Mei-Yu front in the numerical model might influence the event even though the local circulation dominated the area based on the observation. Results showed that the initial conditions mainly determined the location of the surface Mei-Yu front in the model. The fronts in the ECMWF members moved southward slower, while those in the NCEP members moved faster. Therefore, the surface environment near northern Taiwan differed between these two groups. The ECMWF members tended to be warmer and wetter, but the NCEP members were cooler and drier during the development of the thunderstorms.

According to the previous studies (Jou 1994; Miao and Yang 2020), the main focuses of the mesoscale processes included the solar heating in the morning, the sea breeze along the Tamsui River Valley (TRV), and the thunderstorm cold pool. The solar heating in the morning was sensitive to the high cloud pattern. Therefore, the microphysics schemes mainly dominated this process. The Morrison scheme tended to produce too many upper-level hydrometeors, so the heating timing was about one hour later than other schemes.

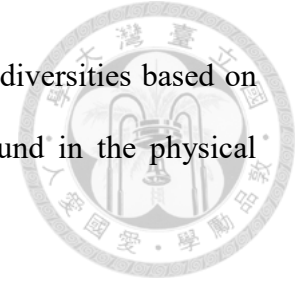


This ensemble spread would be transported to the following physical processes, such as the sea breeze induced by the land-sea heating contrast and the thunderstorm initiation time. The detection time of the resulting thunderstorm cold pool was also delayed in the Morrison members. However, in addition to the microphysics schemes, the diversities of initial conditions influenced the characteristics of the thunderstorm cold pool. The synoptic environment in ECMWF members was warmer and wetter, which was favorable for developing cold pools. The cold pool in these members propagated downslope from the Snow Mountain Range (SMR) to the Taipei Basin, converging with the sea breeze and causing heavy rainfall in the plain area. In contrast, the synoptic environment of NCEP members was cooler and drier, which inhibited the intensity of the cold pool and was unfavorable for triggering new convection in the basin. The resulting rainfall was therefore concentrated in the mountainous area.

The verification of the ensemble quantitative precipitation forecast (QPF) was evaluated by the fractions skill score (FSS; Roberts and Lean 2008) and the method for object-based diagnostic evaluation (MODE; Davis et al. 2006). The results of FSS showed that although the finest horizontal resolution was up to 1 km, the informative spatial scale could range from 1 km to 21 km, which was brought about by the intrinsic spatial uncertainty of the afternoon thunderstorm in the numerical model. The three FSS derivatives (dFSS, eFSS, and LFSS) indicated that the spatial distribution of the precipitation area was underspread under the highest resolution (i.e., 1 km). The rainfall areas were mainly concentrated on the SMR, and the MODE method also pointed out this systematic bias with the distance from 2 km to 27 km.

Last, the hierarchical clustering technique was applied to the 6-hour precipitation between 12 LST and 18 LST to understand the relationship between the ensemble members. The initial conditions mainly dominated the rainfall pattern, while the cumulus

schemes and the microphysics parameterizations further added the diversities based on this background. These results were consistent with what was found in the physical processes analyses.



Key words: Taipei afternoon thunderstorm; ensemble prediction; Tamsui River Valley sea breeze; thunderstorm cold pool; QPF verification

Table of Contents



國立臺灣大學碩士學位論文口試委員審定書	i
誌謝	ii
摘要	iii
Abstract.....	v
Table of Contents.....	viii
List of Tables	x
List of Figures.....	xi
Chapter 1. Introduction	1
Chapter 2. Data and Methods	7
2.1 Observation	7
2.2 Model Configuration.....	8
2.3 Analyses of Physical Processes.....	9
2.3.1 Synoptic Mei-Yu Front	9
2.3.2 Sea Breeze	10
2.3.3 Thunderstorm Cold Pool.....	10
2.4 Verification Methods for Quantitative Precipitation Forecast (QPF).....	11
2.4.1 Fractions Skill Score (FSS)	11
2.4.2 Three Derivatives of FSS.....	15
2.4.3 Method for Object-based Diagnostic Evaluation (MODE).....	18
Chapter 3. Case Overview	20
3.1 Synoptic Environment.....	20
3.2 Evolution of the Thunderstorms.....	22
3.3 Mesoscale Processes	23
Chapter 4. Ensemble Member E17	25



4.1 Synoptic Environment around Northern Taiwan	25
4.2 Evolution of the Thunderstorms.....	27
4.3 Mesoscale Processes	29
Chapter 5. Ensemble Performance of the Physical Processes	32
5.1 Synoptic Environment.....	32
5.2 Solar Heating and Sea Breeze in the Morning.....	36
5.3 Thunderstorm Cold Pool.....	38
Chapter 6. Verification on Quantitative Precipitation Forecast (QPF).....	41
6.1 Fractions Skill Score and its Derivatives	41
6.1.1 Fractions Skill Score (FSS)	41
6.1.2 Ensemble-aggregated FSS (eFSS) and Dispersion FSS (dFSS).....	45
6.1.3 Localized FSS (LFSS)	46
6.2 Method for Object-based Diagnostic Evaluation (MODE)	47
6.2.1 Identifying and Pairing the Areas	47
6.2.2 Errors of the Geometric Characteristics	48
6.2.3 Errors of Rainfall Intensity	50
6.3 Hierarchical Clustering	52
Chapter 7. Conclusions and Recommendations for Future Work.....	54
7.1 Conclusions.....	54
7.2 Recommendations for Future Work.....	57
Reference	59
Tables.....	63
Figures	65

List of Tables

Table 2.1 The configurations of all 32 ensemble members.	63
Table 6.1 The skillful spatial scale of each ensemble member between 12 LST and 18 LST under the threshold of 30 mm/6hr aligned (a) in sequence and (b) by rank.....	64





List of Figures

Figure 1.1 Schematic diagram of the crucial mesoscale mechanisms for Taipei afternoon thunderstorm initiation and development along the Tamsui River Valley (TRV). (Miao and Yang 2020)	65
Figure 1.2 Two major categories and four minor classes of the QPF verification methods. (Gilleland et al. 2009).....	65
Figure 2.1 The locations of RCWF and RCSL radars (red polygons), Banqiao station (green polygon), CWB surface stations (brown dots), and automatic weather stations (blue dots). The blue box shows the area of the Taipei Basin.....	66
Figure 2.2 Four two-way nested domains of the model.	66
Figure 2.3 (a) 6-hour gauge-corrected QPE from 12 LST to 18 LST with (b) the corresponding binary field under the threshold of 30 mm/6hr.	67
Figure 2.4 The FSS curve. (Roberts and Lean 2008)	68
Figure 2.5 The FSS of 6-hour accumulated precipitation from 08 LST to 20 LST with the spatial scale between 1 km and 150 km in ensemble member E01.....	68
Figure 2.6 The histogram of FSSave.....	69
Figure 3.1 The JMA surface weather chart at 08 LST (00 UTC) on 4 June 2021.	69
Figure 3.2 The Himawari-8 visible satellite images around Taiwan from 08 LST to 17 LST with 3-hour intervals.	70
Figure 3.3 The identified observational surface Mei-Yu front at 08 LST (blue line), 11 LST (orange line), and 14 LST (green line).	70
Figure 3.4 Himawari-8 infrared (top half) and visible (bottom half) satellite images at 08 LST (left half) and 11 LST (right half) with the domain of east Asia (subplots a., b., e., and f.) and Taiwan (subplots c., d., g., and h.).	71

Figure 3.5 Banqiao sounding (46692) at 08 LST (00 UTC) with the lifting curve of 08 LST (00 UTC; black line) and 12 LST (04 UTC; purple line).....	72
Figure 3.6 The hourly Shulin composite radar reflectivity from 12 LST to 19 LST.....	73
Figure 3.7 The hourly gauge-corrected QPE from 12 LST to 20 LST.	74
Figure 3.8 The 6-hour gauge-corrected QPE and the surface gauge observation from 12 LST to 18 LST.....	75
Figure 3.9 The definition of Tamsui River Valley (TRV; red box), Taipei Basin (blue box), and six CWB stations along the TRV (brown dots). The shading shows the topography.....	75
Figure 3.10 The time series of 10-m wind (barbs) and 2-m water vapor mixing ratio (color) at six TRV stations from 08 LST to 13 LST.	76
Figure 3.11 The time series of 10-m wind (barbs), 2-m temperature (red lines), and pressure (black lines) at six TRV stations from 08 LST to 17 LST.	77
Figure 4.1 The 10-m wind (barbs), 10-m vorticity (color), and the corresponding surface Mei-Yu front (red line) in ensemble member E17 at (a) 08 LST, (b) 11 LST, and (c) 14 LST. The black dashed lines show the location of observational frontal line.....	78
Figure 4.2 (a) The 1° by 1° box at northern Taiwan Strait. (b) The time series of averaged 10-m wind, 2-m temperature, and 2-m water vapor mixing ratio in the 1° by 1° box of ensemble member E17.....	79
Figure 4.3 The cloud top temperature of ensemble member E17 at (a) 08 LST and (b) 11 LST.	80
Figure 4.4 The time-height plot of the cloud fraction in ensemble member E17 over Taipei Basin.....	81

Figure 4.5 The time series of 2-m temperature from ensemble member E17 (blue) and observation (red) at three stations (Banqiao, Taipei, and National Taiwan University) in Taipei Basin from 08 LST to 17 LST.....	81
Figure 4.6 The maximum reflectivity and 10-m wind field in ensemble member E17 from 10 LST to 18 LST with 30-minute intervals.....	82
Figure 4.7 The hourly rainfall in ensemble member E17 from 10 LST to 18 LST.	83
Figure 4.8 The 6-hour accumulated precipitation of ensemble member E17 from 12 LST to 18 LST.....	84
Figure 4.9 The 2-m water vapor mixing ratio (color) and 10-m wind (barbs) of ensemble member E17 from 08 LST to 15 LST with hourly intervals.	85
Figure 4.10 The equivalent potential temperature (black contours), wind parallel to the cross section (arrows), cold pool (blue lines), and radar reflectivity higher than 35 dBZ (red contours) along the Tamsui River Valley (TRV) from 10 LST to 18 LST. The subplots show the plain view of the 10-m wind (arrows), the radar reflectivity (shading), the area of Taipei Basin (blue box), and the cross section of TRV (red box).	86
Figure 4.11 The Hovmöller diagrams of cold pool thickness (blue contours) with the color shading of (a) 10-m wind parallel to the cross section and (b) maximum radar reflectivity along the Tamsui River Valley from 08 LST to 20 LST. The subplots under each diagram show the topography.	87
Figure 5.1 The flow chart and relationships between (a) synoptic environment, (b) mesoscale processes, and (c) precipitation in this event.	88
Figure 5.2 The surface Mei-Yu fronts of observation (black), NCEP members (green), ECMWF members (blue), and ensemble mean (yellow) at (a) 08 LST, (b) 11 LST, (c) 14 LST, and (d) 17 LST. The color shading shows the spread of one standard deviation. .	89

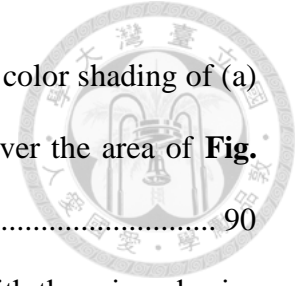


Figure 5.3 The time series of ensemble 10-m wind (barbs) with the color shading of (a) 2-m temperature and (b) 2-m water vapor mixing ratio averaged over the area of **Fig. 4.2(a)** from 08 LST to 13 LST. 90

Figure 5.4 Ensemble cloud top temperature at 08 LST (00 UTC) with the microphysics scheme used in each member..... 91

Figure 5.5 Ensemble vertical profile of averaged cloud fraction between 08 LST and 10 LST in Taipei Basin..... 92

Figure 5.6 (a) The grids lower than 100 meters in Taipei Basin. (b) Ensemble time series of averaged 2-m temperature over the grids of (a) from 08 LST to 20 LST. 93

Figure 5.7 The time series of averaged 2-m temperature in the members of WDM6 (yellow), Goddard (green), Thompson (blue), and Morrison (purple) microphysics schemes. The domain is the same as **Fig. 5.6 (a)**. 94

Figure 5.8 The first detection time of sea breeze along the TRV in each member. 94

Figure 5.9 The first detection time of (a) the convective cell (>45 dBZ) and (b) the induced thunderstorm cold pool along TRV in each member..... 95

Figure 5.10 (a) The occurrence of cold pool (detected every 30 minutes) and (b) the maximum cold pool thickness along TRV between 08 LST and 20 LST..... 96

Figure 6.1 The FSS of 6-hour rainfall in E17 from 08 LST to 20 LST under the threshold of 30 mm/6hr and the spatial scale of 1 km to 141 km. 97

Figure 6.2 Ensemble 6-hour precipitation from 12 LST to 18 LST..... 98

Figure 6.3 Ensemble FSS curves and the corresponding FSSuniform (0.59) for the 6-hour precipitation between 12 LST and 18 LST under the threshold of 30 mm/6hr. 99

Figure 6.4 The histogram of skillful spatial scales in 32 ensemble members between 12 LST and 18 LST under the threshold of 30 mm/6hr. 99

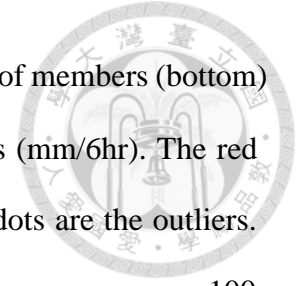


Figure 6.5 The box plot of skillful spatial scale (top) and the number of members (bottom) that can achieve the FSSuniform under different rainfall thresholds (mm/6hr). The red diamonds in the boxplot represent the mean value, and the yellow dots are the outliers. 100

Figure 6.6 The (a) eFSS, (b) dFSS, and (c) eFSS – dFSS of the 6-hour accumulated precipitation from 08 LST to 20 LST under the threshold of 30 mm/6hr. 101

Figure 6.7 The ensemble LFSS of 6-hour accumulated precipitation from 08 LST to 20 LST under the threshold of 30 mm/6hr. 102

Figure 6.8 The (a) mean value and (b) standard deviation of the LFSS for the 6-hour accumulated precipitation from 08 LST to 20 LST under the threshold of 30 mm/6hr. 103

Figure 6.9 Three matching types of the MODE method for the 6-hour observational rainfall from 12 LST to 18 LST. 104

Figure 6.10 The ensemble matching results of the MODE method for the 6-hour rainfall from 12 LST to 18 LST. 105

Figure 6.11 The centroids and the corresponding orientation of the observational and forecasted rainfall areas from the MODE method. 106

Figure 6.12 Four kinds of geometric bias evaluated by the MODE method. The black dot at the origin represents the observation. 107

Figure 6.13 The probability density function of the rainfall intensity from gauge-corrected QPE (red solid), gauge data (red dashed), ensemble QPF (blue solid), and the gauge-grid data of the ensemble members (blue dashed). The color shading shows the spread of one standard deviation. 108

Figure 6.14 The histogram of the forecasted maximum 6-hour accumulated precipitation from 12 LST to 18 LST. The red line is the observational maximum. 108

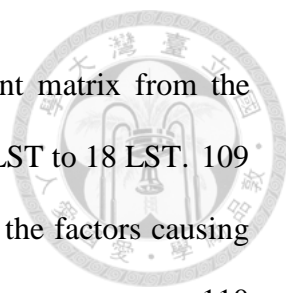


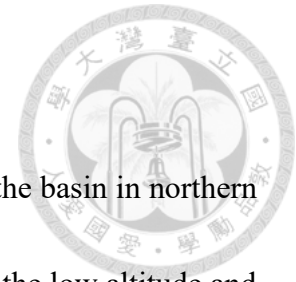
Figure 6.15 The (a) dendrogram and (b) the correlation coefficient matrix from the hierarchical clustering of 6-hour accumulated precipitation from 12 LST to 18 LST. 109

Figure 7.1 The schematic diagram of the physical mechanisms and the factors causing ensemble diversities on the environment before thunderstorm initiation. 110

Figure 7.2 The schematic diagram of the thunderstorm development and the factors causing ensemble diversities in the ECMWF members. 111

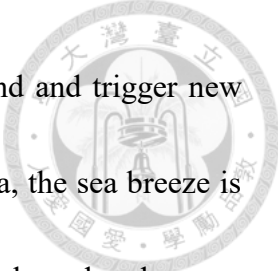
Figure 7.3 The schematic diagram of the thunderstorm development and the factors causing ensemble diversities in the NCEP members..... 112

Chapter 1. Introduction



Taipei, the largest metropolitan region of Taiwan, is located in the basin in northern Taiwan. This city is usually exposed to the risk of inundation due to the low altitude and the several surrounding rivers. Therefore, the sewer system in the urban area is well designed and can endure rainfall intensity up to 78 mm/hour. Most runoff can be successfully drained except for the short-duration high-intensity rainfall that exceeds this limit. One of the risky systems in the Taipei Basin is the afternoon thunderstorms during the warm season. A severe case in recent years occurred on 4 June 2021, which brought heavy rainfall with the peak intensity exceeding 100 mm/hour in southeastern Taipei and caused several districts to be flooded. The physical processes involved and their predictability in the numerical weather prediction (NWP) need to be understood more to increase the leading time of disaster precaution and mitigate the possible damage.

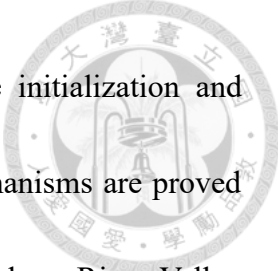
Jou (1994) investigated the lifecycle of the afternoon thunderstorm systems in the Taipei Basin through radar and surface observations. The solar heating in the morning can induce the sea breeze and bring moisture into the basin. The moistened planetary boundary layer provides more precipitable water, and the environment becomes much more convectively unstable, which is favorable for thunderstorm initiation in the afternoon. The thermal forcing on the Snow Mountain Range (SMR) and the up-slope wind at the foothill provide the lifting mechanism to initiate the convective cells. The



thunderstorm cold pool and outflow converge with the up-slope wind and trigger new cells at the downslope side. As the thunderstorms reach the plain area, the sea breeze is lifted. A large amount of the convective energy in the basin is then released and causes heavy rainfall in the urban area.

Lin et al. (2012) used statistical methods to investigate the observational features in the morning that are favorable for Taipei afternoon thunderstorms initiation under weak synoptic conditions. The surface observations along Tamsui River Valley (TRV), Keelung River Valley (KRV), and the sounding at Banqiao in 277 selected days were taken into account. Results show that the weak synoptic wind field and the intense solar heating in the morning favor the onset of sea breeze along TRV and KRV. The sea breeze brings high moisture from the ocean and converges in the Taipei Basin, which plays a critical role in moistening the planetary boundary layer and increasing convective instability in the basin. If the synoptic environment were not too dry at the mid-layer, the thunderstorms would occur in the afternoon with a high possibility.

Miao and Yang (2020) used the numerical model to further investigate the characteristics of the afternoon thunderstorm in the Taipei Basin. The high-resolution model (0.5 km) can successfully simulate most of the crucial phenomena mentioned in Jou (1994) and Lin et al. (2012). The schematic diagram for most physical mechanisms is shown in **Fig. 1.1**. The mesoscale phenomena such as sea breeze, up-slope wind, and



thunderstorm cold pool are demonstrated to be important for the initialization and development of thunderstorms. The interactions between these mechanisms are proved more significant in the Tamsui River Valley (TRV) than in the Keelung River Valley (KRV). Thus, the systems mainly propagate northwestward from the SMR into the Taipei Basin.

The inherent meso- β (20~200 km) to meso- γ (2~20 km) spatial scale and the short lifespan of the afternoon thunderstorm restrict the predictability. Lorenz (1963) pointed out that the initial condition can significantly influence the prediction result, so the deterministic forecast may not reflect all the possible situations. Epstein (1969) demonstrated that in addition to the imperfect initial conditions, the parameterizations of the physical processes could contribute to the model uncertainty. However, the ensemble forecast technique could effectively describe the probability distribution of the possible results from the numerical model.

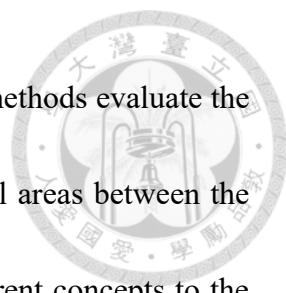
Jeworrek et al. (2021) evaluated the ensemble performance on the quantitative precipitation forecast (QPF) around complex terrain. The ensemble system was established by combining different cumulus schemes, microphysics schemes, planetary boundary layer schemes, and land surface models. The horizontal resolution varied from 27 km to 3 km. Results showed that the higher the resolution was, the better the QPF skill performed. In addition, when the horizontal grid size became finer (<3 km), the



combination between cumulus schemes and microphysics schemes was more critical in the resulting rainfall near the mountainous area. Therefore, when conducting the high-resolution ensemble precipitation forecast around the mountains (e.g., Taipei Basin), the variation of cumulus schemes and microphysics schemes should be considered with higher priority than the other physical parameterizations.

In order to quantify the performance of the model QPF, some methods should be applied. Several traditional indices derived from the four-cell contingency table have been widely used for several decades, such as threat score (TS), equitable threat score (ETS), false alarm rate (FAR), missing rate (MR), and bias score (BS). Although these scores are statistically meaningful and can reflect different aspects of the forecast skill, as the resolution of the NWP model become finer, these point-to-point-based indices may cause some misleading results. The subtle spatial and temporal shift between observational and forecasted fields can be interpreted as “poor performance” by these traditional methods. Besides, the issue of “double-penalty” may cause the verified scores to be lower, and the forecast quality cannot be truly reflected.

New QPF verification methods have been developed to deal with the above-mentioned problems. Gilleland et al. (2009) integrated these methods and classified them into two major categories, which are the “filtering” method and the “displacement” method (**Fig. 1.2**). Filtering methods aim to evaluate the QPF skill at different spatial



scales on the scope of the selected domain, while the displacement methods evaluate the QPF performance by comparing the characteristics of paired rainfall areas between the observation and model forecast. Since the two categories give different concepts to the QPF verification, various aspects of the QPF skill can be viewed if the methods in both classes are applied. Fractions skill score (FSS; Roberts and Lean 2008) and the method for object-based diagnostic evaluation (MODE; Davis et al. 2006) are two popular techniques in the “filtering” and “displacement” categories, respectively, and they are under development in Taiwan’s Central Weather Bureau (CWB; Lai and Hong 2021; 陳等人 2018). This study applied FSS and MODE in the QPF verification section to investigate the ensemble QPF skill from different perspectives.

Although the physical processes within the lifecycle of the afternoon thunderstorm in the Taipei Basin have been examined in previous observational and modeling studies (Jou 1994; Lin et al. 2012; Miao and Yang 2020), high uncertainty still exists in numerical weather prediction. This study aims to find the critical factors in the model that influence these processes. According to the previous studies (Lorenz 1963; Epstein 1969; Jeworrek 2021), the initial conditions and the combination between cumulus schemes and microphysics schemes might significantly influence the forecast of Taipei afternoon thunderstorms. Hence, an ensemble system is established by combining different initial conditions, cumulus parameterizations, and microphysics schemes to address this

scientific question. The prediction is conducted on the afternoon thunderstorm case of 4 June 2021 in the Taipei Basin, and the ensemble performance on (1) the physical mechanisms involved and (2) the resulting QPF output are evaluated and discussed.

The data and methods used in this study are described in Chapter 2. A case overview will be given in Chapter 3 to learn the observational characteristics of the event. One of the ensemble members will be further analyzed in Chapter 4, and the ensemble performance on the physical processes will be discussed in Chapter 5. Chapter 6 provides the verification results on the model QPF. Finally, all conclusions and recommendations for future work will be summarized in Chapter 7.



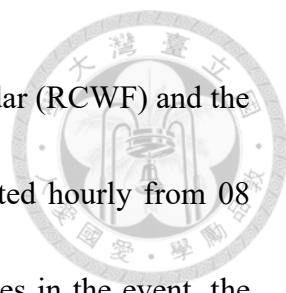
Chapter 2. Data and Methods

2.1 Observation

The synoptic environment of East Asia was examined by the weather chart from the Japan Meteorological Agency (JMA). Himawari-8 satellite images provided information on the approaching Mei-Yu front and the cloud pattern near Taiwan. Other characteristics of the synoptic systems were derived from ERA5, a reanalysis dataset provided by the European Centre for Medium-Range Weather Forecasts (ECMWF) with a spatial resolution of $0.1^\circ \times 0.1^\circ$.

Shulin Radar (RCSL; C-band) and Wufenshan Radar (RCWF; S-band) observed the evolution of the convective cells in northern Taiwan with a temporal resolution of 2 minutes and 6 minutes, respectively. The local surface observations were provided by the automatic weather stations (AWS) and the CWB weather stations every 10 minutes, including accumulated precipitation, pressure, wind speed, wind direction, temperature, and relative humidity. The sounding at Banqiao (46692) was also analyzed to understand the vertical thermodynamic profile of the environment in northern Taiwan. **Figure 2.1** shows all the mentioned observational sites on the map.

The quantitative precipitation estimation (QPE) was computed by the method of Zhang et al. (2008). This process first estimates the rainfall intensity through the Z-R relationship of the S-band radar. Then the ground-based gauges help to correct the rainfall

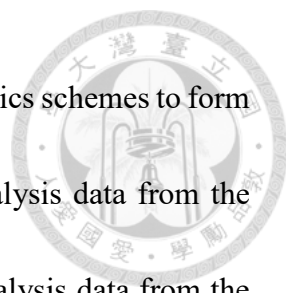


intensity. This study used the reflectivity observed by Wufenshan radar (RCWF) and the Z-R relationship $Z = 32.5R^{1.65}$. These QPE routines were conducted hourly from 08 LST to 20 LST. In addition to producing the precipitation time series in the event, the results were also used to verify the model performance on the quantitative precipitation forecast (QPF) in Chapter 6.

2.2 Model Configuration

Weather Research and Forecasting model version 3.9 (WRF 3.9; Skamarock et al. 2008) was applied in this study to conduct the ensemble prediction. Four two-way nested domains with 27-km, 9-km, 3-km, and 1-km horizontal grid sizes were employed (**Fig. 2.2**). Fifty-five vertical layers were involved, and the model top was set at 20 hPa. The prediction started at 20 LST on 3 June and ended 24 hours later with the integration time step of 60 seconds. The first 12 hours (i.e., before 08 LST 4 June) were the spin-up time, so the model performance was analyzed after this time interval. Besides, the temporal resolution of the model outputs was 30 minutes in the finest domain (i.e., d04 in **Fig. 2.2**).

According to the previous studies (Lorenz 1963; Epstien 1969; Jeworrek et al. 2021), the initial conditions, cumulus schemes, and microphysics schemes are the critical factors that might significantly influence the precipitation results of Taipei afternoon thunderstorms. Therefore, this study systematically combined the variations of two initial



conditions (ICs), four cumulus parameterizations, and four microphysics schemes to form the 32 ensemble members. The initial conditions included FNL analysis data from the National Center for Atmospheric Research (NCAR) and ERA5 reanalysis data from the ECMWF. Both FNL and ERA5 are widely used for operational and research purposes. The parameterization methods from Kain-Fritsch, Betts-Miller-Janjic, Grell 3D ensemble, and Grell-Devenyi ensemble contributed to the variations of the cumulus scheme. The WDM6, Goddard, Thompson, and Morrison schemes built the diversity of microphysics processes. **Table 2.1** shows the detailed configurations of each ensemble member. The long wave and short wave radiation schemes were RRTM and Dudhia methods across all members, and the planetary boundary layer (PBL) scheme was set to be YSU in the whole ensemble system.

2.3 Analyses of Physical Processes

2.3.1 Synoptic Mei-Yu Front

For the location of the observed Mei-Yu front, since half of the ensemble members were initiated by the ECMWF ERA5 reanalysis data, the frontal line should be identified by other sources rather than this reanalysis dataset for fairness. Seitter and Muench (1985) indicated that the rope clouds in the visible satellite images were consistent with the leading edge of the surface front. Therefore, we used this method to locate the observed



frontal line in the following work. On the other hand, the location of the surface Mei-Yu front in the model results was located by the 10-m wind field and the vorticity in the coarsest domain (i.e., d01 in **Fig. 2.2**). The grid points with the maximum vorticity at each longitude from 120 °E to 140 °E were connected to form the predicted frontal line.

2.3.2 Sea Breeze

According to the surface observation at Tamsui River Valley (TRV) on 4 June 2021, the definition of the sea breeze is given in the following to analyze the temporal-spatial distribution of the sea breeze in both observation and ensemble prediction:

- (1) 2-m water vapor mixing ratio higher than 21 g/kg
- (2) 10-m wind direction between -90° and 45° (westerly to northeasterly)
- (3) 10-m wind speed stronger than 2 knots

If the observational station or model grid point along the TRV matches these conditions before the thunderstorm initiation, it will be identified as the sea breeze signal.

2.3.3 Thunderstorm Cold Pool

In order to analyze the characteristics of the thunderstorm cold pool in the model, some definitions are given in the following equations (Rotunno, Klemp, and Weisman 1988; Weisman and Rotunno 2004):

$$B = g \frac{(\theta_v - \bar{\theta}_v)}{\bar{\theta}_v} \quad (2.1)$$

$$\theta_v = \theta(1 + 0.608q_v - q_c - q_r) \quad (2.2)$$



The buoyancy is defined in **Eq. (2.1)** by the virtual potential temperature (θ_v), of which the definition is given in **Eq. (2.2)** for moist air. Since the cold pool is a kind of density current, the virtual potential temperature can reflect the actual air density and describe the cold pool adequately. q_v , q_c , and q_r are the mixing ratio of water vapor, cloud water, and rain water, respectively. The base state of virtual potential temperature ($\bar{\theta}_v$) is calculated by averaging over the area of interest. In this study, the scope is the Taipei Basin shown in **Figure 2.1**. Besides, the top of the cold pool is defined as the first altitude from the ground level where the buoyancy is larger than -0.05 m/s^2 (Miao and Yang, 2020).

2.4 Verification Methods for Quantitative Precipitation Forecast (QPF)

2.4.1 Fractions Skill Score (FSS)

Roberts and Lean (2008) introduced “fractions skill score (FSS)” to verify the skillful scale that the high-resolution model can describe. The term “skillful scale” can be interpreted as the spatial resolution at which the forecasted rainfall field can achieve the predetermined score. This method can also implicitly indicate the spatial shift and the size bias of the QPF results.

In the following steps, the procedures to calculate the fractions skill score (FSS) in



Roberts and Lean (2008) and the corresponding values of the involving parameters in this study are stated:

(1) Calculate the binary fields

Set a suitable precipitation threshold “ T ” and filter out the grid points that exceed this value. This process is formulated in **Eq. (2.3a)** and **Eq. (2.3b)**, in which the rainfall fields (R) are converted to the binary fields (I). The subscripts “ O ” and “ F ” represent the observation and forecast, respectively.

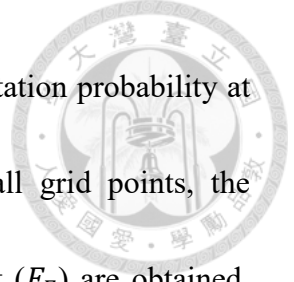
$$I_O = \begin{cases} 1, & R_O > T \\ 0, & R_O < T \end{cases} \quad (2.3a)$$

$$I_F = \begin{cases} 1, & R_F > T \\ 0, & R_F < T \end{cases} \quad (2.3b)$$

In this study, since the initiation time and the duration of the thunderstorm event varied across the ensemble members, the time scope was selected to be 6 hours to cover the entire thunderstorm event for rainfall verification. The threshold was set to be $T=30$ mm/6hr to evaluate the precipitation pattern, which was also consistent with the rainfall verification research in Central Weather Bureau (陳等人 2018). The corresponding R_O and I_O for the 6-hour QPE between 12 LST and 18 LST on 4 June 2021 are shown in **Figure 2.3** for illustration.

(2) Calculate the fractions fields

At each grid point of the binary fields, choose a suitable range of the spatial scales “ N ” (unit: grid) and calculate the fraction that the surrounding N times N grids have the



value “1”. The resulting values can be viewed as the spatial precipitation probability at the surrounding N times N grids. After repeating this process at all grid points, the fractions fields “ F ” of the observation (F_O) and the model forecast (F_F) are obtained. These fractions fields are the function of both the threshold T and the spatial scale N . The processes above can be formulated into **Eq. (2.4a)** and **Eq. (2.4b)** for clarity. The indices “ i ” and “ j ” denotes the row and column of the domain.

$$F_O(T, N)[i, j] = \frac{1}{N^2} \sum_{k=1}^N \sum_{l=1}^N I_O \left[i + k - 1 - \frac{N-1}{2}, j + l - 1 - \frac{N-1}{2} \right] \quad (2.4a)$$

$$F_F(T, N)[i, j] = \frac{1}{N^2} \sum_{k=1}^N \sum_{l=1}^N I_F \left[i + k - 1 - \frac{N-1}{2}, j + l - 1 - \frac{N-1}{2} \right] \quad (2.4b)$$

In this study, the range of the spatial scale N was set from 1 grid to 150 grids. The lower bound corresponds to the highest resolution of the model horizontal grid size (1 km), and the upper bound is consistent with the scale of the northern Taiwan area (150 km).

(3) Calculate the fractions skill score

The mean square error (MSE) of the fraction fields between observation (F_O) and forecast (F_F) can be calculated by **Eq. (2.5)**, in which N_x and N_y are the numbers of columns and rows of the verified domain. The minimum MSE value can be 0, which indicates the forecast fraction field (F_F) perfectly matches the observed fraction field (F_O). According to Roberts and Lean (2008), the maximum possible value of MSE can reach the value called “referenced mean square error” denoted by MSE_{ref} , which can be



formulated into **Eq. (2.6)**.

$$MSE = \frac{1}{N_x N_y} \sum_{i=1}^{N_x} \sum_{j=1}^{N_y} \{F_O[i, j] - F_F[i, j]\}^2 \quad (2.5)$$

$$MSE_{ref} = \frac{1}{N_x N_y} \left\{ \sum_{i=1}^{N_x} \sum_{j=1}^{N_y} F_O^2[i, j] + \sum_{i=1}^{N_x} \sum_{j=1}^{N_y} F_F^2[i, j] \right\} \quad (2.6)$$

Eventually, the fractions skill score (FSS) can be defined by MSE and MSE_{ref} . The definition is shown in **Eq. (2.7)**, in which $MSE_{perfect}$ is perfect zero. FSS can range from 0 to 1, of which 0 denotes no skill and 1 represents perfect skill.

$$FSS = \frac{MSE - MSE_{ref}}{MSE_{perfect} - MSE_{ref}} = 1 - \frac{MSE}{MSE_{ref}} \quad (2.7)$$

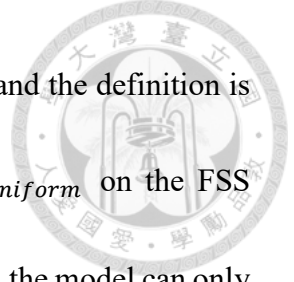
(4) Plot the FSS curve

An FSS curve would be obtained once the scores are computed under a constant threshold T with different spatial scales N . An example is shown in **Fig. 2.4**. As the spatial scale increases from the grid scale (1 km) to the domain scale (150 km), the FSS will also increase to approach an asymptote. Such asymptote can implicitly reflect the relationship between FSS and traditional bias score (f_F/f_O), which is shown in **Eq. (2.8)**. f_O and f_F represent the proportion of the grids exceeding the threshold T in observation and forecast fields. If there is no frequency bias, the value of $FSS_{asymptote}$ will approach 1, and vice versa.

$$FSS_{asymptote} = \frac{2f_O f_F}{f_O^2 + f_F^2} \quad (2.8)$$

(5) Define an acceptable score

In order to find the skillful spatial scale, a proper value of targeted FSS is needed.



Roberts and Lean (2008) denoted this targeted FSS as $FSS_{uniform}$, and the definition is given in **Eq. (2.9)**. The corresponding spatial scale S_{min} at $FSS_{uniform}$ on the FSS curve is considered the minimum skillful spatial scale. In other words, the model can only describe the precipitation event informatively to the highest resolution of S_{min} grid scale. For the finer structure, the valuable information is lost.

$$FSS_{uniform} = 0.5 + \frac{f_0}{2} \quad (2.9)$$

2.4.2 Three Derivatives of FSS

(1) Ensemble-aggregated FSS (eFSS)

In order to broaden the concept of FSS to the whole ensemble system, Dey et al. (2014) and Ferrett et al. (2021) introduced an index called ensemble-aggregated FSS (eFSS) to evaluate all members as a whole. As shown in **Eq. (2.10)** and **Eq. (2.11)**, the MSE in **Eq. (2.5)** and the MSE_{ref} in **Eq. (2.6)** should be averaged over all M ensemble members first. Then, the eFSS can be derived (**Eq. 2.12**) using the same method in **Eq. (2.7)**. The characteristics of eFSS are the same as the original FSS mentioned in the previous section, of which 1 represents perfect skill while 0 means no skill.

$$MSE_{avg} = \frac{1}{M} \sum_{i=1}^M MSE_i \quad (2.10)$$

$$MSE_{avg}^{ref} = \frac{1}{M} \sum_{i=1}^M MSE_i^{ref} \quad (2.11)$$

$$eFSS = 1 - \frac{MSE_{avg}}{MSE_{avg}^{ref}} \quad (2.12)$$



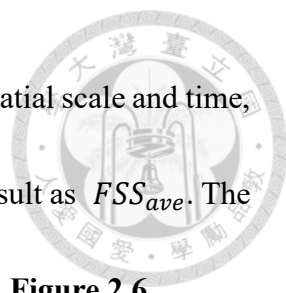
(2) Dispersion FSS (dFSS)

The ensemble spread of the forecast skill is also a crucial issue since an effective ensemble system should be divergent enough but not too dispersed. Rezacova et al. (2009) and Dey et al. (2014) define an index called “dispersion FSS,” denoted by dFSS, to evaluate the spread of an ensemble forecast. dFSS is derived by the same processes as those of the eFSS except that the observation field is replaced by one of the ensemble members called “control member.” The dFSS needs to be compared to the eFSS to determine whether the ensemble spread is proper, and **Eq. (2.13)** shows all possible relationships between dFSS and eFSS with the corresponding meaning. The higher dFSS means the ensemble members tend to perform similarly to the control member rather than the observation, so it is considered under spread, and vice versa. The best ensemble spread occurs when the dFSS is identical to the eFSS.

$$\begin{cases} dFSS > eFSS, \text{ under spread} \\ dFSS = eFSS, \text{ best spread} \\ dFSS < eFSS, \text{ over spread} \end{cases} \quad (2.13)$$

The control member used to calculate the dFSS in this study is determined by the following steps:

- a. Calculate the FSS on 6-hour accumulated precipitation in each member for every spatial scale from 08 LST to 20 LST. **Figure 2.5** shows the resulting FSS of member E01 as an example.

- 
- b. For each member, average the FSS over the dimensions of spatial scale and time, that is, average all the values in **Figure 2.5** and denote the result as FSS_{ave} . The histogram of FSS_{ave} for all ensemble members is shown in **Figure 2.6**.
- c. Since the control member is chosen to compare with other members to interpret the ensemble spread, the best choice may be the member with the median of FSS_{ave} .
- d. The resulting control member is E05 with the FSS_{ave} of 0.80.

(3) Localized FSS (LFSS)

Both temporal evolution and spatial variation of the rainfall areas are crucial. However, the original FSS introduced by Roberts and Lean (2008) can only evaluate the temporal evolution. To make up for the verification of spatial variation, Woodhams et al. (2018) brought forward a new index called “localized FSS” and denoted LFSS.

The calculation of LFSS is similar to FSS. The only difference is to average the mean square error over time at each grid point rather than average over the whole domain. Therefore, we can view the performance of each grid independently. In short, it rewrites the MSE from **Eq. (2.5)** to **Eq. (2.14)** and the MSE_{ref} from **Eq. (2.6)** to **Eq. (2.15)**. The resulting FSS shown in **Eq. (2.16)** is the LFSS. The indices i and j in the brackets represent the row and column of the domain.

$$MSE[i, j] = \frac{1}{N_t} \sum_{t_i=1}^{N_t} \{F_O[t_i, i, j] - F_F[t_i, i, j]\}^2 \quad (2.14)$$

$$MSE_{ref}[i, j] = \frac{1}{N_t} \sum_{t_i=1}^{N_t} \{F_O^2[t_i, i, j] + F_F^2[t_i, i, j]\} \quad (2.15)$$

$$LFSS[i, j] = 1 - \frac{MSE[i, j]}{MSE_{ref}[i, j]} \quad (2.16)$$



2.4.3 Method for Object-based Diagnostic Evaluation (MODE)

Davis et al. (2006) introduced the method for object-based diagnostic evaluation (MODE) to verify the characteristics of forecasted precipitation area. The procedures involved in this method and the parameters used in this study are illustrated in the following steps:

- (1) Convolve the rainfall fields in both observation and model forecast with a convolution radius “ R ” to smooth the boundary of the precipitation area. In this study, the radius R is set to be five grids (5 km).
- (2) Set a rainfall threshold “ T ” and filter out the grids that exceed this value. T is set to be 30 mm/6hr, which is consistent with that used in the FSS method in the previous sections. The results of different methods can thus be compared to each other.
- (3) Label the rainfall objects that are just filtered out and match them between observation and forecast fields. **Eq. (2.17)** shows the matching criteria, in which A_O and A_F represent the areas of observation and forecast entities, and D means the distance between their centroids.

$$D < A_O^{1/2} + A_F^{1/2} \quad (2.17)$$

- (4) After obtaining the matching pairs of the rainfall entities, we can compare their characteristics, such as size, centroid location, axis orientation, aspect ratio, and probability density function of the rainfall intensity.



Chapter 3. Case Overview

3.1 Synoptic Environment



The JMA surface weather chart in **Figure 3.1** shows the synoptic pattern in the morning. A Mei-Yu front was located offshore of northern Taiwan about 50 km, and Typhoon Choi-Wan (2021) was near the southwest coast of Taiwan. The environment could not be realized as weak synoptic like the previous studies on Taipei afternoon thunderstorms (Jou 1994; Lin et al. 2012; Miao and Yang 2020). Instead, the synoptic systems, especially the Mei-Yu front, might influence the evolution of the convective systems at Taipei Basin. In order to investigate the location of the Mei-Yu front with a higher temporal resolution, the visible satellite images in **Figure 3.2** were used to identify the frontal line at 3-hour intervals from 08 LST to 17 LST. The results were plotted in **Figure 3.3**, which indicates that the front kept moving southward in the morning and reached the northern coast of Taiwan at 14 LST. However, the front lingered over the sea after this time. As we will see in Section 3.3, the surface observations in the Taipei Basin did not detect the signal of the arrival of this Mei-Yu front until the convective cells ended their development processes at 17 LST. The local circulations such as the sea breeze and the thunderstorm cold pool prevailed, which suggested that although the convective cells were close to the frontal line, the forcing provided by this synoptic system might be less significant in this event.



In addition to the surface front, the infrared and visible satellite images (**Fig. 3.4**) were used to investigate the synoptic cloud pattern in the morning. Some high clouds at the boundary of the frontal rainband covered the northwest part of Taiwan, of which the cloud top temperature was about $-40\text{ }^{\circ}\text{C}$ to $-50\text{ }^{\circ}\text{C}$. Nevertheless, the visible images showed that these clouds were not too thick to affect the solar heating in the morning. As we will show in the following, solar heating was still significant in the Taipei Basin and provided a favorable environment for the event.

The sounding of Banqiao station (46692) at 08 LST (00 UTC) is shown in **Figure 3.5**. The parcel lifting curve at 08 LST pointed out that the inversion layer at 800 hPa could effectively restrain the shallow convection in the morning, which could also be reflected by the existence of CIN (-31 J/kg). The solar heating increased the surface temperature from $30.6\text{ }^{\circ}\text{C}$ to $33.6\text{ }^{\circ}\text{C}$ in the morning (08 LST to 12 LST). Therefore, the lifting curve shifted to the right, causing the CAPE to increase from 1088 J/kg to 3169 J/kg and much more favorable for thunderstorm initiation. Besides, the southwesterly from the surface to 500 hPa brought the moisture from the South China Sea to northern Taiwan, making the environment wetter across the low to mid levels. Such high environmental moisture can provide adequate precipitable water for the extreme thunderstorm event in the afternoon.



3.2 Evolution of the Thunderstorms

The time series of composite reflectivity observed by Shulin radar (RCSL; C-band) are presented in **Figure 3.6**. At 12 LST, there were two groups of convective cells initiated. One was at the ridge, and the other was at the foothill of the Snow Mountain Range (SMR). The group at the ridge matured at 14 LST and moved toward the northeast coast with reintensification at 17 LST as the Mei-Yu front approached. The other group, which is the main target of this study, initiated at the foothill and propagated northwestward into the Taipei Basin with the maximum reflectivity parallel to the ridge of SMR. New cells continued to be triggered along the Tamsui River Valley (TRV) until they arrived at the coastline at about 15 LST. After the release of convective instability, the cell development in the basin weakened.

The resulting rainfall fields are presented in **Figure 3.7** with the hourly interval from 12 LST to 20 LST. The rainfall pattern was similar to that of the reflectivity field (**Fig. 3.6**), and the maximum hourly rainfall was up to 132 mm at the southeast Taipei Basin between 13 LST and 14 LST. According to the 6-hour accumulated precipitation from 12 LST to 18 LST (**Fig. 3.8**), two rainfall hotspots were observed at Fu-Jou Mountain (221 mm/6hr) and Ping-Lin (222 mm/6hr). The lack of rain gauge in the mountainous area caused the problem that the overestimation of the rainfall intensity by the Z-R relationship ($Z = 32.5R^{1.65}$) at the SMR could not be corrected. The discrepancy between the QPE

maximum (280mm/6hr) and the gauge maximum (222 mm/6hr) occurred near Ping-Lin.

As a result, the observations from the surface rain gauges were used to determine the maximum value, while the QPE patterns were used to verify the QPF results from the model.

3.3 Mesoscale Processes

The main focus of this study is the thunderstorms initiated at the SMR with the development toward the Taipei Basin. Previous studies (Jou 1994; Miao and Yang 2020) indicated that the interactions between the sea breeze and the thunderstorm cold pool along the TRV are crucial in this type of event. Thus, in order to understand the physical processes at TRV in this case, six CWB stations were chosen from the foothill of the SMR to the estuary of Tamsui River (**Fig. 3.9**). The time series of 2-m water vapor mixing ratio and 10-m wind (**Fig. 3.10**) show that the sea breeze established at 09 LST, then it penetrated into the Taipei Basin with moisture increasing to about 22 g/kg. This signal propagated through the whole basin and arrived at the foothill of SMR (Xindian) at 11 LST, which was about 1 hour before the thunderstorm initiation (**Fig. 3.6**).

After the thunderstorms initiated in the mountainous area, the cold pools were induced under the convective cells. Wakimoto (1982) pointed out that the signals of temperature drop, pressure increase, wind shift, and enhanced wind speed could be



detected as the leading edge of the thunderstorm cold pool passed. Some of these phenomena are shown in **Figure 3.11**. The temperature dropped by 6 °C with a sudden wind shift from northwest to southeast near Xindian at 12 LST. The pressure slightly increased and became more perturbed after this time. As the cold pool propagated downslope toward the northwest, the same signals were observed at the other 5 stations later. However, the wind direction at NTU was always from the northeast without any change. The reason might be the several high buildings surrounding the observational site since only the momentum field was affected while the mass fields (pressure and temperature) were not. The cold pool moved along the TRV and reached Tamsui at about 1430 LST. These spatiotemporal features matched well with those where the intense radar reflectivity echoes were (**Fig. 3.6**), demonstrating again that the convective system could induce the cold pool and trigger new cells in front of them.

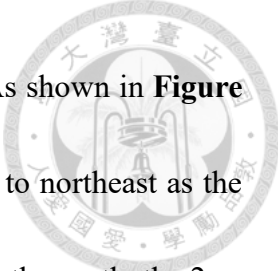


Chapter 4. Ensemble Member E17

Most of the observational data in Chapters 2 and 3 could only provide piecewise information about the physical processes. To get more insight into the complete evolution of the systems, an ensemble member that could successfully predict the synoptic environment and the mesoscale processes can be chosen and further analyzed. When evaluating the diversities of the ensemble members in the next chapter, this member could act as an analogy to the observation. After a comprehensive assessment of the synoptic environment (i.e., Mei-Yu front), mesoscale processes (i.e., sea breeze and cold pool), and the resulting precipitation, the ensemble member No. 17 (abbreviated as E17 hereafter) was chosen. In this chapter, the verification of E17 will be given, and more details of the convective system will be analyzed with a higher spatiotemporal resolution.

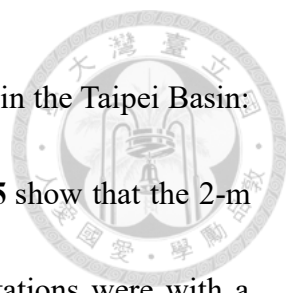
4.1 Synoptic Environment around Northern Taiwan

Figure 4.1 shows the synoptic Mei-Yu front in E17 with the observational frontal line. The frontal line matched well with the observation to the east of 124 °E, while the west part of the frontal line in E17 moved slower at about 50 km to the north of the observed line in the morning. The front approached the northwest corner of Taiwan at 14 LST and then lingered. Corresponding synoptic parameters such as surface wind, temperature, and moisture were evaluated by averaging over the 1° by 1° box at northern



Taiwan Strait (**Fig 4.2a**) to show the evolution of the environment. As shown in **Figure 4.2b**, the wind direction gradually rotated clockwise from southwest to northeast as the Mei-Yu front approached. After the cold advection strengthened from the north, the 2-m temperature dropped from 27.3 °C to 26.3 °C, and the water vapor mixing ratio slightly decreased from 21.8 g/kg to 20.5 g/kg. It will be shown in the following analyses that the thunderstorm had matured and propagated through the Taipei Basin before the Mei-Yu front arrived, so the thunderstorm development was not heavily influenced by the synoptic forcing, which is similar to the observations in Chapter 3.

In addition to the surface environment, the pattern of high clouds was also taken into account since it might influence the solar heating in the morning. The cloud top temperature at 08 LST and 11 LST in E17 (**Fig. 4.3**) were comparable to the observation (**Fig. 3.4**) near northern Taiwan with the value of -40 °C to -50 °C. The cloud coverage was also similar at first glance. To quantitatively analyze the cloud coverage and thickness over the Taipei Basin, the grid points of the cloud should be clearly defined first. The grids were identified as clouds if the sum of cloud water and cloud ice exceeded 0.001 g/kg (Kurowski et al. 2018), and the percentile of these grids at each level over the Taipei Basin (**Fig. 3.9**) could be considered as the cloud fraction. The resulting time-height plot of the cloud fractions (**Fig. 4.4**) indicates that the high clouds covered 60% to 70% of the sky in the morning (08 LST to 10 LST) and were mainly located from 11 km to 13 km.



The solar heating in the morning was analyzed by three stations in the Taipei Basin: Banqiao, Taipei, and National Taiwan University. Results in **Fig. 4.5** show that the 2-m temperature between observation and model forecast at all three stations were with a slight difference (< 0.5 °C) in the early morning (08 LST). However, the heating limb in the model tended to be steeper and was about 1 °C warmer after the temperature reached the peak between 10 LST and 12 LST. This discrepancy might be contributed by the systematic bias in the short-wave radiation scheme (Dudhia) since the heating rate differed slightly (see the next chapter) with different configurations of the initial condition, cumulus scheme, and microphysics scheme. In addition, the cooling occurred earlier in E17 due to the earlier thunderstorm initiation (1.5 hours) in the model (see the next section).

4.2 Evolution of the Thunderstorms

The composite radar reflectivity (**Fig. 4.6**) shows that one of the convective cells initiated near the foothill of Snow Mountain Range (SMR) at 10 LST, and the other was over the ridge at 1030 LST. Although the timing was 1.5 hours earlier than the observation (**Fig. 3.6**), the subsequent development of the convective cells was quite similar. On the one hand, the cells at the foothill propagated northwestward into Taipei Basin and reached the coastline at about 14 LST before the synoptic Mei-Yu front arrived (**Fig. 4.1**). On the



other hand, the cells at the ridge moved northeastward as the front approached the northeast coast of Taiwan. The thunderstorm development could also be identified by the cloud fraction of Taipei Basin in **Figure 4.4**, which shows that the low clouds started to increase after 10 LST. As the convective cells developed upward and matured, the cloud fraction exceeded 40% at all levels (13 LST). After the thunderstorm started to dissipate in the late afternoon (18 LST), the precipitation became more stratiform within the basin, and the cloud profile tended to concentrate at the middle levels.

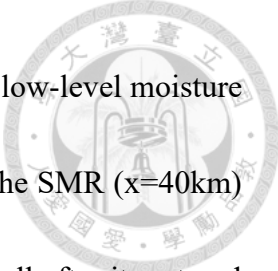
The hourly rainfall from 10 LST to 18 LST is displayed in **Figure 4.7**. At the early stage, the precipitation area propagated from the SMR toward the Taipei Basin with the maximum rainfall intensity up to 67 mm/hour between 13 LST and 15 LST. After the Mei-Yu front dominated this area after 15 LST, the horizontal area of the precipitation widened over the SMR and moved northeastward. The 6-hour accumulated precipitation shown in **Figure 4.8** also exhibited two precipitation hotspots, one on the east side of the central Taipei Basin and the other on the west side. Although the 1-hour rainfall intensity and the 6-hour accumulation were less than the observations (**Fig. 3.7** and **Fig. 3.8**), the involving precipitation areas and the development processes were similar. The mesoscale processes such as sea breeze and cold pool will be further analyzed in the next section.



4.3 Mesoscale Processes

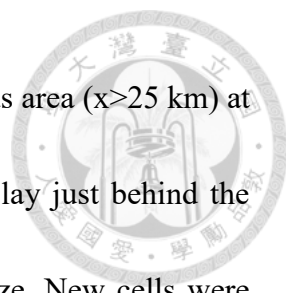
The sea breeze in the morning was analyzed through the 2-m water vapor mixing ratio and 10-m wind field (**Fig. 4.9**). The results indicate that the sea breeze onset was at 09 LST, at which the solar radiation rapidly heated the land (**Fig. 4.5**). A large amount of moisture over Taiwan Strait was transported into the Taipei Basin along the Tamsui River Valley (TRV), and the water vapor mixing ratio rose to 22 g/kg as the sea breeze passed. Thus, the convective instability could be further increased by the wetted boundary layer. As long as a lifting mechanism existed, the convective instability could be released. The up-valley wind along the foothill of SMR (i.e., Xindian) at 09 LST lifted the air layer, and one hour later (10 LST), the thunderstorm was initiated here (**Fig. 4.6**). After the thunderstorm propagated northwestward along the TRV, an apparent low-moisture boundary was found at the edge of high reflectivity, which was also a signal of the cold pool and the thunderstorm outflow, providing the lifting mechanism in the plain area.

Since most of the convective cells developed along the TRV, more insights can be found in this cross section to investigate the physical processes involved. As shown in **Figure 3.9**, this cross section started from the estuary of Tamsui River to the ridge of SMR with a 6-km width in the zonal direction. The time series in **Figure 4.10** indicated that the sea breeze in the morning, the thunderstorm cold pool, and the outflow were all observed in this event. The environment of the Taipei Basin was highly convectively



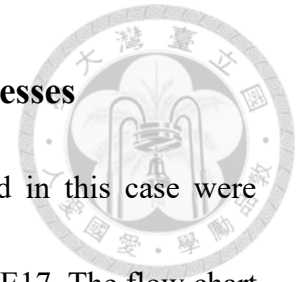
unstable ($\frac{\partial\theta_e}{\partial z} \ll 0$) in the morning, owing to the solar heating and the low-level moisture brought by the sea breeze. The first convective cell was initiated on the SMR ($x=40\text{km}$) at 10 LST, and the corresponding cold pool was detected under this cell after it matured at 11 LST. The cold pool was about 500-m thick and then propagated downslope into the Taipei Basin. The leading edge of this cold pool converged with the sea breeze and triggered a new cell ($x=20\text{km}$) in front of the old cells ($x>25\text{km}$) at 12 LST. The new cell matured later at 1330 LST and induced another cold pool. The moist air brought by the sea breeze continued to converge with thunderstorm outflow and lifted by the cold pool to release the convective instability until 15 LST. After the Mei-Yu front arrived at 15 LST, the synoptic-scale wind dominated in northern Taiwan, and the environment became colder. The favorable conditions for forming new cold pools no longer existed as the contrast of the air density between the rainfall area and the environment decreased. In the absence of the interactions between the sea breeze and the cold pool, the convective cells were trapped over the SMR. The rainfall inside the Taipei Basin thus weakened afterward.

To summarize the mesoscale processes involved in this ensemble member, the Hovmöller diagrams of sea breeze, radar reflectivity, and cold pool along the TRV were plotted in **Figure 4.11**. The 10-m wind (**Fig. 4.11a**) shows that the signals of the sea breeze started from the estuary ($x=0\text{ km}$) at 09 LST, which reached the central Taipei Basin ($x=20\text{ km}$) before being lifted by the cold pool at 11 LST. The convective cells and the induced



thunderstorm cold pool (**Fig. 4.11b**) were initiated in the mountainous area ($x > 25$ km) at 10 LST. During the downhill development, the cold pools always lay just behind the leading edge with the outflow direction in contrast to the sea breeze. New cells were triggered by the convergence between the thunderstorm outflow and the sea breeze. This mechanism repeated until the convergence line arrived at the estuary of Tamsui River ($x = 0$ km) around 15 LST, when the Mei-Yu front approached northern Taiwan. The front destroyed the local circulation of sea breeze, and the environment became cooler under the cold advection from the north. The self-development processes ended in the Taipei Basin without the interactions between the sea breeze and the thunderstorm cold pool. Hence, the following convective cells were mainly concentrated over the SMR ($x > 25$ km).

Chapter 5. Ensemble Performance of the Physical Processes



In the previous two chapters, the physical processes involved in this case were analyzed by the observation and the results from ensemble member E17. The flow chart in **Figure 5.1** can systematically summarize the relationships between the synoptic environment and the thunderstorm mesoscale processes. The environment near northern Taiwan was mainly influenced by the location of the Mei-Yu front, which further affected the meteorological parameters, including temperature, wind, and moisture around this area. The interactions between each mesoscale process, such as solar heating, sea breeze, and the thunderstorm cold pool, dominated the spatiotemporal characteristics of the convective cells. In this chapter, the scope will expand from a deterministic viewpoint to a probabilistic perspective. All of the ensemble members will be analyzed by the methods that have been described in Chapter 4. Then the results will be viewed as a whole to evaluate the ensemble skill and the ensemble spread in the forecasts of the thunderstorm event. The key factors that contributed to the ensemble diversity will also be discussed.

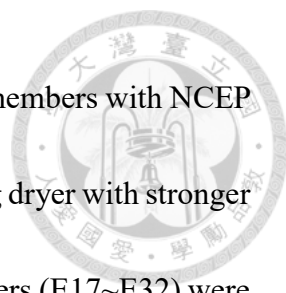
5.1 Synoptic Environment

The observational and predicted frontal lines were plotted together in **Figure 5.2** for comparison. The ensemble mean moved slower to the east of 124 °E but matched well to the observation near Taiwan. When digging more into the performance of each member,



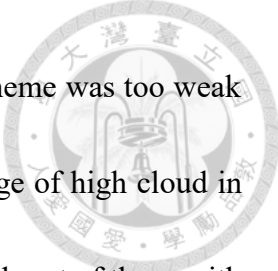
the locations of the Mei-Yu front could be easily classified into two categories by different initial conditions (ICs), which were NCEP FNL (E01~E16) and ECMWF ERA5 (E17~E32). Although the ensemble mean exhibits quite good consistency with observation to the west of 124 °E, neither the two clusters could predict the best position. The cold advection behind the Mei-Yu front was much stronger in the members initiated by NCEP FNL (E01~E16), and thus the front moved toward the south faster. On the contrary, the front of the members with ECMWF ERA5 initial condition (E17~E32) moved slower and approached Taiwan later. Regarding the east part of the front, all members predicted slower movement, especially the NCEP FNL ones. However, the east part of the front will not be taken much into account since it is far from the area we were interested in (i.e., Taipei Basin). To sum up, we found that the initial conditions dominated the location of the Mei-Yu front. The ensemble result could also indicate the possible site of the system, even though most members could not predict this system successfully.

In addition to the front location, the resulting meteorological parameters near northern Taiwan were also examined. Owing to the discrepancy in the movement of the Mei-Yu front, the surface environment of the north Taiwan Strait might be pretty different. Therefore, the 10-m wind, 2-m temperature, and 2-m water vapor mixing ratio in the 1° × 1° box (**Fig. 4.2a**) were analyzed before the thunderstorm matured (08 LST to 13 LST), and the ensemble results are shown in **Figure 5.3**. An apparent demarcation between E16



and E17 is the separation line of the different initial conditions. The members with NCEP FNL initial condition (E01~E16) tended to be 1.5 °C cooler and 2 g/kg dryer with stronger cold advection from the north. In contrast, the ECMWF ERA5 members (E17~E32) were warmer and wetter because of the later arrival of the Mei-Yu front. Furthermore, as the synoptic wind turned north, the ECMWF members were 0.5 °C warmer and 1 g/kg wetter than those with NCEP members. The result shows that just like the front location, the ensemble spread of the synoptic environment near the surface was brought by the diversity of initial conditions.

According to the observational satellite images (**Fig. 3.4**), the high clouds at the edge of the frontal rainband covered the west coast of Taiwan, some of which moved inland into the Taipei Basin. Solar heating, one of the crucial factors for the sea breeze and thunderstorm initiation, might be sensitive to these clouds. To investigate the diversities of the ensemble system, the stamp chart in **Figure 5.4** shows the cloud top temperature of each ensemble member in the morning (08 LST). A noticeable feature was that the members performed similarly to those with the same microphysics scheme without regard to which initial condition or cumulus parameterization was used. WDM6 and Goddard microphysics schemes resembled the satellite images more with the cloud covering the northwest coast of Taiwan, but the cloud top temperature was about 10 °C lower. Nevertheless, the Thompson and Morrison microphysics parameterizations predicted two



extremes, in which the signal of the high clouds in the Thompson scheme was too weak while those in the Morrison scheme were too strong. The leading edge of high cloud in the members with NCEP FNL initial condition was located to the southeast of those with ECMWF ERA5 initial condition under the same combination of microphysics and cumulus parameterizations. The systematic shift of the high cloud position between the members with different initial conditions was consistent with the discrepancy of the frontal location near the surface (**Fig. 5.2**).

The vertical thickness of the clouds was also crucial to solar heating. **Figure 5.5** shows the averaged cloud fraction profile in the morning (i.e., the time average from 08 LST to 10 LST in **Figure. 4.4**) for each member. Like the horizontal pattern, the high clouds in the members with the Morrison scheme (E04, E08, E12, and so on) were much thicker than in other microphysics schemes. This means that the Morrison scheme tended to have a systematic bias of predicting too many ice-phase hydrometeors at high levels. On the other end, the Thompson scheme (E03, E07, E11, and so on) predicted too few high clouds, and the clouds even disappeared with the ECMWF ERA5 initial condition (E19, E23, E27, and E31) due to the slower southward movement of the Mei-Yu front.

In summary, the initial conditions mainly dominated the location of the surface Mei-Yu front and the leading edge of the high clouds. The microphysics scheme influenced the horizontal and vertical distribution of the hydrometeors without regard to which initial

condition was combined. However, the cumulus scheme did not contribute to the ensemble diversity with any apparent signal on the discussed physical processes.



5.2 Solar Heating and Sea Breeze in the Morning

The solar heating in the morning was evaluated by averaging the 2-m temperature at the grids lower than 100 meters in the Taipei Basin (**Fig. 5.6a**). The ensemble time series (**Fig. 5.6b**) suggested that the heating diversity could break down into two parts. The first was the mean temperature state dominated by the synoptic environment (i.e., Mei-Yu front). The members initiated by NCEP FNL (E01~E16) were about 1 °C cooler than those with the ECMWF ERA5 initial condition. The same tendency was also found in the northern Taiwan Strait in the previous section. The other factor was the microphysics scheme used. A clear difference is between the members with the Morrison scheme (E04, E08, E12, and so on) and the other three parameterizations. At first glance, the Morrison scheme had a systematic time lag in the morning. If the heating process was averaged in the members of different microphysics schemes (**Fig. 5.7**), the surface temperature variation within WDM6, Goddard, and Thompson schemes were in-phase. However, the Morrison scheme shifted 30 to 60 minutes later. The reason could be traced back to the cloud pattern at the high levels. As mentioned in the previous section, the Morrison scheme was prone to predicting too much ice-phase hydrometeor, and the cloud fraction

over the Taipei Basin was too much. The cloud thickness was also at least 2 times thicker than the other schemes, which could reduce the solar heating in this area and postpone the time the basin started to be heated.



When it comes to the sea breeze, the onset time was closely related to the solar heating process on the land. Therefore, the ensemble spread of the surface temperature discussed in the previous paragraph was supposed to transfer to the ensemble performance of the sea breeze. The sea breeze traveled into the Taipei Basin mainly through the Tamsui River Valley (TRV), so we will focus on this northeast to southwest cross section (**Fig. 3.9**) in the following analysis. In order to find where the leading edge of the sea breeze was, the grids along the TRV were defined as sea breeze if all the criteria in Section 2.3.2 were satisfied, and the first detected time along this line was recorded in **Figure 5.8**. Results showed that the sea breeze started at the estuary of Tamsui River and propagated inland toward the Snow Mountain Range (SMR). Although the overall signals show the same propagating direction, some diversities existed between the ensemble members.

First, the onset time within the members of ECMWF ERA5 initial condition (E17~E32) was earlier (09 LST) than the NCEP FNL ones (10~11 LST) near the estuary ($x=0\sim 10$ km). The difference in the synoptic environment of the northern Taiwan Strait might contribute to this spread, which was influenced by the initial conditions based on

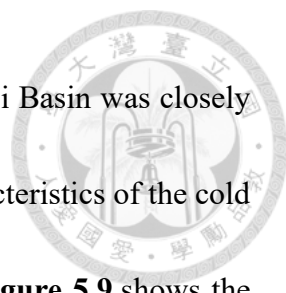


the investigation in the previous section (**Fig. 5.3**). The water vapor mixing ratio over the ocean tended to be higher in ECMWF ERA5 members (E16~E32), so the moisture could achieve criteria (1) in Section 2.3.2 earlier than the NCEP FNL ones (E01~E16). Despite the later onset, the sea breeze in the NCEP FNL members could propagate more inland to the foothill of SMR ($x=30\sim 40$ km), while those in ECMWF ERA5 ones could only reach the center of the basin ($x=20$ km). This discrepancy of where the sea breeze could achieve will be discussed later with the thunderstorm cold pool characteristics.

Next, the timing spread was observed between the Morrison microphysics schemes and the others. An apparent time lag occurred in the Morrison members, and the postponement was consistent with the delay of solar heating with about 1 to 2 hours later than the other microphysics schemes. If tracing further back, the ensemble spread of the synoptic cloud pattern did influence the mesoscale physical processes. More high clouds produced by the Morrison scheme caused the solar heating later and delayed the sea breeze onset. Thus, the ensemble spread of the synoptic environment could influence and transfer to the mesoscale processes through the flowchart plotted in **Figure 5.1**.

5.3 Thunderstorm Cold Pool

Although the sea breeze could transport the low-level moisture into the Taipei Basin, the convective instability would not be released until the air was lifted. According to the



investigation in Chapters 3 and 4, the lifting mechanism in the Taipei Basin was closely related to the thunderstorm cold pool. Therefore, the ensemble characteristics of the cold pool and their interactions with the sea breeze will be discussed. **Figure 5.9** shows the first detection time of the convective cell (>45 dBZ) and the induced cold pools along TRV, which were produced by the evaporation cooling and the rainfall downdraft.

Although there was good consistency between the reflectivity signal and the cold pool regarding the location and the direction of propagation, the features were dissimilar in the members with different initial conditions. The thunderstorm and the resulting cold pools in the ECMWF members (E17~E32) started from the SMR and propagated downslope in sequence, the same as the observation discussed in Chapter 3. However, those in the NCEP members (E01~E16) were more cluttered. Even some of the convective cells initiated near the estuary and propagated upslope to the SMR (e.g., E02, E04, E10, and E12). The dissimilar propagation of the thunderstorm might cause the discrepancy between these two groups. The lifting mechanism in the ECMWF members was located near the mountainous area before the Mei-Yu front arrived in the afternoon. Nevertheless, the earlier arrival of the Mei-Yu front in the NCEP members provided the low-level forcing everywhere near the wind shear line in the morning, which caused the convective cells to be initiated at a more uncertain location.

Besides, the cold pool occurrence frequency from 08 LST to 20 LST (**Fig 5.10a**) and



the maximum cold pool thickness (**Fig. 5.10b**) indicated that the cold pools in the ECMWF members were more intense and prolonged. The cold pool thickness could reach 1 km with more detection along the entire valley, but those in the NCEP members (E01 to E16) were thinner and concentrated near the foothill ($x=20\sim 40$ km) with less occurrence. The weaker signal of the thunderstorm cold pool would mitigate the lifting mechanism in the basin. Even though the NCEP members brought the moisture more inland, it would not be lifted effectively and converted to precipitation. On the contrary, although the sea breeze in the ECMWF members only reached the center of Taipei Basin ($x=20$ km), it encountered a more vigorous thunderstorm cold pool and lifted. The convective energy could thus be released, leading to heavy rainfall in the plain area.

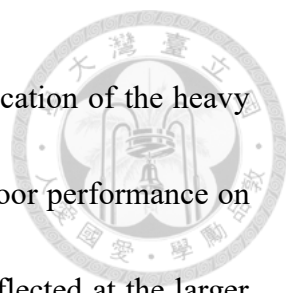
Chapter 6. Verification on Quantitative Precipitation Forecast (QPF)

So far, we have discussed the ensemble performance on the topics of the synoptic environment and the mesoscale processes. This chapter will consider the resulting rainfall field since it is a crucial issue in disaster prevention and can help us realize the characteristics of the ensemble system. The concept of fractions skill score (FSS; Roberts and Lean 2008) and the method for object-based diagnostic evaluation (MODE; Davis et al. 2006) were used to evaluate the ensemble performance on the quantitative precipitation forecast (QPF). After the verification by these two methods, the hierarchical clustering technique will be applied to categorize the members, and their connection to the physical processes discussed in previous chapters will be provided.

6.1 Fractions Skill Score and its Derivatives

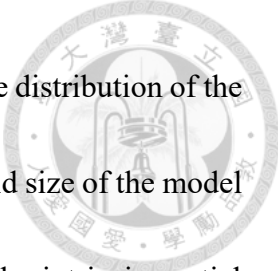
6.1.1 Fractions Skill Score (FSS)

The fractions skill score (FSS) was applied to the 6-hour accumulated precipitation of all ensemble members from 08 LST to 20 LST. The results in the member E17 will be used for illustration (**Fig. 6.1**). The lower score at the time interval from 08 LST to 14 LST was caused by the discrepancy of thunderstorm initiation time between E17 and the observation, so we focus more on the later time. As the scope broadened from the grid scale (1 km) to the domain scale (141 km), the FSS increased and reached the perfect



score of 1. It means that the model could hardly predict the exact location of the heavy rainfall due to the stochastic nature of the convection. Despite the poor performance on the rainfall hotspot, the frequency bias, which the FSS implicitly reflected at the larger spatial scope (Eq. 2.8), indicated that the size of the predicted rainfall area with the threshold of 30 mm/6hr was comparable to the observation. Since the FSS increases monotonically as the spatial scale broadens, some thresholds should be determined to define the skillful spatial scale. The $FSS_{uniform}$ (Eq. 2.9) was thus needed to decide whether the performance at the given resolution was acceptable. In order to get the $FSS_{uniform}$ in the verified interval (i.e., 08 LST to 20 LST), the mean observational frequency f_o in Eq. (2.9) was decided by averaging the fractions of grids that exceeded the rainfall threshold (30 mm/6hr) in all 7 periods of the 6-hour accumulated precipitation. The resulting mean frequency f_o was 15.6 %, and the derived criteria, $FSS_{uniform}$, was 0.58. Figure 6.1 shows that the spatial scale coarser than 11 km after 09 LST were all considered skillful.

The steps mentioned above were then applied to all 32 ensemble members. We will mainly focus on the QPF performance from 12 LST to 18 LST (Fig. 6.2) since this time interval covered most rainfall periods in this event (Fig. 3.7) and could reflect the entire rainfall pattern. The FSS curves of each member were plotted in Figure 6.3, and they intersect with the $FSS_{uniform}$ line at different spatial scales, suggesting that the



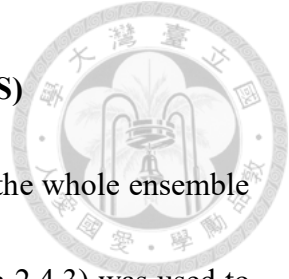
ensemble members were considered skillful at various resolutions. The distribution of the skillful scale (**Fig. 6.4**) indicated that although the finest horizontal grid size of the model was up to 1 km, the useful information could be coarser owing to the intrinsic spatial uncertainty of the convection. All members could be considered skillful at the resolution finer than 21 km, and more than 50 % (21 members) were between 1 km and 11 km. Besides, the asymptotes of the FSS curves in **Figure 6.3** at the domain scale (140 km) were concentrated between the scores of 0.9 and 1.0, which implicitly pointed out that the members well predicted the size of the rainfall area by **Eq. (2.8)**.

In addition to investigating the distribution of the skillful spatial scale (**Fig. 6.4**), the exact value of which could be viewed as a judgment to rank the performance of the 32 ensemble members. According to the concept of FSS, the better the member forecasted, the finer the skillful resolution was. **Table 6.1** listed the skillful spatial scale of each member both in sequence and by rank. It shows that the members with the Morrison scheme (E04, E08, E12, and so on) performed better than the others without regard to what initial condition and cumulus parameterization were used. Nevertheless, the analyses of physical processes in Chapter 5 pointed out that the Morrison scheme performed poorly on both the synoptic cloud pattern and the local solar heating processes in the Taipei Basin. The delayed heating made the environment warmer in the afternoon and more favorable to the development of the thunderstorm cold pool. The following

stronger convergence between the sea breeze and the cold pools pushed the precipitation area toward the northeast along the Tamsui River Valley, thus similar to the observation.

Despite the high score verified by the FSS method, it alerts that better results might be the consequence of combining wrong physical processes, such as those in the Morrison microphysics scheme. Therefore, the member (E17) chosen in Chapter 4 for illustration was determined by not only the high FSS score but also the more reasonable physical processes compared to the observation.

The analyses above were merely based on the rainfall threshold of 30 mm/6hr. As we extend the threshold to other values ranging from 10 to 150 mm/6hr, the characteristics and the trend under different rainfall intensities could be found. **Figure 6.5** shows the distribution of the skillful resolution and the number of ensemble members that could achieve the $FSS_{uniform}$ under different thresholds. All members achieved the criteria when the intensity was smaller than 60 mm/6hr, while only 16 members were considered skillful at the extreme rainfall (150 mm/6hr). As the threshold increased from 10 mm/6hr to 150 mm/6hr, the mean descriptive resolution rose from 19 km to 33 km, which could demonstrate again that the location of the extreme rainfall was quite random and could not be precisely predicted by the model.



6.1.2 Ensemble-aggregated FSS (eFSS) and Dispersion FSS (dFSS)

The concept of the fractions skill score could also be applied to the whole ensemble system. In this section, the ensemble-aggregated FSS (eFSS; Section 2.4.3) was used to evaluate all 32 ensemble members as a whole. The verification was conducted on the 6-hour precipitation from 08 LST to 20 LST with the threshold of 30 mm/6hr. **Figure 6.6a** shows that the eFSS increased from 0.6 to 0.99 as the spatial scale converted from the grid size to the whole domain. This pattern was similar to that of a single member (**Fig. 6.1**). $eFSS_{uniform}$, the criteria of the skillful scale, was obtained by averaging the $FSS_{uniform}$ in all time intervals and indicated that the skillful resolution of the ensemble system could reach 10 km at the time interval from 12 LST to 18 LST. Such spatial scale was roughly the mean value of the results evaluated on every single member in **Figure 6.4**, demonstrating that although we could not obtain the best prediction by viewing all ensemble members as a whole, an acceptable result on quantitative precipitation could be provided before the convection occurred in reality.

In addition to the mean state of ensemble skill provided by the eFSS, the ensemble spread was given to realize whether the diversity among the members was wide enough or not. The concept of dFSS (Section 2.4.3) was applied here to evaluate the ensemble spread, and the resulting pattern of dFSS (**Fig. 6.6b**) was much similar to the eFSS in **Figure 6.6a**. The method of deciding the control member (E05) was explained in detail



in Chapter 2. The definition of $dFSS_{uniform}$ is the same as the $eFSS_{uniform}$ in the previous paragraph, except that the observation was replaced by the control member (E05). From 09 LST to 18 LST, the dFSS at the grid scale (1 km) is higher than $dFSS_{uniform}$, suggesting that the rainfall fields in the ensemble members resemble the control member. However, we could not interpret the degree of spread only through the value of dFSS. It should be compared to the eFSS to determine whether the spread is appropriate (Eq. 2.13). The optimal ensemble spread during the heavy rainfall was at the spatial scale of 90 km, where the difference between eFSS and dFSS was perfect zero (Fig. 6.6c). The performance tended to be underspread near the grid scale (1 km), where the dFSS was higher than the eFSS. It will be proved in the next section that the underspread was caused by the terrain-locking effect. On the other hand, the signal of overspread was observed at the domain scale (>90 km), which implicitly indicated that the frequency bias was too divergent within the ensemble system.

6.1.3 Localized FSS (LFSS)

The verification in the previous sections ignored the spatial information of the forecast skill. Therefore, LFSS (Section 2.4.3) was used here to examine the spatial distribution of the QPF performance over northern Taiwan. **Figure 6.7** shows the LFSS of 6-hour accumulated precipitation from 08 LST to 20 LST in each ensemble member. The location



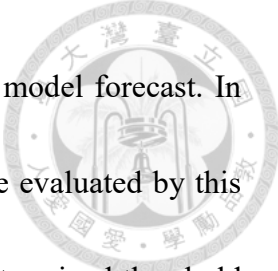
of high LFSS mainly corresponded to the overlapping area between the observational (Fig. 3.8) and forecasted rainfall field (Fig. 6.2).

After averaging the LFSS on each member, an apparent tendency was found in Figure 6.8. The high performance was centered at the SMR, while the diversity mainly occurred at the lower terrain such as the Taipei Basin and the northeast offshore. This phenomenon could be explained by the physical processes discussed in Chapter 5. The thunderstorm was initiated at the SMR in both the observation and all ensemble members. Therefore, a higher score with less ensemble spread was found here. However, the precipitation near the estuary of Tamsui River was only predicted by the members with ECMWF ERA5 initial condition (E17~E32). The missing in the NCEP FNL members (E01~E16) was caused by the weaker convergence between the thunderstorm cold pool and the sea breeze, so the LFSS at Tamsui River Valley was lower and more divergent. In addition, the diversities of the forecast skill near the northeast coast were brought by the different southward movements of the Mei-Yu front and determined by different initial conditions (Chapter 5).

6.2 Method for Object-based Diagnostic Evaluation (MODE)

6.2.1 Identifying and Pairing the Areas

The MODE method verified the QPF results by explicitly comparing the



characteristics of the rainfall areas between the observation and the model forecast. In this section, the 6-hour precipitation from 12 LST to 18 LST will be evaluated by this method. We first identified the rainfall areas that exceeded the predetermined threshold of 30 mm/6hr. As shown in **Figure 6.9c**, a larger area over northern Taiwan (A1 hereafter) and a much smaller one at the East China Sea (A2 hereafter) were identified from observation. The rainfall areas within all 32 ensemble members are shown in **Figure 6.10** and will then be matched to the observational areas by the criteria in **Eq. (2.17)**. Three matching types were defined after pairing (**Fig. 6.9**). All members successfully predicted A1, but 23 of them, classified as type 1, missed A2. Four members, labeled type 2, predicted both A1 and A2 while these two areas were connected. The members labeled type 3 could successfully predict A1 and A2 separately and resemble the observation the most. However, only 4 of the members were in this category. In the following analysis, only the rainfall area over northern Taiwan (A1) was analyzed since it is the main target in this study. The observed centroid in type 2 was slightly shifted to the northeast compared to the other two types (**Figure 6.11**) due to the connection of A2. Hence the following results will be weighted by the number of members in each type.

6.2.2 Errors of the Geometric Characteristics

Four kinds of geometric errors, including centroid distance, centroid azimuth, axis



orientation, and size, were evaluated in this section. The centroids in all ensemble members were plotted on the map with the axis orientation in **Figure 6.11**. The quantitative results of all these errors (**Fig. 6.12**) showed that the distance between the observational and forecasted centroids was 17 km on average and ranged from 2 km to 27 km. The azimuth errors concentrated between 90° and 180° , indicating that most centroids were located in the southeastern quadrant of the observation. Such systematic bias toward the SMR was consistent with what had been found in the physical processes (Chapter 5) and the verification results from LFSS (Section 6.1.3).

When it comes to the error of axis orientation, the positive error means the counterclockwise rotation while the negative means the other way. **Figure 6.12** shows that the more southeast the centroid, the more negative the orientation error, which can also be found in **Figure 6.11** that the axis tended to be more east-west oriented as the centroid moved southeastward. This kind of error mainly occurred in the members with the NCEP FNL initial conditions (E01~E16) due to the earlier arrival of the Mei-Yu front. As the front moved southward earlier in this time interval, the rainfall inside the Taipei Basin decreased and those at the northeast coast near the front increased, which could eventually cause the axis to turn clockwise with the centroid moving southeastward simultaneously.



6.2.3 Errors of Rainfall Intensity

After evaluating the exterior of the rainfall areas, the next important issue to be explored was what mattered inside them. Although the stochastic essence of the convective system limited the model performance on the location of maximum rainfall, if the rainfall intensity could be correctly forecasted, some precautions could be taken before the disaster took place. Since the size of the rainfall area differed from member to member, the probability density function (PDF) was used to standardize the coverage at each rainfall intensity.

Figure 6.13 shows the PDF of observed rainfall and ensemble model forecast. On the one hand, the PDF of gauge-corrected QPE (red solid line) was compared to that of the model QPF (blue solid line). The spread near 30 mm/6hr on the observational rainfall PDF was brought by the subtle area difference between the three matching types (**Fig. 6.9**) in the previous section. It shows that the model tended to predict too many grids on lower intensity (0~100 mm/6hr) but underestimate the area of heavy rainfall (>100 mm/6hr). However, the distribution of maximum rainfall intensity in **Figure 6.14** indicated that the 6-hour maximum rainfall was not underestimated. The maximum observational 6-hour precipitation (222 mm/6hr) fell almost at the middle (50 %) of the distribution, which implied that the discrepancy of the PDF in **Figure 6.13** might be caused by other factors rather than the underestimation of the extreme value. The



systematic bias in the model with too much rainfall concentrated on the mountain led to this mismatching of PDF curves. The decreasing coverage of heavy rainfall aside from the mountainous area could increase the fraction of moderate rainfall, consistent with that observed in the analysis of physical processes (Chapter 5) and the results of LFSS (Section 6.1.3).

On the other hand, the PDF of the observational data from 284 rain gauges (red dashed line) and the averaged PDF of the corresponding grid data from the ensemble members (blue dashed line) were analyzed. The mean PDF of the model-gauge data shifted slightly to the right due to the missing of the precipitation over the ocean, which dropped the grids with medium rainfall intensity (30 mm/6hr to 50 mm/6hr) offshore and retained the others with higher accumulated precipitation on the land. This right shift of PDF was much more apparent in the PDF of gauge data (red dashed line). In addition to the missing of precipitation information over the sea, the much less gauge sampling size (284) than the QPE grids (4134) contributed to this discrepancy. The non-uniform distributed gauges were primarily located in the heavy rainfall area (**Fig. 3.8**), which led to this significant right-shifted bias. Therefore, the rainfall intensity verification between the gauge-corrected QPE (red solid line) and the 2-dimensional model QPF data (blue solid line) were more reliable.

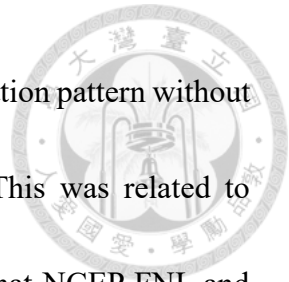


6.3 Hierarchical Clustering

The verification methods used in the previous sections mainly focused on the skill of individual members. In this section, we would like to explore what configuration in **Table 2.1** contributes more to the similarity of the rainfall patterns. To achieve this goal, the ensemble members will be categorized into several groups by hierarchical clustering of the 6-hour accumulated precipitation from 12 LST to 18 LST.

First, the correlation coefficients (CC) between any two rainfall fields of the ensemble members were calculated to quantify the similarity. Then the virtual distance (D), defined as $1-CC$, could be derived. The distance value ranges from 0 to 2, of which 0 means two identical rainfall fields while 2 represents two negative correlated patterns. A dendrogram could then be created based on the correlation coefficients and the distances (**Fig. 6.15**). **Figure 6.15a** indicates that the first hierarchy was sharply divided by the initial condition used, that is, NCEP FNL or ECMWF ERA5. The branch of NCEP FNL was shorter, meaning that these 16 members were more similar, while those with the ECMWF ERA5 were more diverse. The corresponding pattern could also be observed in **Figure 6.2** that the initial conditions influenced the general rainfall pattern a lot. The second hierarchy was produced by different combinations of microphysics schemes and cumulus schemes. However, the distances showed that the differences were subtle compared to that caused by the initial conditions.

In summary, the initial conditions influenced the overall precipitation pattern without regard to which microphysics and cumulus schemes were used. This was related to different features of the synoptic environment (i.e., Mei-Yu front) that NCEP FNL and ECMWF ERA5 brought about. More diversities were introduced as the different cumulus and microphysics schemes were involved since the mesoscale processes, such as solar heating, sea breeze, and cold pool, were more sensitive to these configurations.



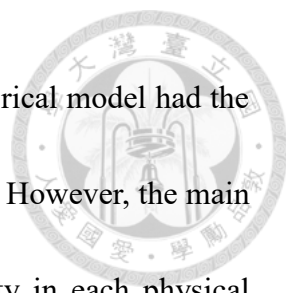
Chapter 7. Conclusions and Recommendations for Future Work



7.1 Conclusions

This study focused on the afternoon thunderstorm event on 4 June 2021 in the Taipei Basin. The ensemble predictions were conducted to investigate the uncertainty within this high spatiotemporal varied event. Different initial conditions, cumulus parameterizations, and microphysics schemes were used to examine their influences on the involving physical mechanisms. The analysis targets include the synoptic environment, mesoscale processes, and precipitation results. FSS and MODE methods were applied to quantitatively evaluate the characteristics of the QPF results.

The environment and the thunderstorm evolution were analyzed by the observational data first. A Mei-Yu front was located near the northern coast of Taiwan, and a typhoon was at the southwest corner, so the environment could not be considered as “weak synoptic” in this case. However, the front lingered offshore and the synoptic wind field in northern Taiwan was relatively weak. Therefore, the local circulation dominated in the Taipei Basin. The sea breeze circulation along the Tamsui River Valley (TRV) in the morning and its interactions with the thunderstorm outflow in the afternoon were crucial to determining whether the heavy rainfall could occur in the basin. The resulting accumulated precipitation showed two hotspots. One was along the Snow Mountain Range (SMR), and the other was at the southeast corner of Taipei Basin.



As shown in the analysis of member E17 (Chapter 4), the numerical model had the chance to reproduce the physical processes and the resulting rainfall. However, the main objectives of this study were to understand the forecast uncertainty in each physical process and what factors caused these spreads. The analyses were separated into three parts: (1) synoptic environment, (2) mesoscale processes, and (3) QPF results. The schematic diagrams from **Figure 7.1 to Figure 7.3** integrate the critical physical mechanisms in the event and the corresponding factors that caused the ensemble diversities.

The synoptic environment near northern Taiwan was significantly influenced by the location of the surface Mei-Yu front. Initial conditions dominated the frontal line without regard to which cumulus scheme and microphysics scheme were applied. The Mei-Yu front in NCEP FNL members (E01~E16) moved faster, and the environment tended to be colder and dryer. On the contrary, the frontal line in ECMWF ERA5 members (E17~E32) moved slower, which caused the wetter and warmer low-level environment and much more favorable for thunderstorm development.

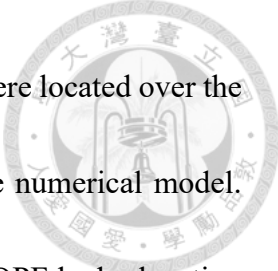
Despite the similar location of the surface front with the same initial condition, the microphysics schemes significantly affected the high cloud pattern. Morrison scheme produced too much hydrometeor at the upper level, causing more and thicker high clouds over the Taipei Basin, while the Thompson scheme showed the opposite extreme. WDM6

and Goddard performed more similarly to the observation. These characteristics were independent of the initial conditions used.



These ensemble diversities could be transported by the relationship between the synoptic environment and the mesoscale processes (**Fig. 5.1**). The heating in the morning was influenced by both the initial conditions and the microphysics schemes. The initial conditions dominated mean state temperature through the synoptic environment around the Taipei Basin, while the microphysics scheme controlled the heating time phase by the high cloud pattern. The resulting sea breeze further reflected these diversities. The Morrison members showed a later onset of the sea breeze with the corresponding delayed solar heating. However, the signal of the thunderstorm cold pool was more affected by initial conditions. The warmer ECMWF members were more favorable for developing density current, which led to producing thicker cold pools in the Taipei Basin. In contrast, the cooler NCEP members caused the cold pool in the basin to be thinner and weaker. These characteristics of thunderstorm cold pools further influence whether the precipitation can occur in the basin since it is the most significant lifting mechanism in the plain area.

For the QPF verification, FSS revealed that although the horizontal grid size was up to 1 km, the valuable information could be coarser and ranged from 1 km to 21 km. The differences between eFSS and dFSS showed that the ensemble system was slightly



underspread at the grid scale (1 km). The grids with the higher skill were located over the SMR by LFSS, which resulted from the terrain-locking effect in the numerical model. MODE, the other QPF verification method, showed that the model QPF had a location bias toward the SMR, which was the same as the results from FSS method. The distance error ranged from 2 km to 27 km, and the orientation error was determined by the frontal precipitation on the northeast coast. The hierarchical clustering demonstrated again that the initial conditions determined the main pattern of the precipitation area, and the combination of the cumulus scheme and the microphysics parameterizations contributed more to the diversities in the ensemble system. These results were consistent with what has been found in the physical processes.

7.2 Recommendations for Future Work

This study investigated the ensemble characteristics of several critical mechanisms in the afternoon thunderstorm event in the Taipei Basin on 4 June 2021. Although the synoptic environment near northern Taiwan was mainly influenced by the Mei-Yu front on the northern side, the influences of Typhoon Choi-Wan (2021) on the southwest corner of Taiwan and its interactions with the Mei-Yu front were not discussed. More analyses on how the typhoon contributed to this event can be investigated in both the observational and the modeling aspects in the future. Besides, what was examined in this study was



mainly located in northern Taiwan. According to the observation, severe afternoon thunderstorms also occurred in central and southern Taiwan. The similarities and the differences of the afternoon thunderstorms between different regions of Taiwan under the same synoptic environment can also be investigated in the future.

On the topic of ensemble prediction, the configurations of the ensemble members have only considered the variations of the initial conditions, cumulus schemes, and microphysics schemes. Other physical parameterizations such as planetary boundary layer (PBL) and the radiation can also be taken into account since they might affect the physical mechanisms of the afternoon thunderstorms. Other techniques for establishing the ensemble systems, such as different data assimilation methods and perturbed initial conditions, can be further included in the ensemble members to examine more possible forecast uncertainty to this event.

Last but not least, since the scope of this study is focused on the event on 4 June 2021, more thunderstorm cases should be considered in the future to further understand the physical mechanisms and the characteristics of ensemble predictions on the afternoon thunderstorm during the Mei-Yu season in Taiwan.

Reference



陳白榆，李志昕，葉天降，2018：物件基礎診斷校驗技術於中央氣象局區域模式定
量降水預報能力之初步評估結果。中央氣象局 107 年天氣分析與預報研討會，
A2-8。

Davis, C. A., B. G. Brown, and R. G. Bullock, 2006: Object-based verification of
precipitation forecasts. Part I: Methodology and application to mesoscale rain areas.

Mon. Wea. Rev., **134**, 1772–1784.

Dey, S. R. A., G. Leoncini, N. M. Roberts, R. S. Plant, and S. Migliorini, 2014: A spatial
view of ensemble spread in convection permitting ensembles. *Mon. Wea. Rev.*, **142**,

4091–4107.

Epstein, E.S., 1969: Stochastic dynamic prediction. *Tellus*, **21**, 739–759.

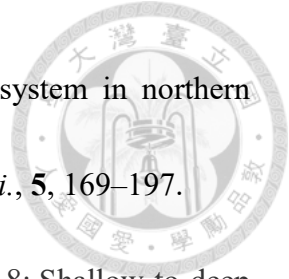
Ferrett, S., T. H. A. Frame, J. Methven, C. E. Holloway, S. Webster, T. H. M. Stein, and

C. Cafaro, 2021: Evaluating convection-permitting ensemble forecasts of
precipitation over southeast Asia. *Wea. Forecasting*, **36**, 1199–1217.

Gilleland E., D. Ahijevych, B. Brown, and E. Ebert, 2009: Intercomparison of spatial
forecast verification methods. *Wea. Forecasting*, **24**, 1416–1430.

Jeworrek, J., G. West, and R. Stull, 2021: WRF precipitation performance and
predictability for systematically varied parameterizations over complex terrain.

Wea. Forecasting, **36**, 893–913.



Jou, B. J.-D., 1994: Mountain-originated mesoscale precipitation system in northern Taiwan: A case study of 21 June 1991. *Terr. Atmos. Oceanic Sci.*, **5**, 169–197.

Kurowski, M. J., K. Suselj, W. W. Grabowski, and J. Teixeira, 2018: Shallow-to-deep transition of continental moist convection: Cold pools, surface fluxes, and mesoscale organization. *J. Atmos. Sci.*, **75**, 4071–4090.

Lai, Hsiao-Wei and Hong, Jing-Shan, 2021: Evaluation of Guidance for Quantitative Precipitation Forecast of the Central Weather Bureau (in Chinese). *Atmosphere*, **49**, 52-76.

Lin, P. F., Chang, P. L., Jong-Dao Jou, B., Wilson, J. W., & Roberts, R. D., 2012: Objective prediction of warm season afternoon thunderstorms in northern Taiwan using a fuzzy logic approach. *Weather and forecasting*, *27*(5), 1178-1197.

Lorenz, E.N., 1963: Deterministic Nonperiodic Flow. *Journal of Atmospheric Sciences*, **20**, 130-141.

Miao, J.-E., and M.-J. Yang, 2020: A modeling study of the severe afternoon thunderstorm event at Taipei on 14 June 2015: The roles of sea breeze, microphysics, and terrain. *J. Meteor. Soc. Japan*, **98**, 129–152.

Rezacova, D., P. Zacharov, and Z. Sokol, 2009: Uncertainty in the area-related QPF for heavy convective precipitation. *Atmos. Res.*, **93**, 238–246.

Roberts, N. M., and H. W. Lean, 2008: Scale-selective verification of rainfall



accumulations from high-resolution forecasts of convective events, *Mon. Wea. Rev.*, **136**, 78–97.

Rotunno, R., J. B. Klemp, and M. L. Weisman, 1988: A theory for strong, long-lived squall lines. *J. Atmos. Sci.*, **45**, 463–485.

Seitter, K. L., & Muench, H. S. 1985: Observation of a cold front with rope cloud. *Mon. Wea. Rev.*, **113(5)**, 840-848.

Skamarock, W. C., Klemp, J. B., Dudhia, J., Gill, D. O., Barker, D., Duda, M. G., ... Powers, J. G. 2008: A Description of the Advanced Research WRF Version 3 (No. NCAR/TN-475+STR). *University Corporation for Atmospheric Research*.

Wakimoto, R. M., 1982: The life cycle of thunderstorm gust fronts as viewed with Doppler radar and rawinsonde data. *Mon. Wea. Rev.*, **110**, 1060–1082.

Weisman, M. L., and R. Rotunno, 2004: “A theory for strong long-lived squall lines” revisited. *J. Atmos. Sci.*, **61**, 361–382.

Woodhams, B. J., C. E. Birch, J. H. Marsham, C. L. Bain, N. M. Roberts, and D. F. A. Boyd, 2018: What is the added value of a convection-permitting model for forecasting extreme rainfall over tropical East Africa? *Mon. Wea. Rev.*, **146**, 2757–2780.

Zhang, J., and Coauthors, 2008: High-resolution QPE system for Taiwan. Data Assimilation for Atmospheric, Oceanic, and Hydrologic Applications, S. K. Park

and L. Xu, Eds., *Springer-Verlag*, 147–162.



Tables



Table 2.1 The configurations of all 32 ensemble members.

Member	IC/BC	cumulus scheme	microphysics scheme
E01	NCEP FNL	Kain-Fritsch	WDM 6-class
E02	NCEP FNL	Kain-Fritsch	Goddard
E03	NCEP FNL	Kain-Fritsch	Thompson
E04	NCEP FNL	Kain-Fritsch	Morrison
E05	NCEP FNL	Betts-Miller-Janjic	WDM 6-class
E06	NCEP FNL	Betts-Miller-Janjic	Goddard
E07	NCEP FNL	Betts-Miller-Janjic	Thompson
E08	NCEP FNL	Betts-Miller-Janjic	Morrison
E09	NCEP FNL	Grell 3D ensemble	WDM 6-class
E10	NCEP FNL	Grell 3D ensemble	Goddard
E11	NCEP FNL	Grell 3D ensemble	Thompson
E12	NCEP FNL	Grell 3D ensemble	Morrison
E13	NCEP FNL	Grell-Devenyi ensemble	WDM 6-class
E14	NCEP FNL	Grell-Devenyi ensemble	Goddard
E15	NCEP FNL	Grell-Devenyi ensemble	Thompson
E16	NCEP FNL	Grell-Devenyi ensemble	Morrison
E17	EC ERA5	Kain-Fritsch	WDM 6-class
E18	EC ERA5	Kain-Fritsch	Goddard
E19	EC ERA5	Kain-Fritsch	Thompson
E20	EC ERA5	Kain-Fritsch	Morrison
E21	EC ERA5	Betts-Miller-Janjic	WDM 6-class
E22	EC ERA5	Betts-Miller-Janjic	Goddard
E23	EC ERA5	Betts-Miller-Janjic	Thompson
E24	EC ERA5	Betts-Miller-Janjic	Morrison
E25	EC ERA5	Grell 3D ensemble	WDM 6-class
E26	EC ERA5	Grell 3D ensemble	Goddard
E27	EC ERA5	Grell 3D ensemble	Thompson
E28	EC ERA5	Grell 3D ensemble	Morrison
E29	EC ERA5	Grell-Devenyi ensemble	WDM 6-class
E30	EC ERA5	Grell-Devenyi ensemble	Goddard
E31	EC ERA5	Grell-Devenyi ensemble	Thompson
E32	EC ERA5	Grell-Devenyi ensemble	Morrison

Table 6.1 The skillful spatial scale of each ensemble member between 12 LST and 18 LST under the threshold of 30 mm/6hr aligned (a) in sequence and (b) by rank.

(a)	Member	Skillful Spatial Scale (km)	(b)	Member	Skillful Spatial Scale (km)
	E01	9.2		E24	1.0
	E02	10.6		E04	1.6
	E03	12.7		E32	2.3
	E04	1.6		E08	2.5
	E05	10.9		E17	2.6
	E06	9.3		E28	3.2
	E07	5.9		E20	3.3
	E08	2.5		E19	4.4
	E09	11.6		E16	5.1
	E10	18.6		E21	5.8
	E11	20.9		E07	5.9
	E12	6.4		E22	6.0
	E13	17.9		E18	6.1
	E14	11.0		E12	6.4
	E15	19.8		E30	7.3
	E16	5.1		E25	8.9
	E17	2.6		E01	9.2
	E18	6.1		E06	9.3
	E19	4.4		E02	10.6
	E20	3.3		E05	10.9
	E21	5.8		E14	11.0
	E22	6.0		E09	11.6
	E23	17.1		E29	11.9
	E24	1.0		E03	12.7
	E25	8.9		E26	13.4
	E26	13.4		E31	15.5
	E27	15.5		E27	15.5
	E28	3.2		E23	17.1
	E29	11.9		E13	17.9
	E30	7.3		E10	18.6
	E31	15.5		E15	19.8
	E32	2.3		E11	20.9

Figures

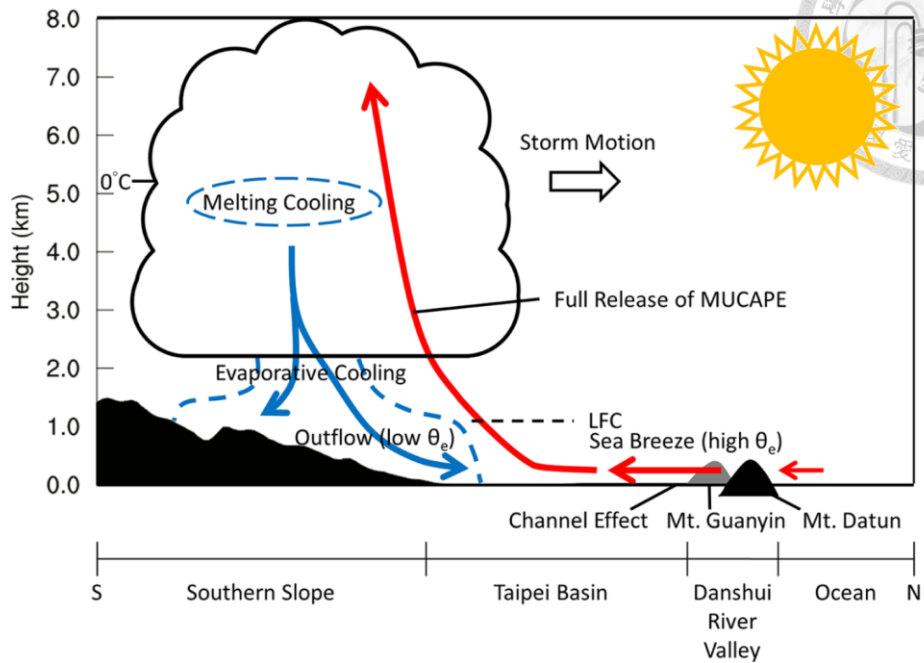


Figure 1.1 Schematic diagram of the crucial mesoscale mechanisms for Taipei afternoon thunderstorm initiation and development along the Tamsui River Valley (TRV). (Miao and Yang 2020)

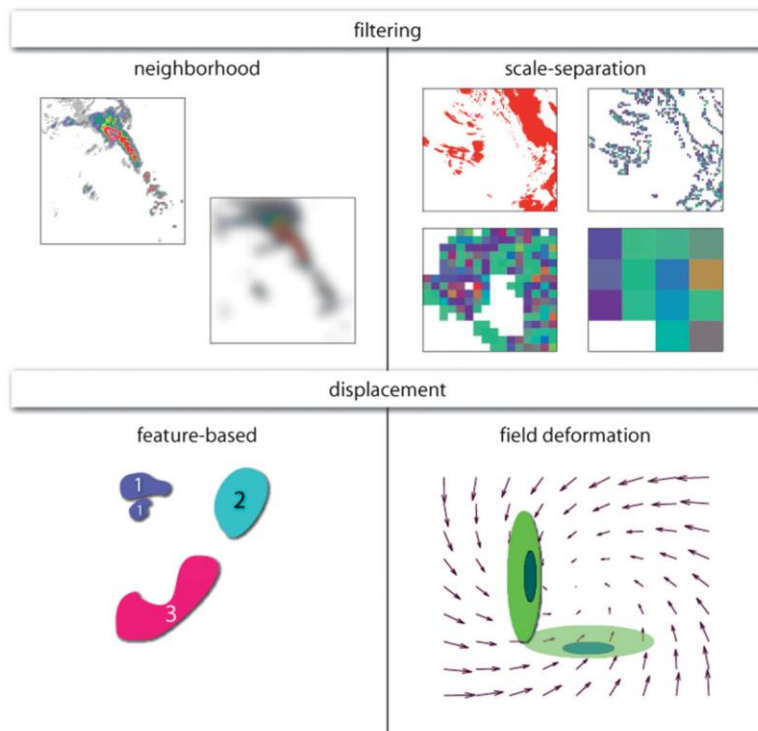


Figure 1.2 Two major categories and four minor classes of the QPF verification methods. (Gilleland et al. 2009)

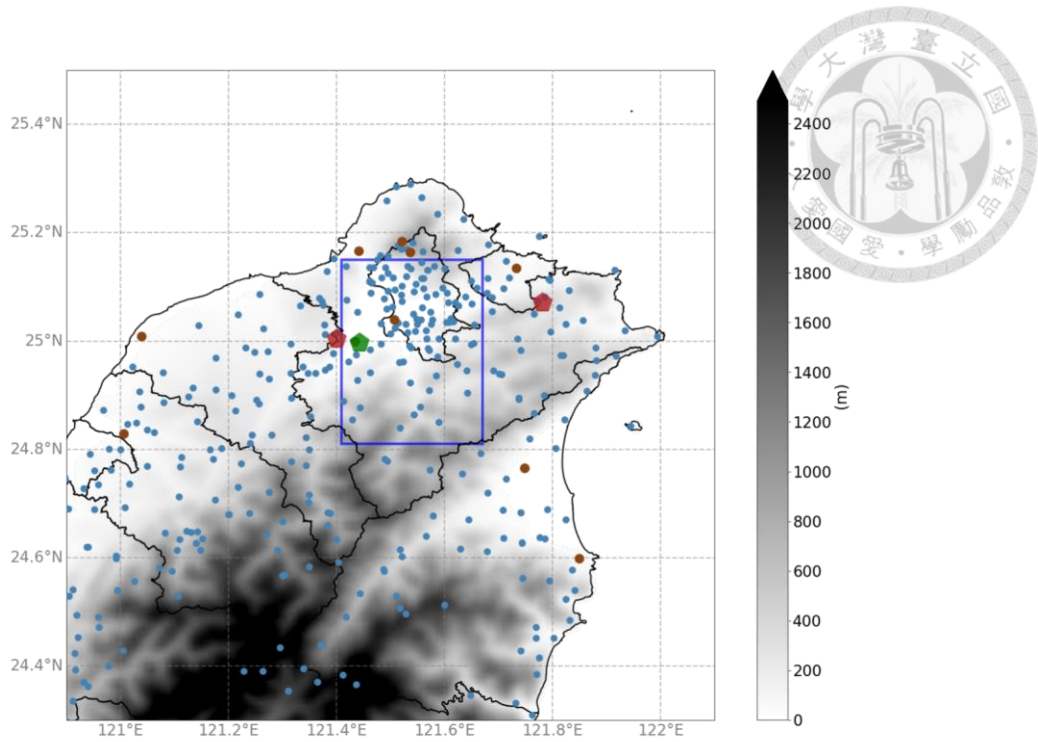


Figure 2.1 The locations of RCWF and RCSL radars (red polygons), Banqiao station (green polygon), CWB surface stations (brown dots), and automatic weather stations (blue dots). The blue box shows the area of the Taipei Basin.

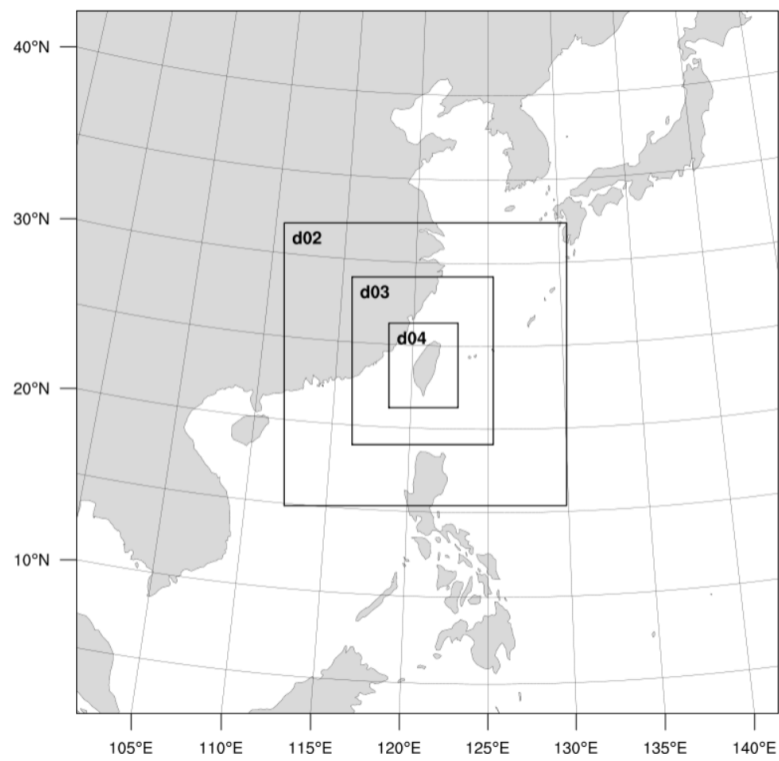


Figure 2.2 Four two-way nested domains of the model.

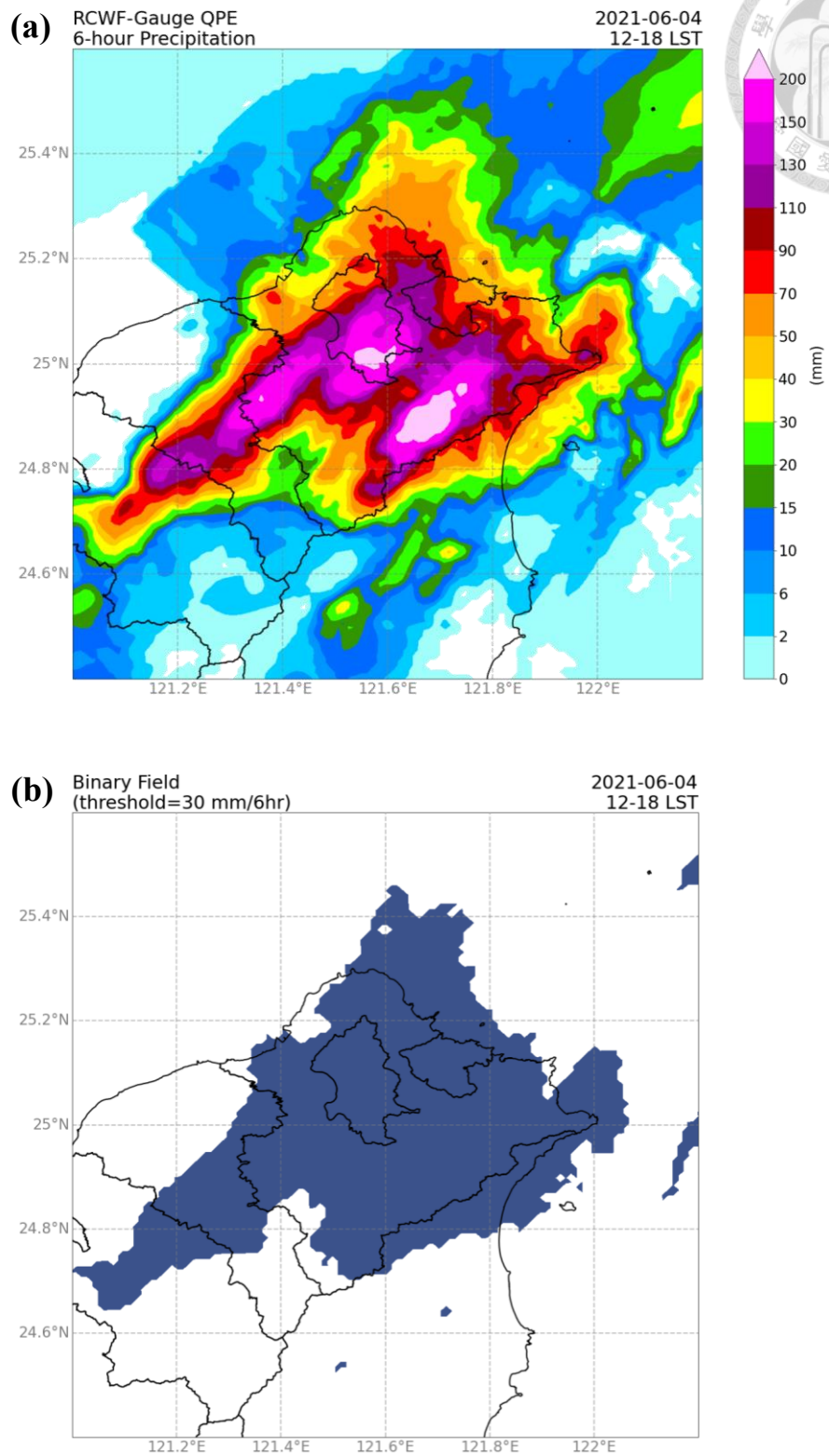


Figure 2.3 (a) 6-hour gauge-corrected QPE from 12 LST to 18 LST with (b) the corresponding binary field under the threshold of 30 mm/6hr.

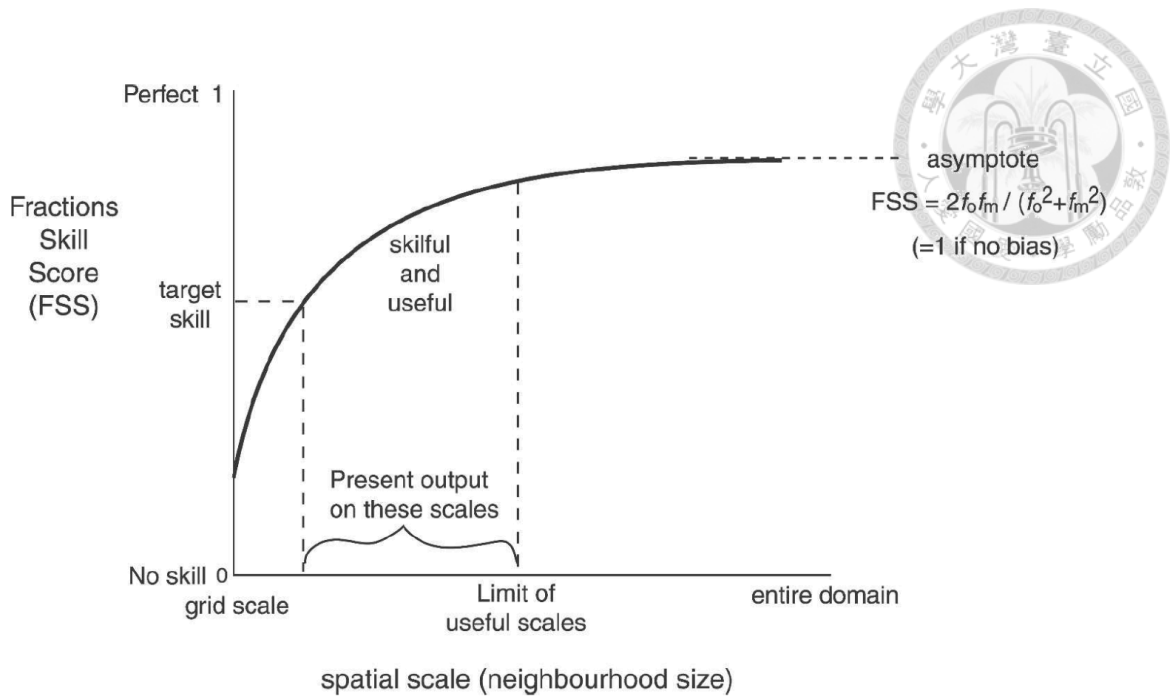


Figure 2.4 The FSS curve. (Roberts and Lean 2008)

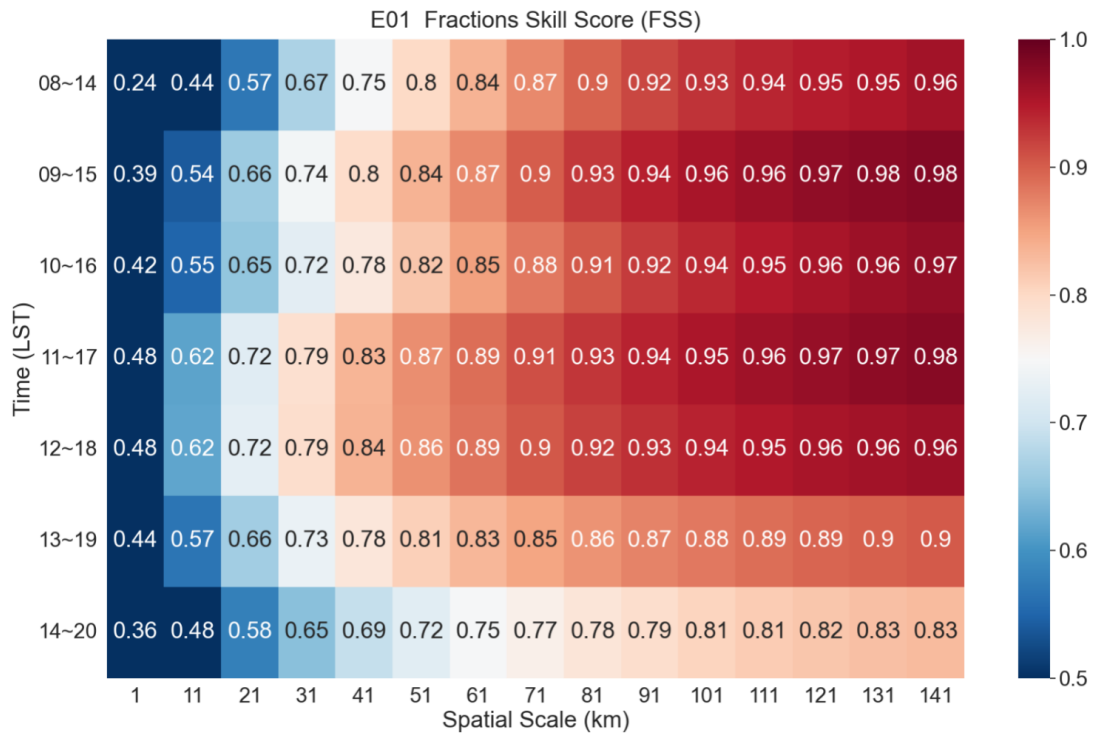


Figure 2.5 The FSS of 6-hour accumulated precipitation from 08 LST to 20 LST with the spatial scale between 1 km and 150 km in ensemble member E01.

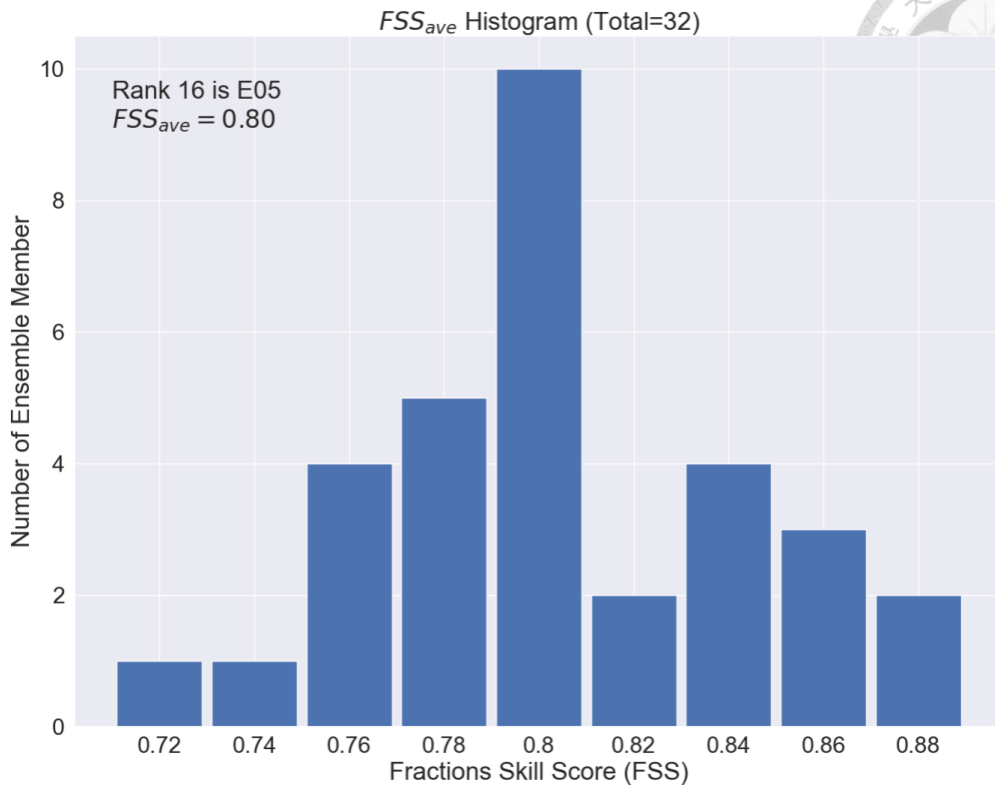


Figure 2.6 The histogram of FSS_{ave} .

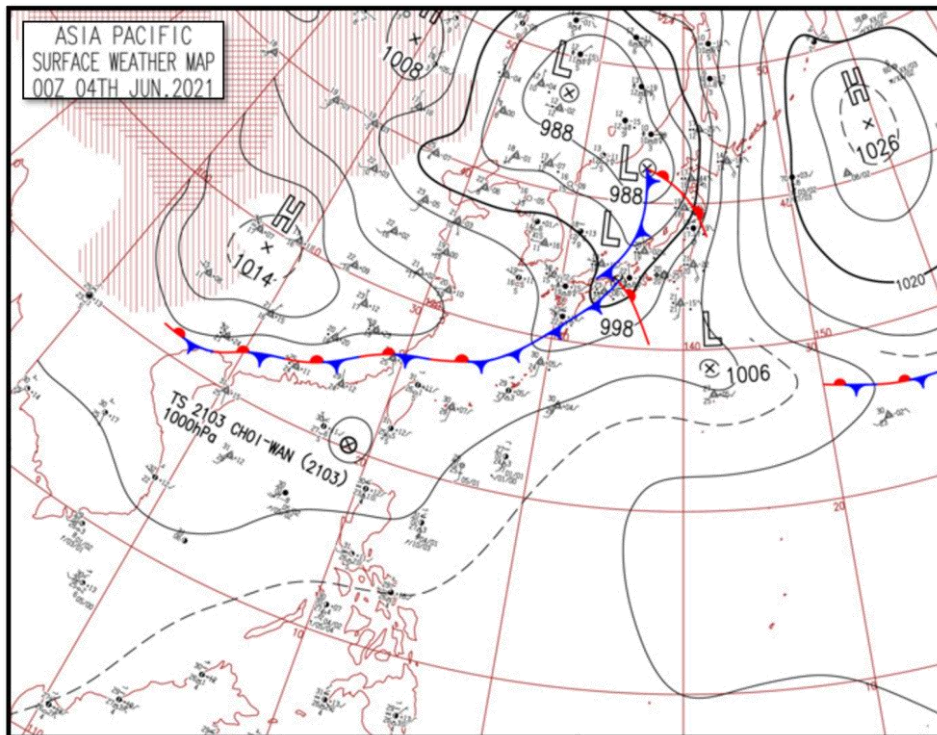


Figure 3.1 The JMA surface weather chart at 08 LST (00 UTC) on 4 June 2021.

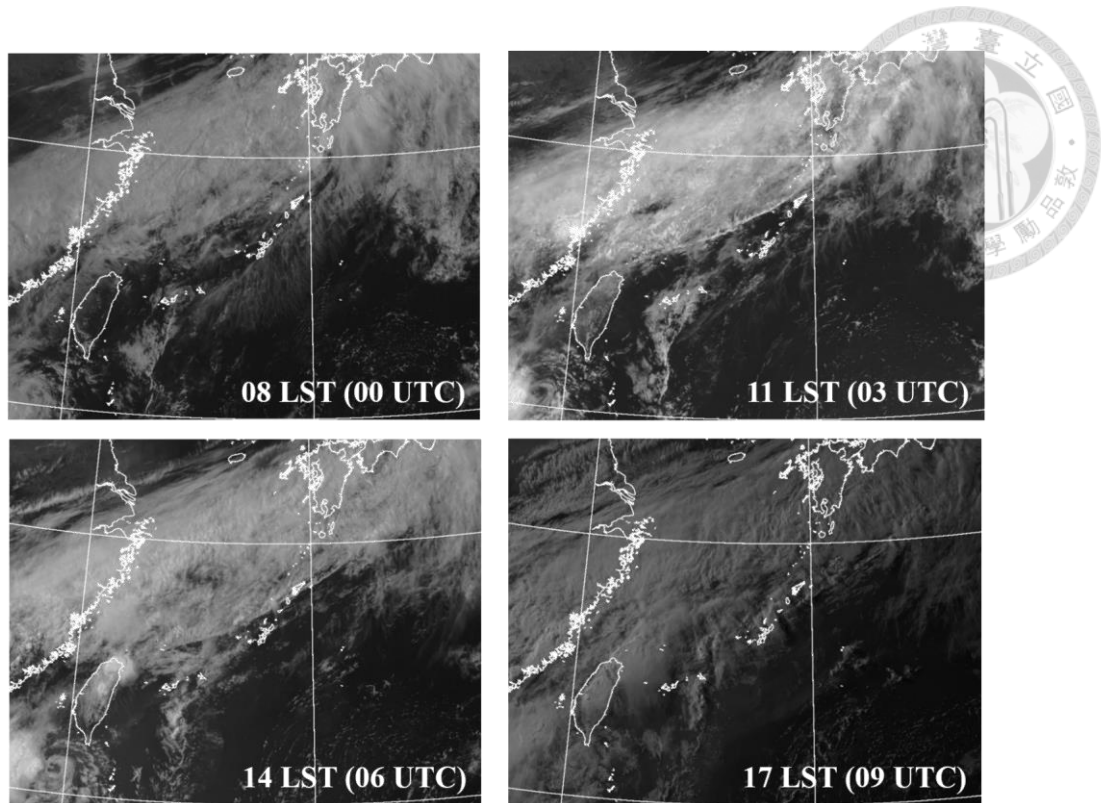


Figure 3.2 The Himawari-8 visible satellite images around Taiwan from 08 LST to 17 LST with 3-hour intervals.

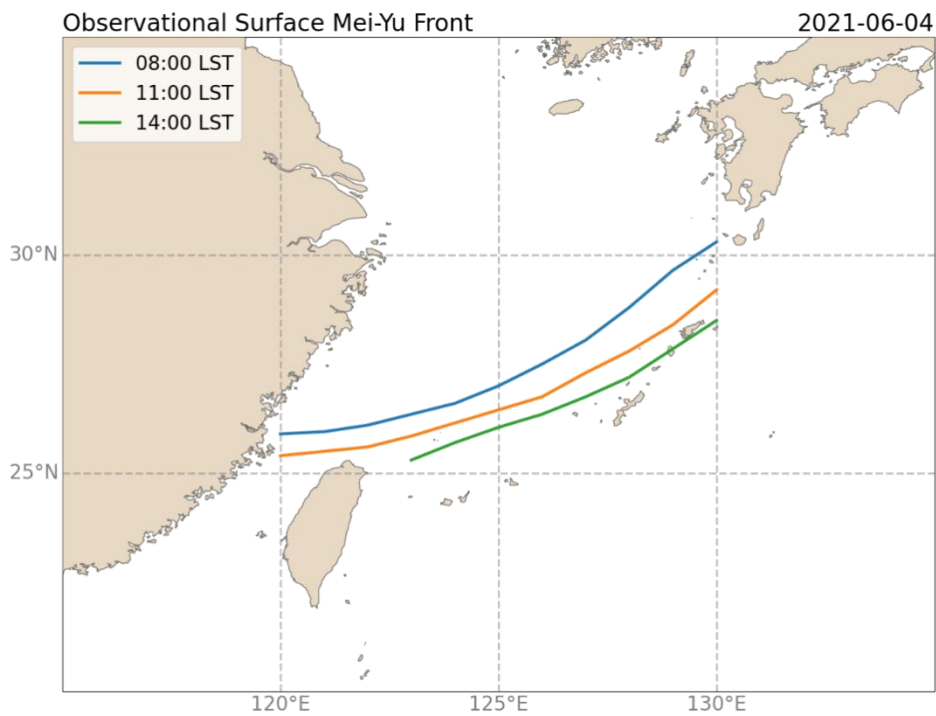


Figure 3.3 The identified observational surface Mei-Yu front at 08 LST (blue line), 11 LST (orange line), and 14 LST (green line).

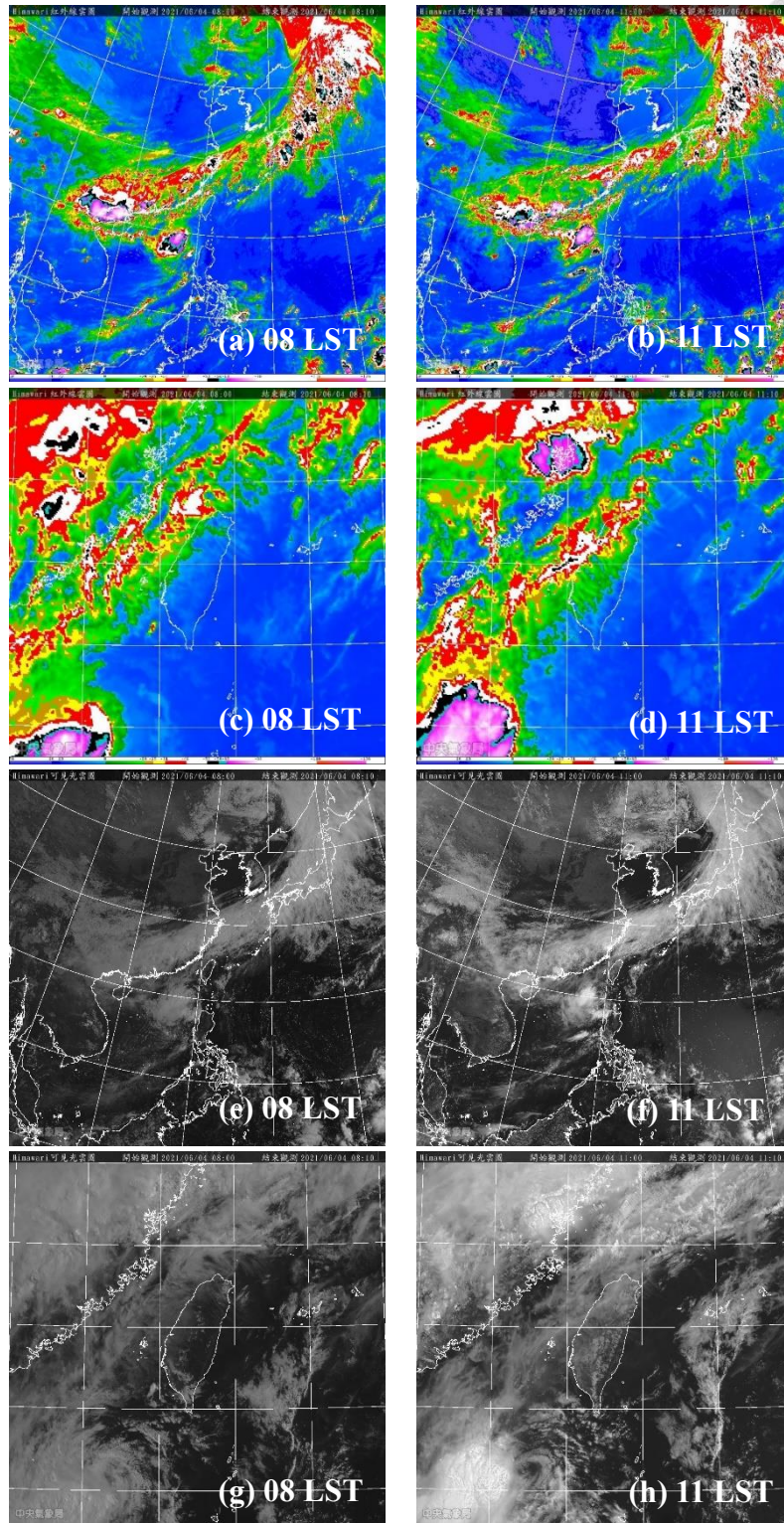
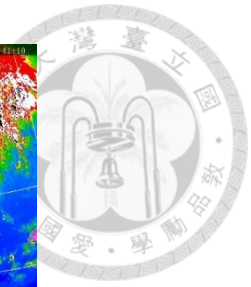


Figure 3.4 Himawari-8 infrared (top half) and visible (bottom half) satellite images at 08 LST (left half) and 11 LST (right half) with the domain of east Asia (subplots a., b., e., and f.) and Taiwan (subplots c., d., g., and h.).

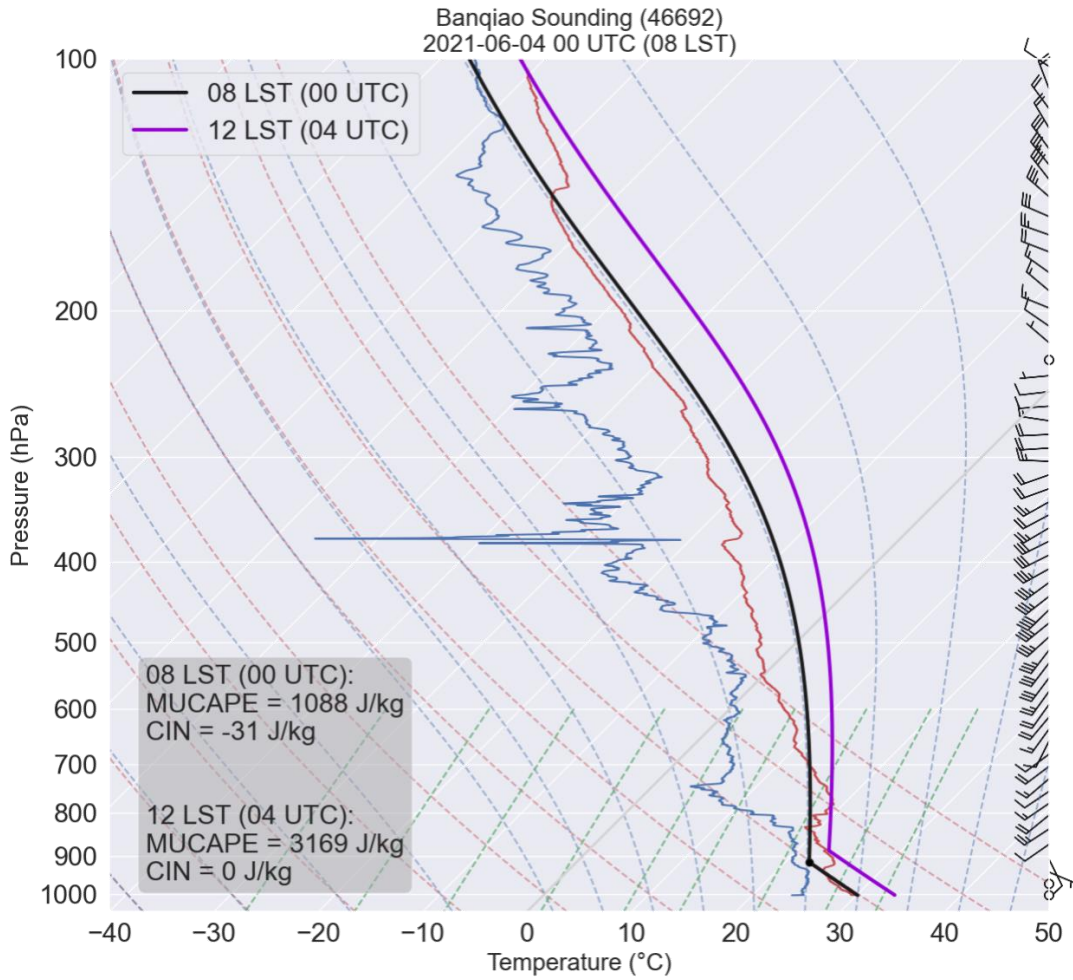


Figure 3.5 Banqiao sounding (46692) at 08 LST (00 UTC) with the lifting curve of 08 LST (00 UTC; black line) and 12 LST (04 UTC; purple line).

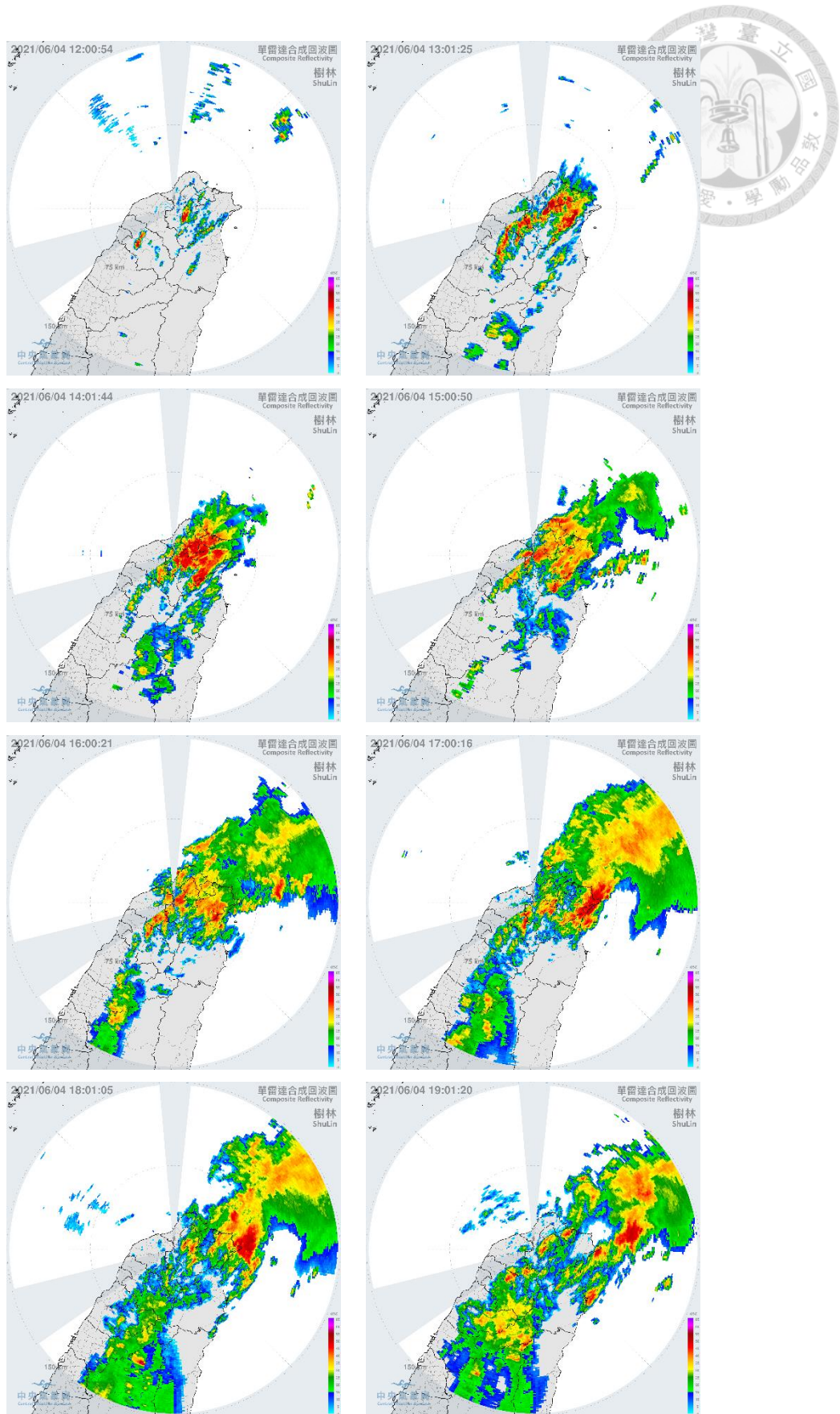


Figure 3.6 The hourly Shulin composite radar reflectivity from 12 LST to 19 LST.

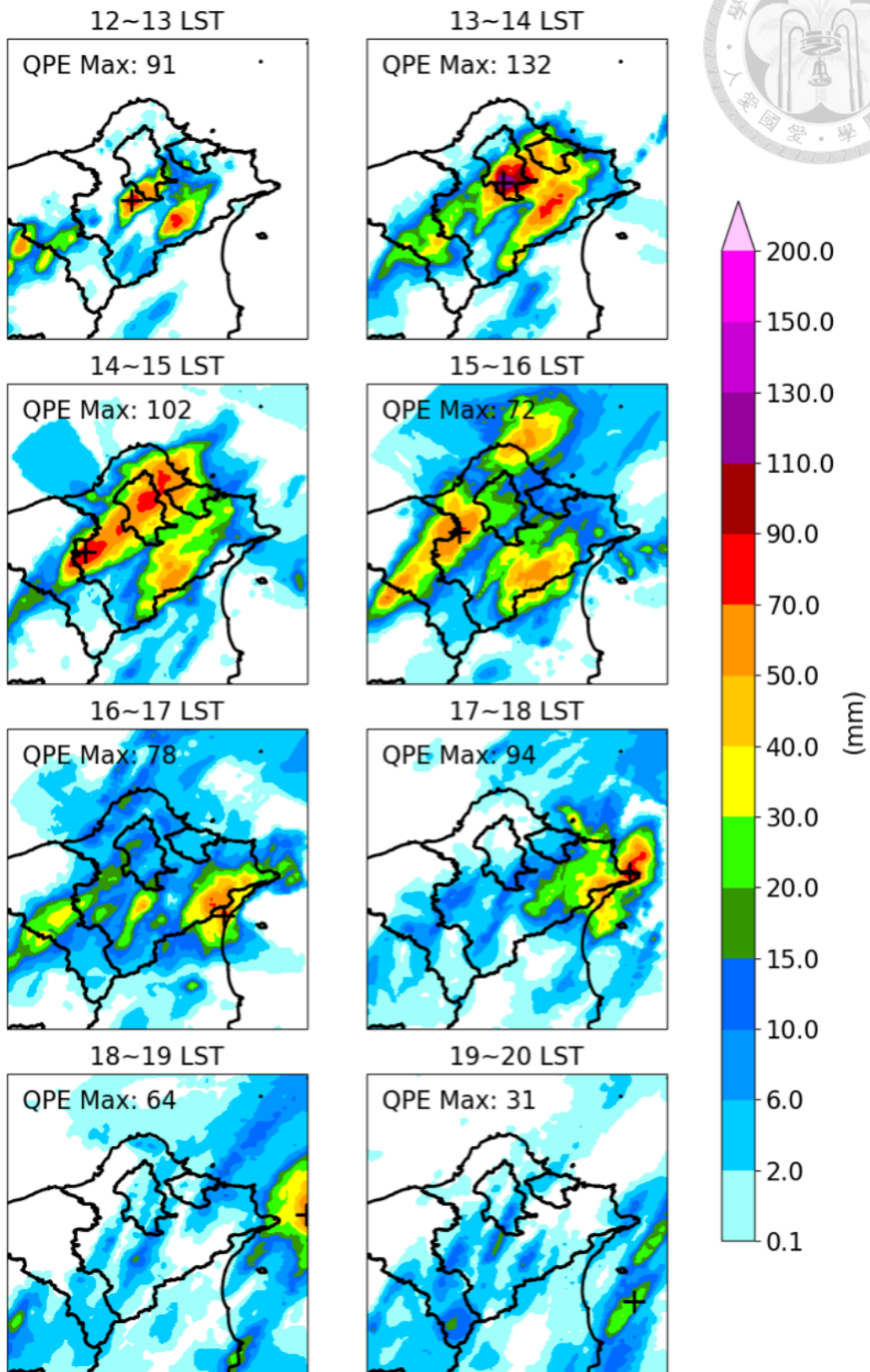


Figure 3.7 The hourly gauge-corrected QPE from 12 LST to 20 LST.

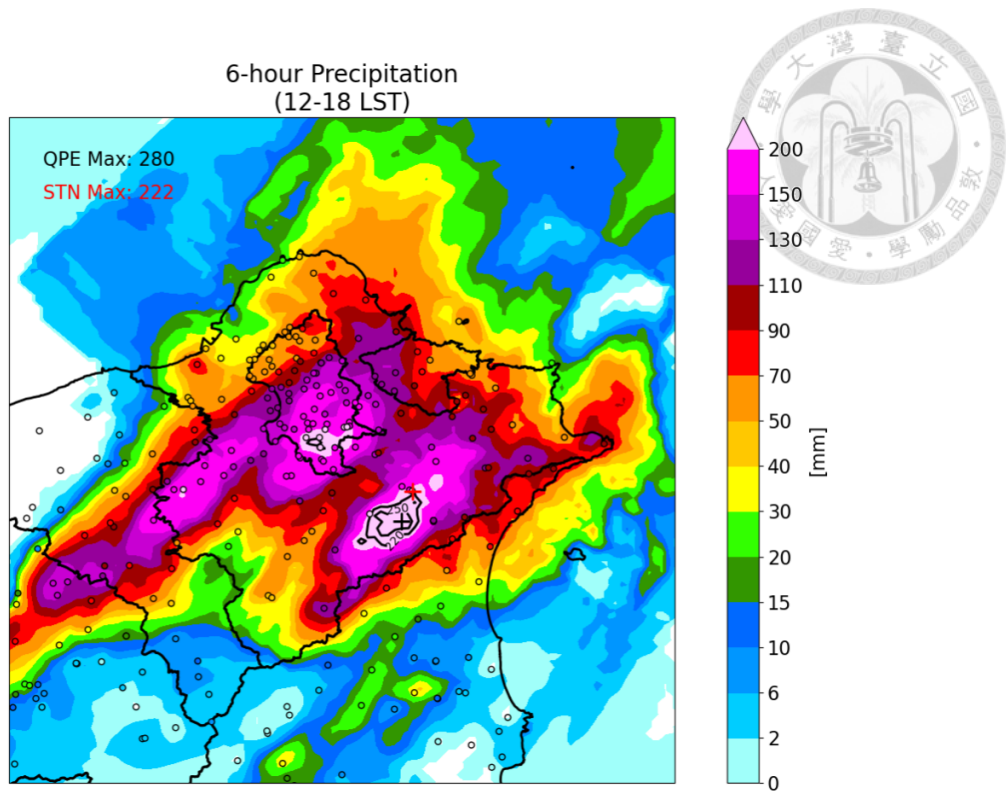


Figure 3.8 The 6-hour gauge-corrected QPE and the surface gauge observation from 12 LST to 18 LST.

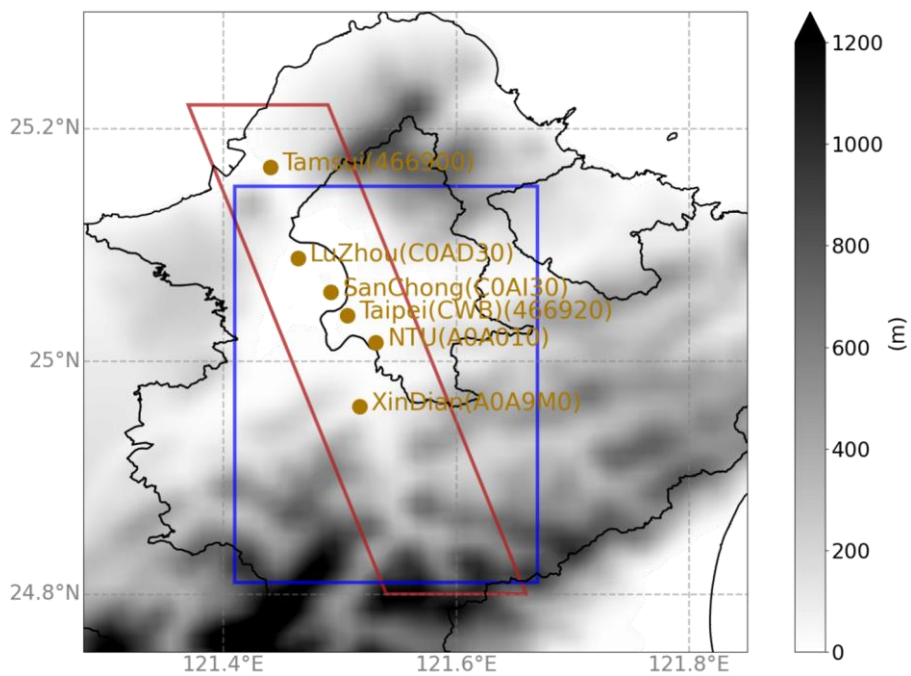


Figure 3.9 The definition of Tamsui River Valley (TRV; red box), Taipei Basin (blue box), and six CWB stations along the TRV (brown dots). The shading shows the topography.

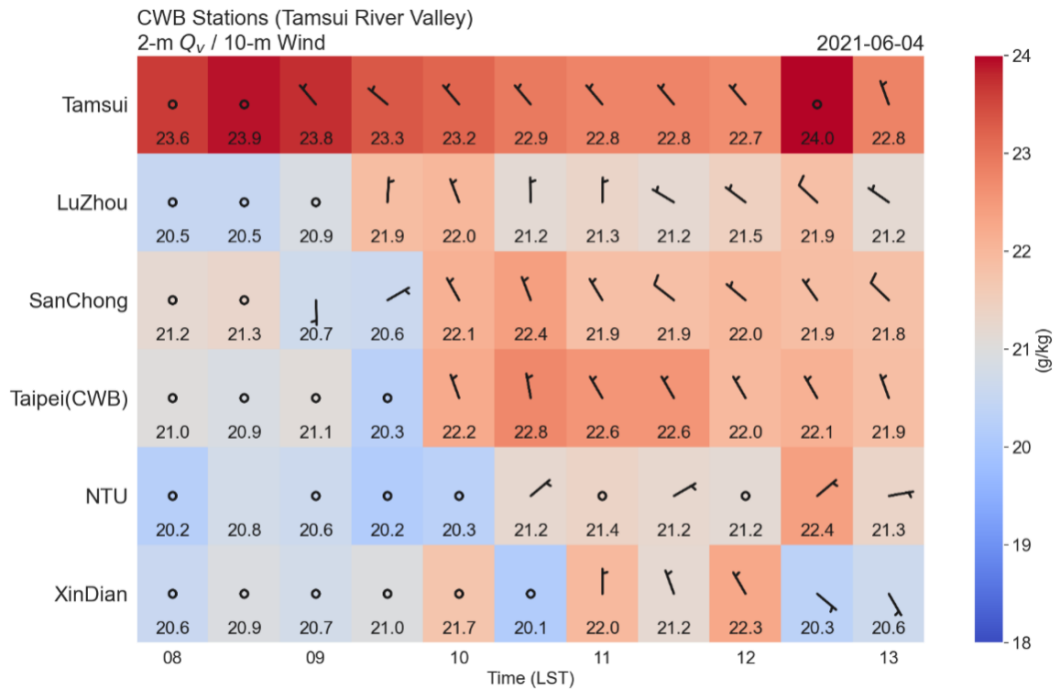


Figure 3.10 The time series of 10-m wind (barbs) and 2-m water vapor mixing ratio (color) at six TRV stations from 08 LST to 13 LST.

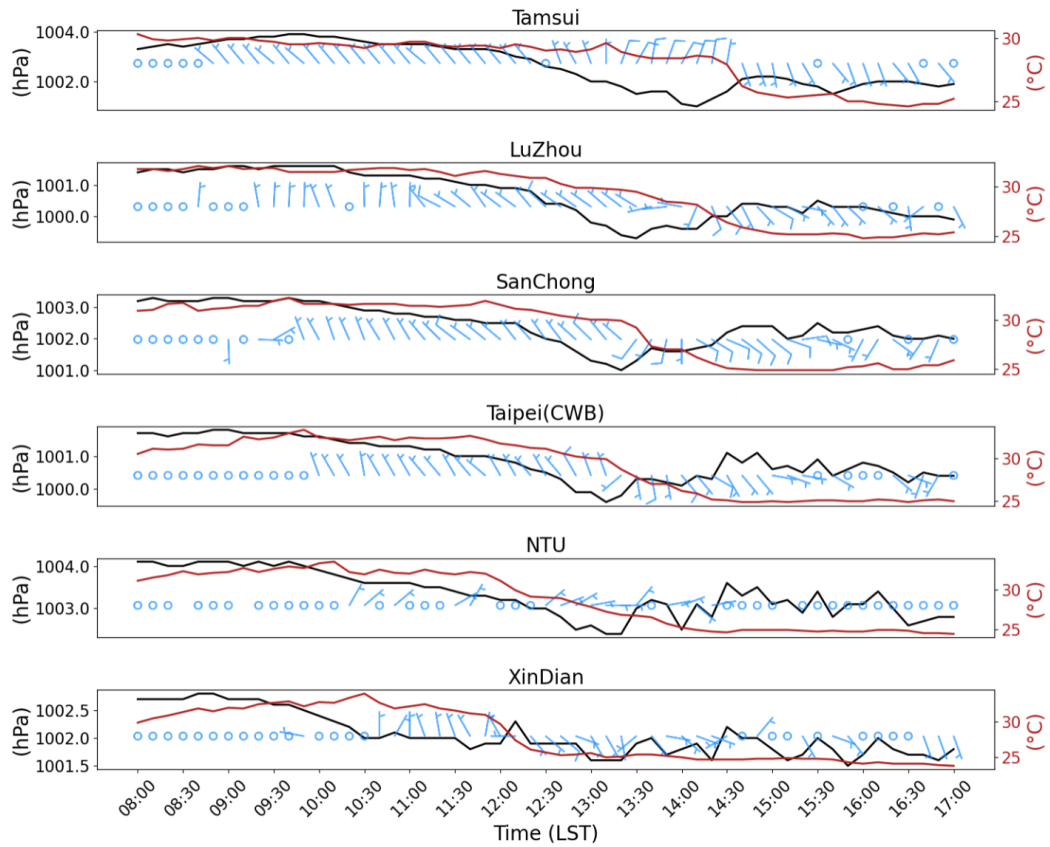


Figure 3.11 The time series of 10-m wind (barbs), 2-m temperature (red lines), and pressure (black lines) at six TRV stations from 08 LST to 17 LST.

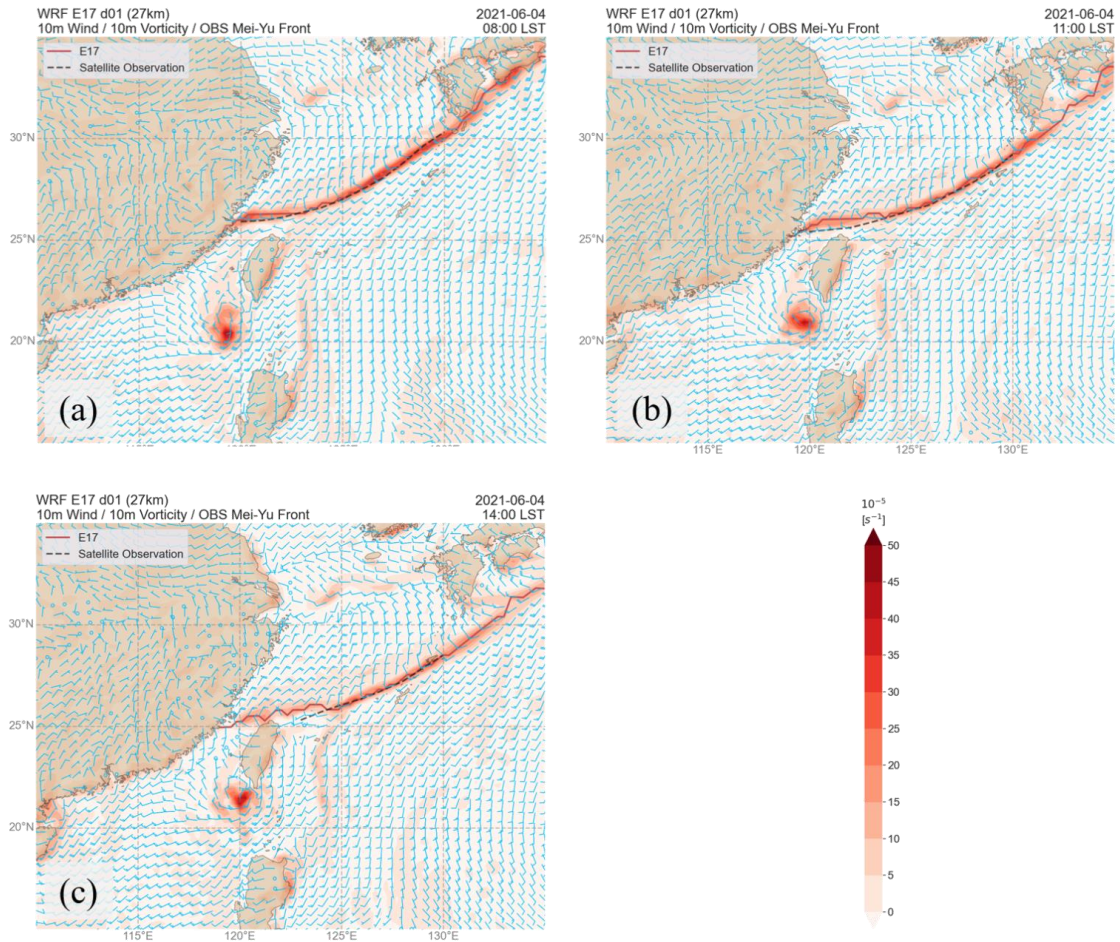
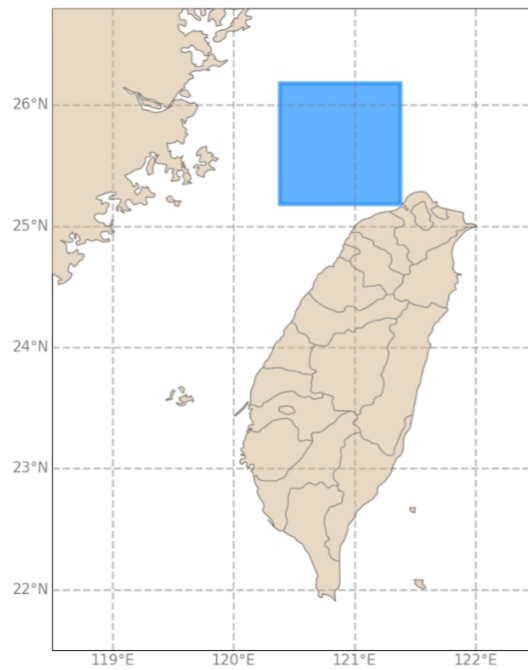


Figure 4.1 The 10-m wind (barbs), 10-m vorticity (color), and the corresponding surface Mei-Yu front (red line) in ensemble member E17 at (a) 08 LST, (b) 11 LST, and (c) 14 LST. The black dashed lines show the location of observational frontal line.



(a)



(b)

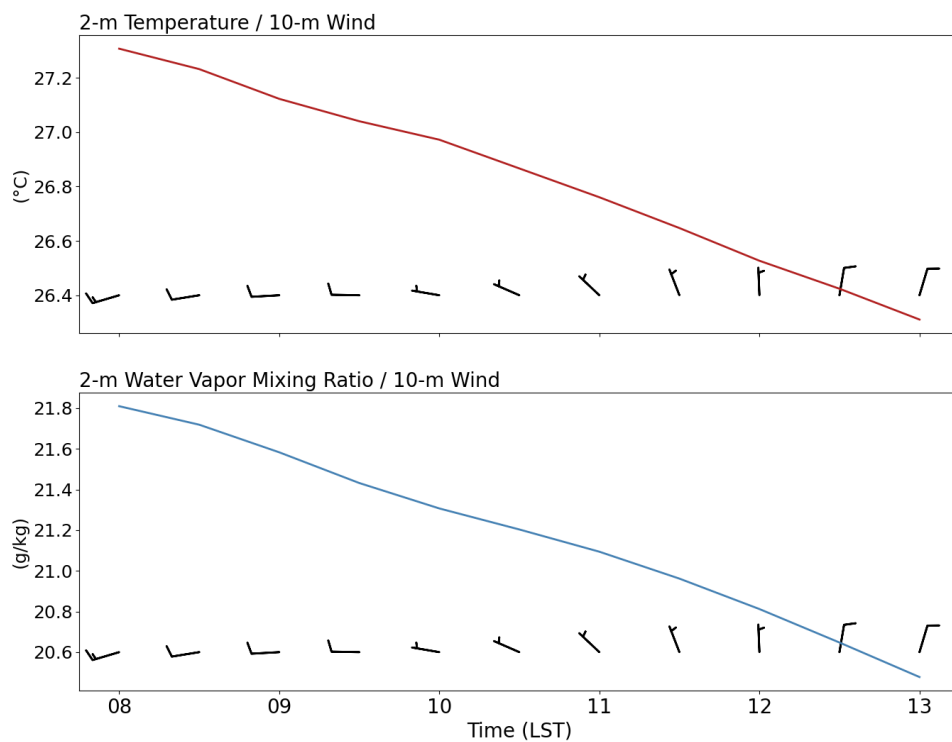


Figure 4.2 (a) The 1° by 1° box at northern Taiwan Strait. (b) The time series of averaged 10-m wind, 2-m temperature, and 2-m water vapor mixing ratio in the 1° by 1° box of ensemble member E17.

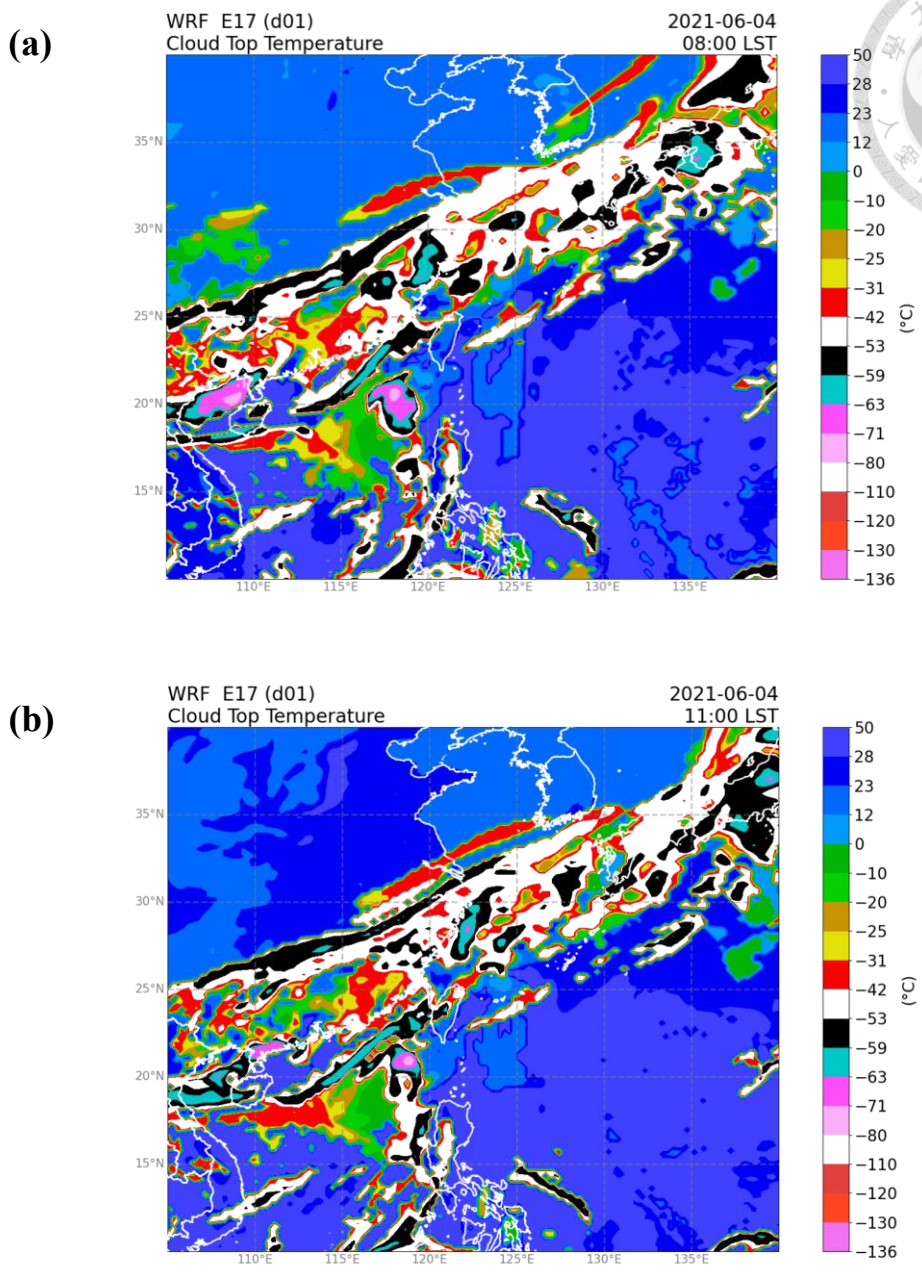
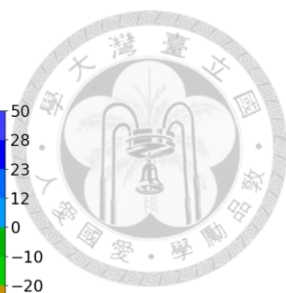


Figure 4.3 The cloud top temperature of ensemble member E17 at (a) 08 LST and (b) 11 LST.

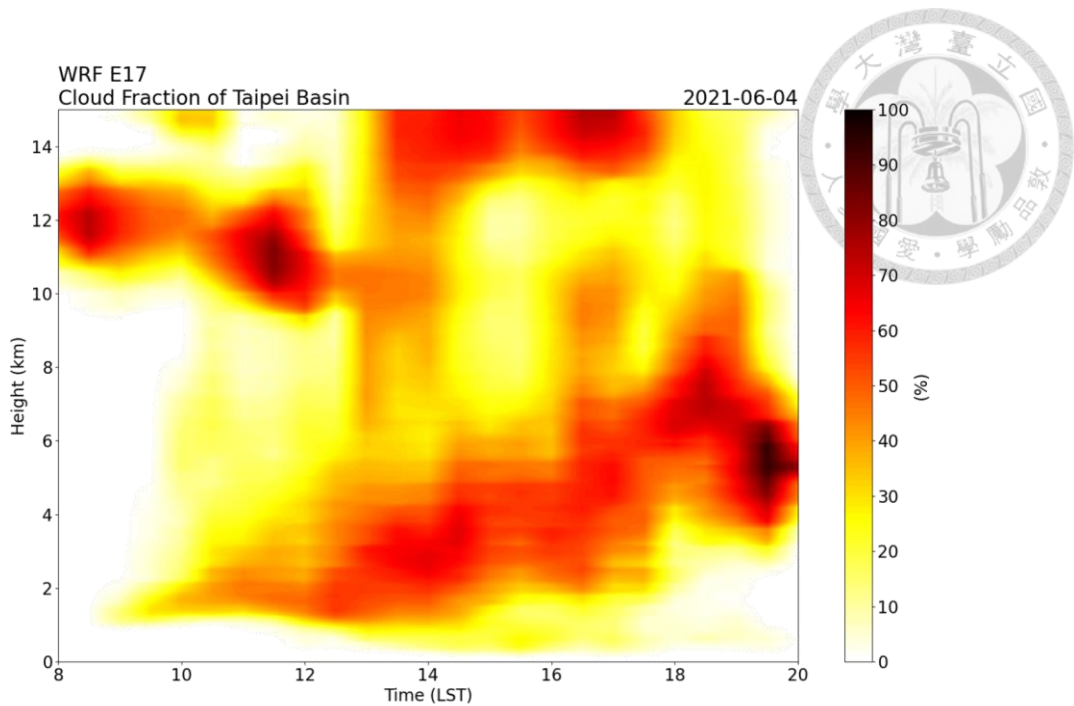


Figure 4.4 The time-height plot of the cloud fraction in ensemble member E17 over Taipei Basin.

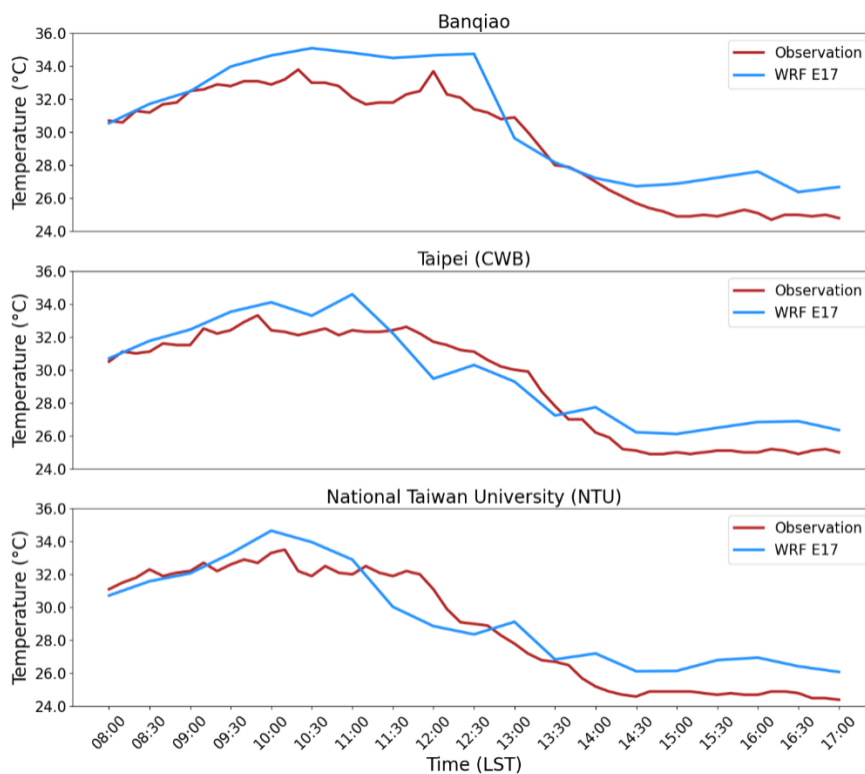


Figure 4.5 The time series of 2-m temperature from ensemble member E17 (blue) and observation (red) at three stations (Banqiao, Taipei, and National Taiwan University) in Taipei Basin from 08 LST to 17 LST.

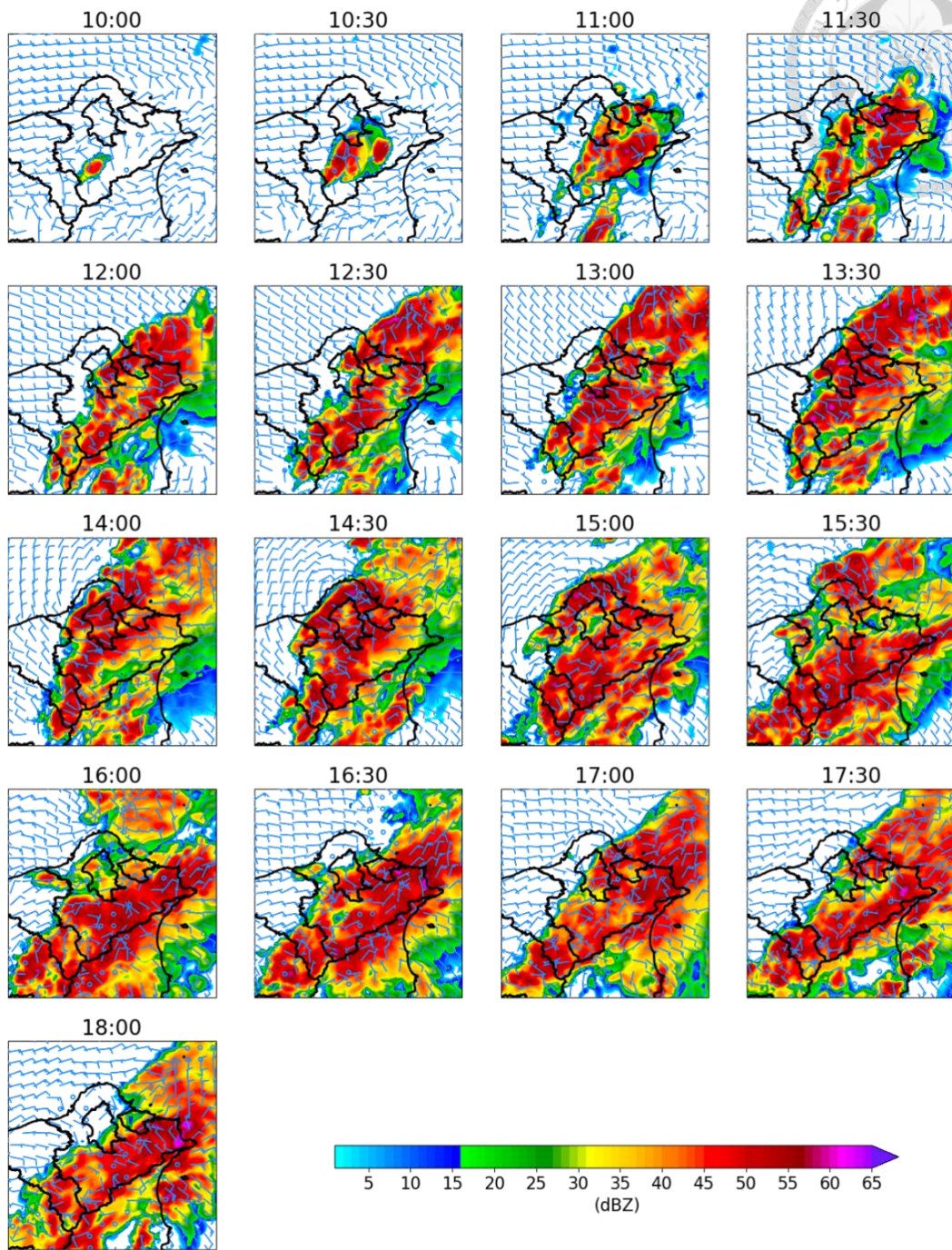


Figure 4.6 The maximum reflectivity and 10-m wind field in ensemble member E17 from 10 LST to 18 LST with 30-minute intervals.

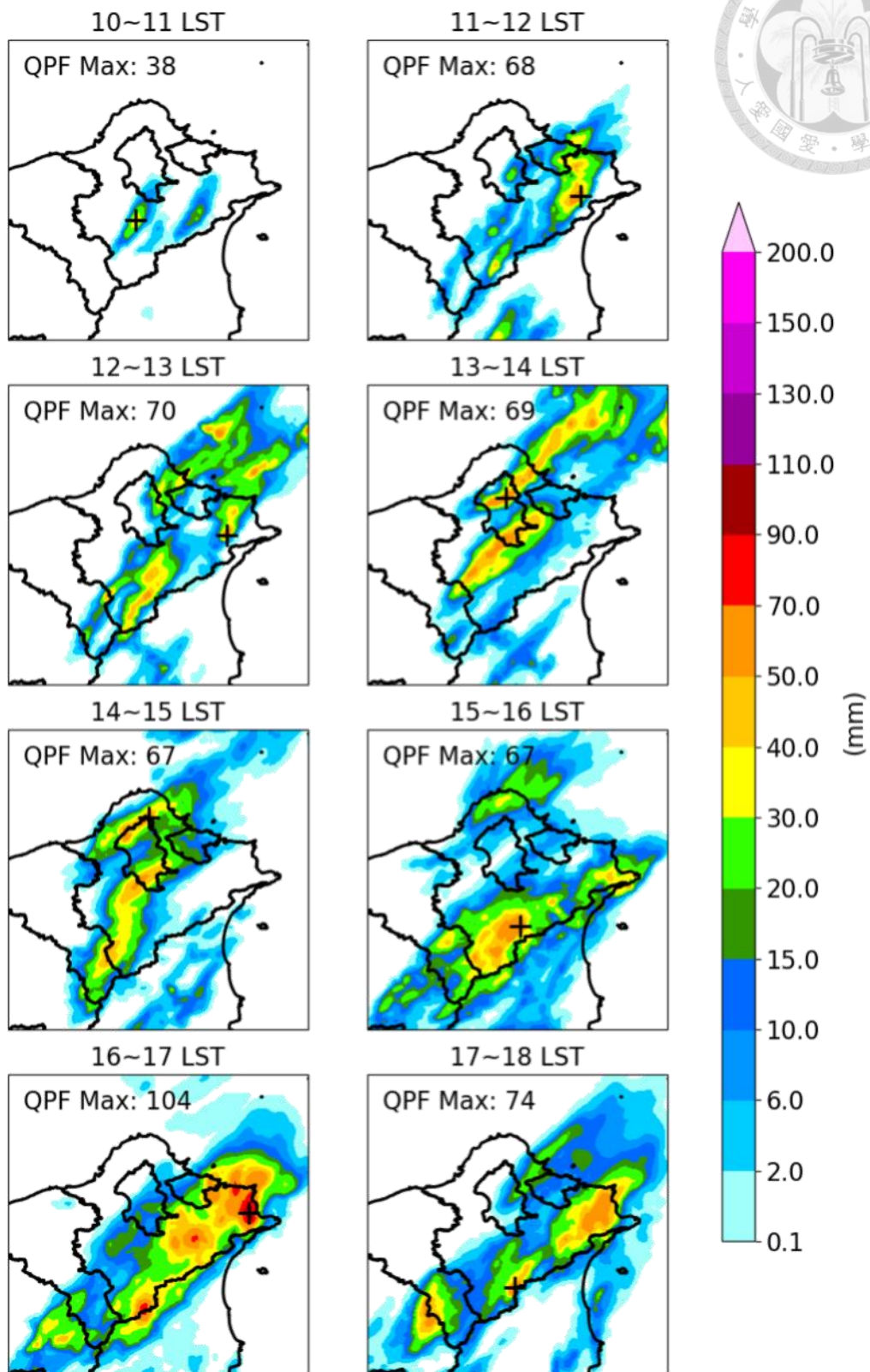


Figure 4.7 The hourly rainfall in ensemble member E17 from 10 LST to 18 LST.

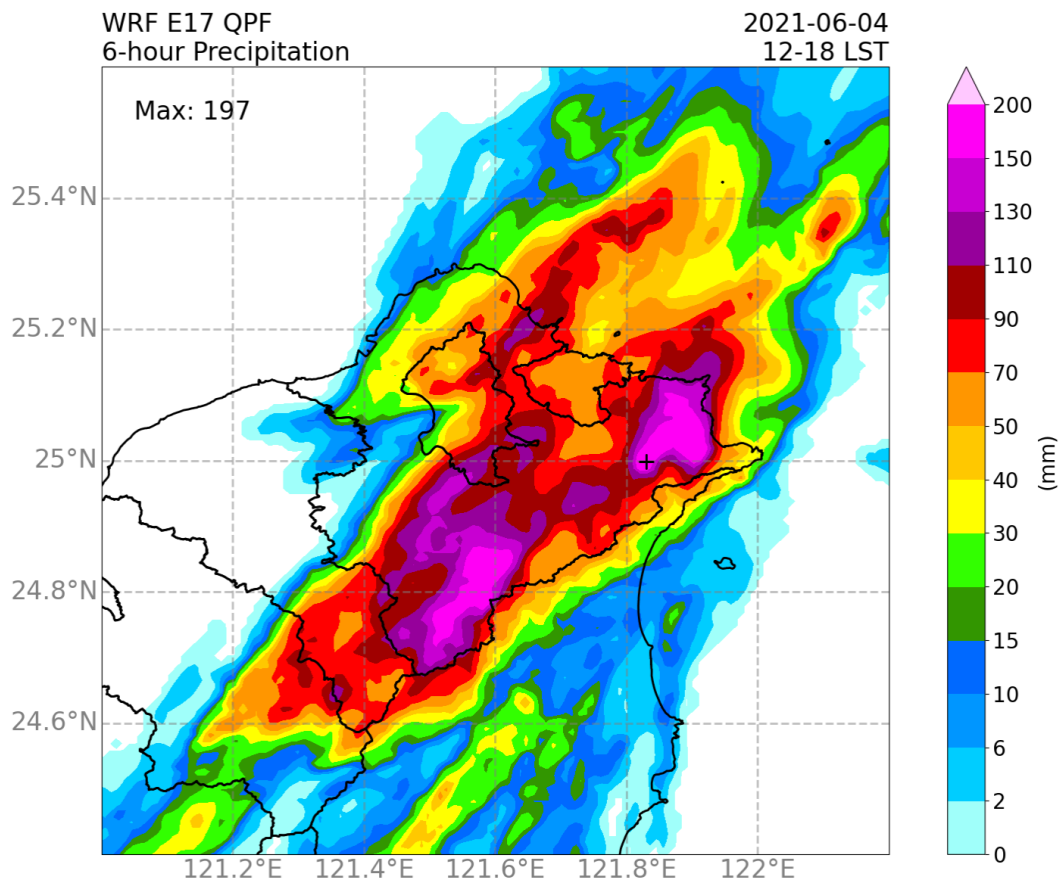


Figure 4.8 The 6-hour accumulated precipitation of ensemble member E17 from 12 LST to 18 LST.

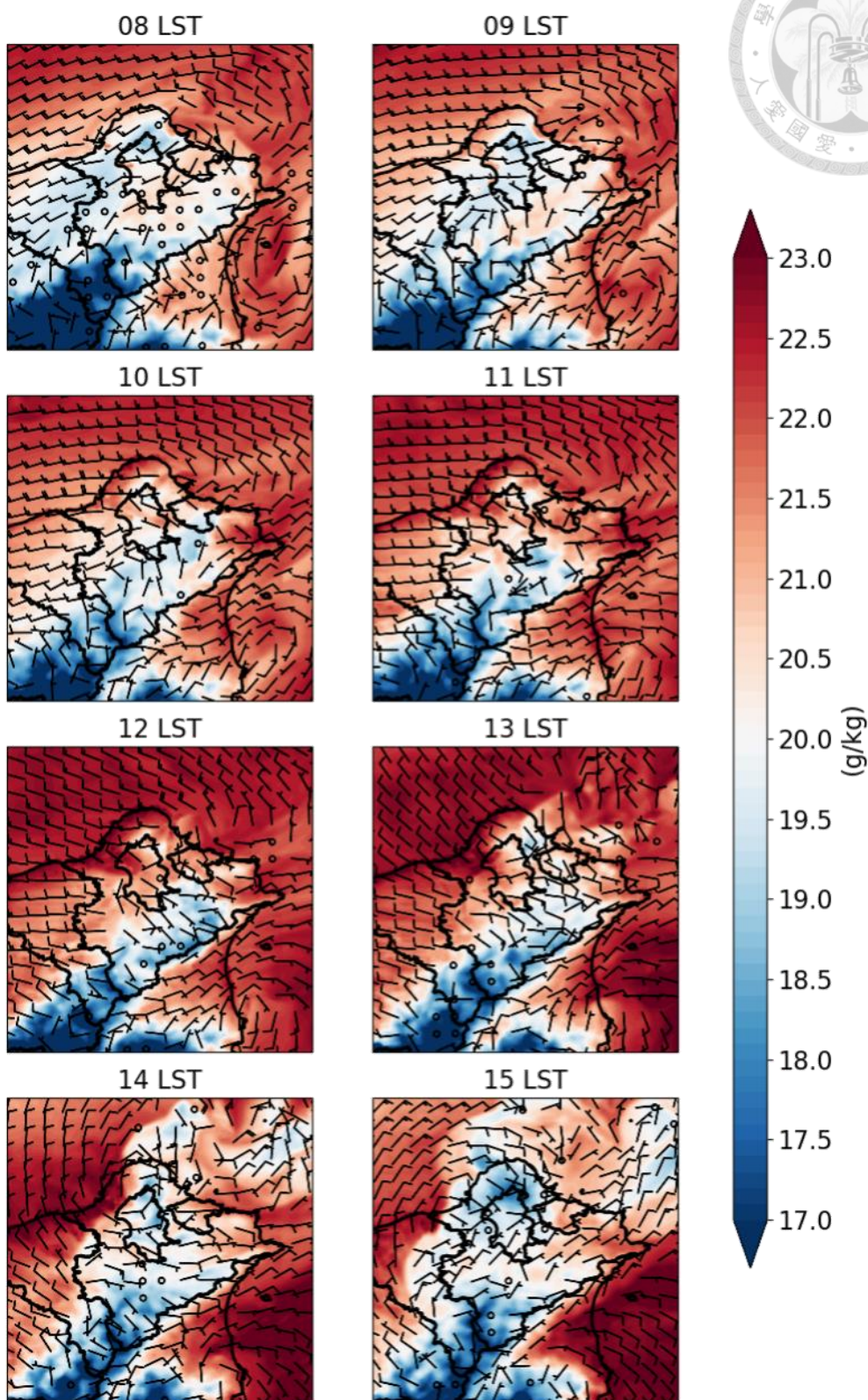


Figure 4.9 The 2-m water vapor mixing ratio (color) and 10-m wind (barbs) of ensemble member E17 from 08 LST to 15 LST with hourly intervals.

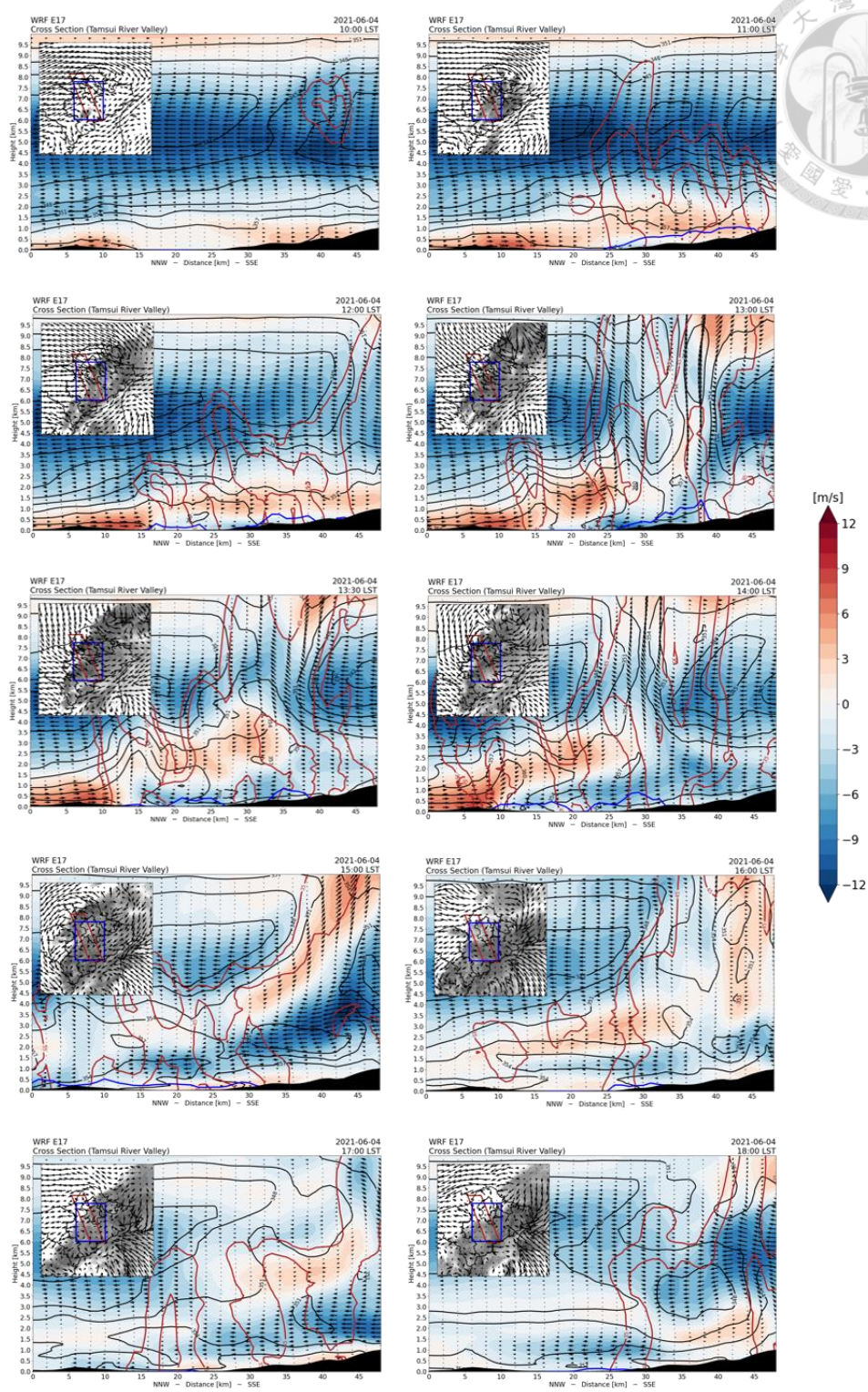
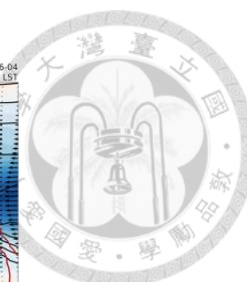


Figure 4.10 The equivalent potential temperature (black contours), wind parallel to the cross section (arrows), cold pool (blue lines), and radar reflectivity higher than 35 dBZ (red contours) along the Tamsui River Valley (TRV) from 10 LST to 18 LST. The subplots show the plain view of the 10-m wind (arrows), the radar reflectivity (shading), the area of Taipei Basin (blue box), and the cross section of TRV (red box).

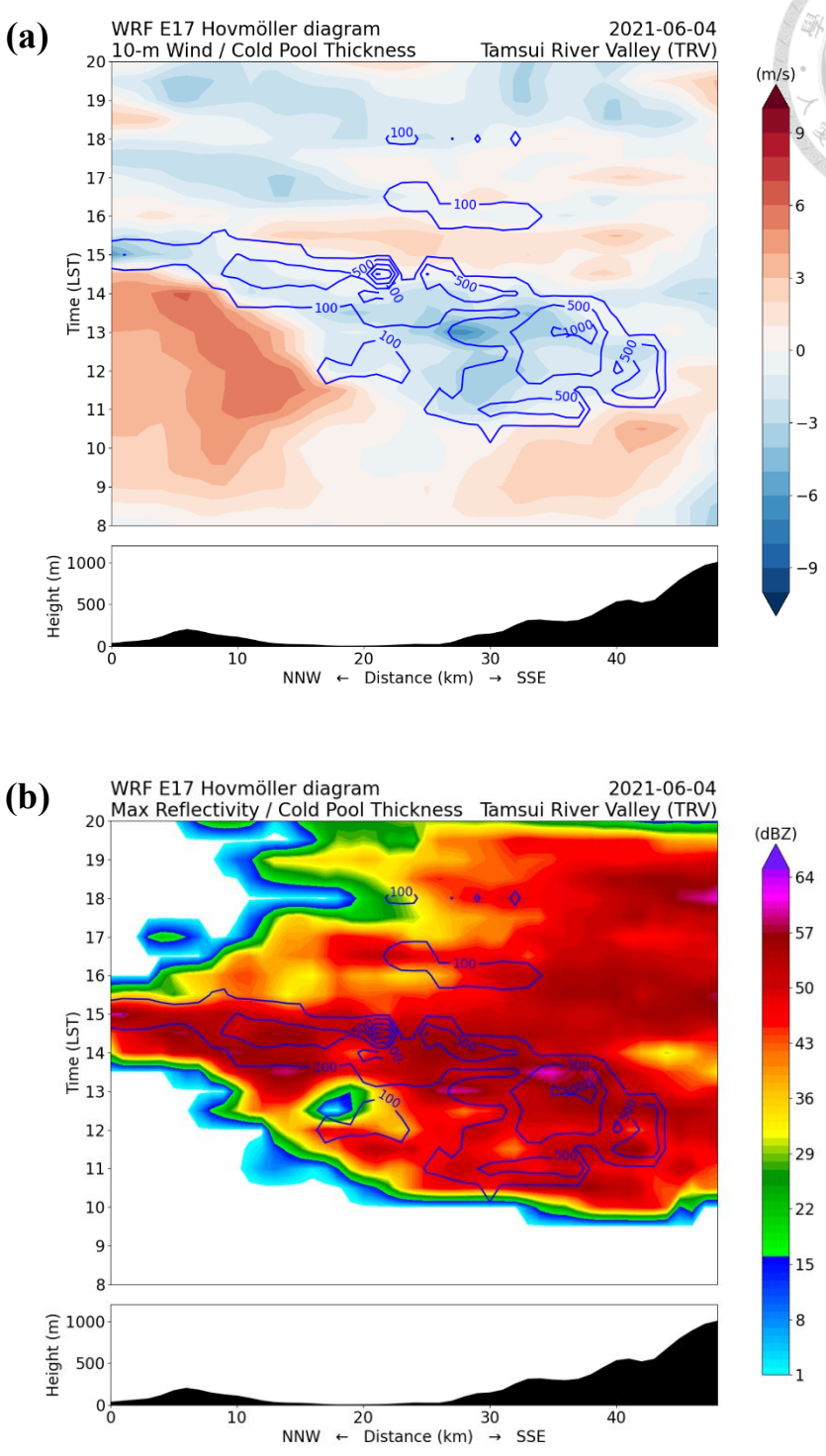
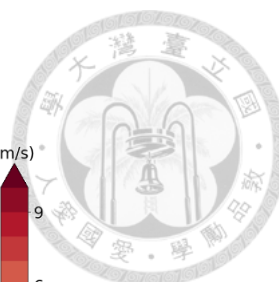


Figure 4.11 The Hovmöller diagrams of cold pool thickness (blue contours) with the color shading of (a) 10-m wind parallel to the cross section and (b) maximum radar reflectivity along the Tamsui River Valley from 08 LST to 20 LST. The subplots under each diagram show the topography.

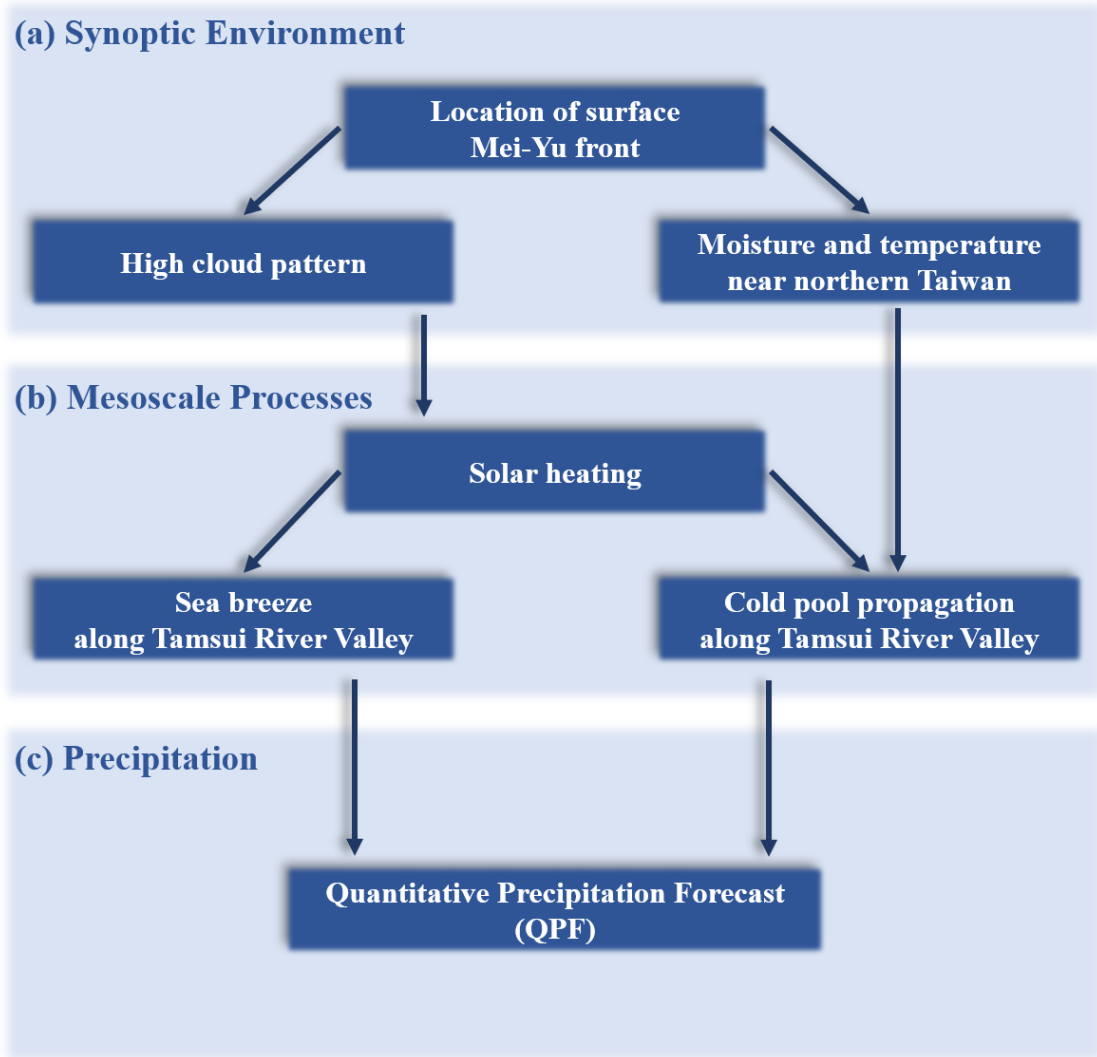


Figure 5.1 The flow chart and relationships between (a) synoptic environment, (b) mesoscale processes, and (c) precipitation in this event.

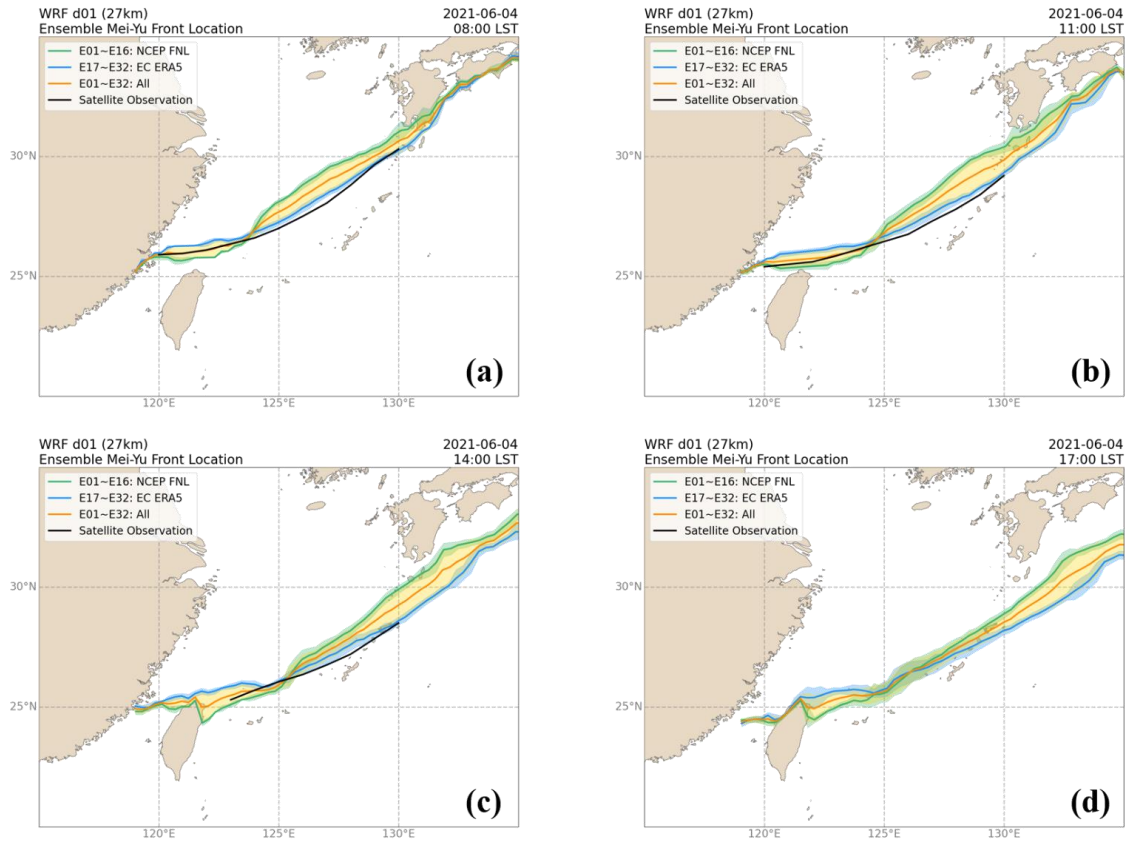


Figure 5.2 The surface Mei-Yu fronts of observation (black), NCEP members (green), ECMWF members (blue), and ensemble mean (yellow) at (a) 08 LST, (b) 11 LST, (c) 14 LST, and (d) 17 LST. The color shading shows the spread of one standard deviation.

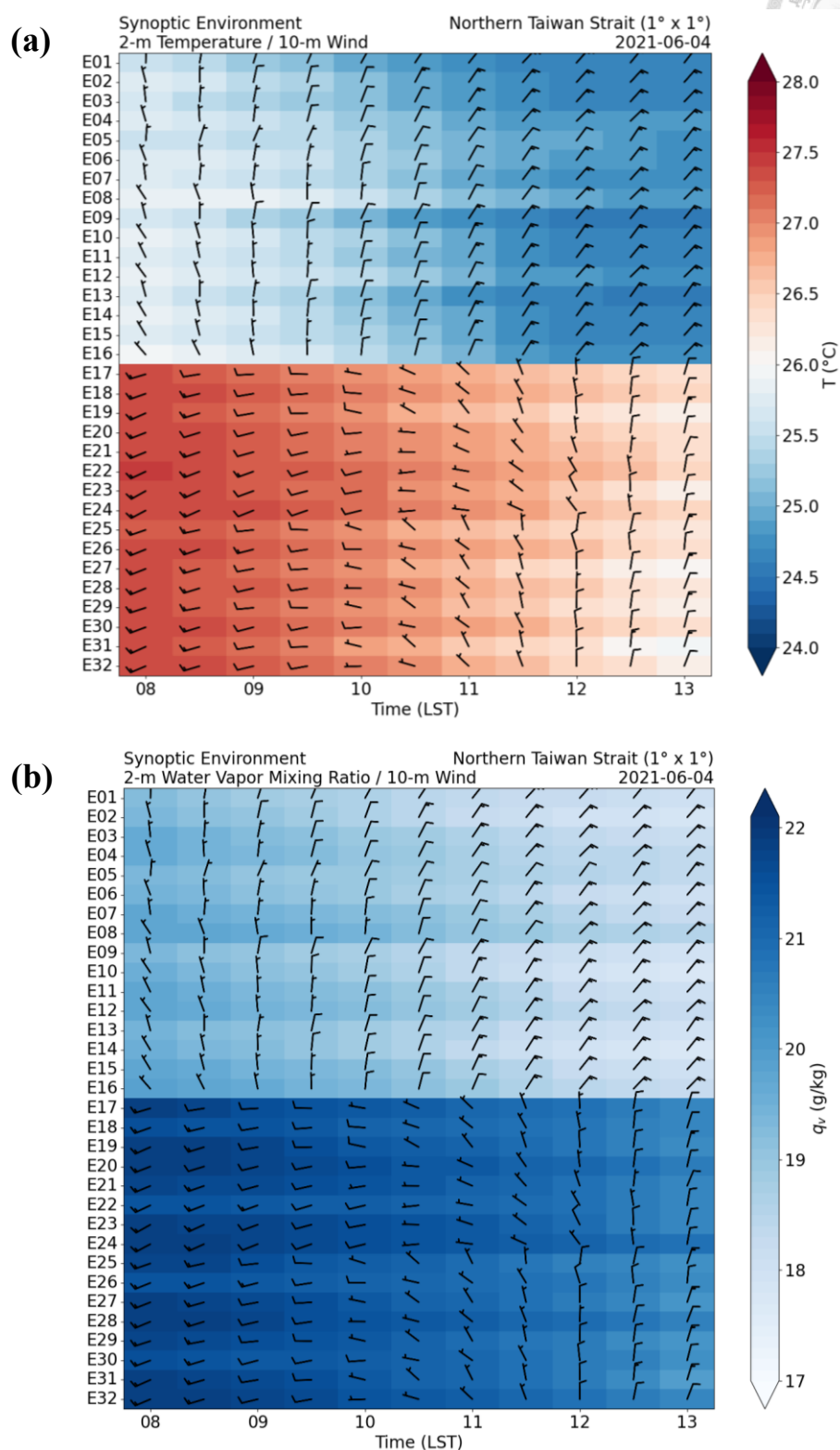
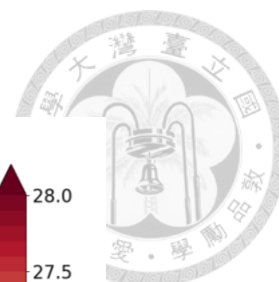


Figure 5.3 The time series of ensemble 10-m wind (barbs) with the color shading of (a) 2-m temperature and (b) 2-m water vapor mixing ratio averaged over the area of Fig. 4.2(a) from 08 LST to 13 LST.

Cloud Top Temperature
2021-06-04 08 LST

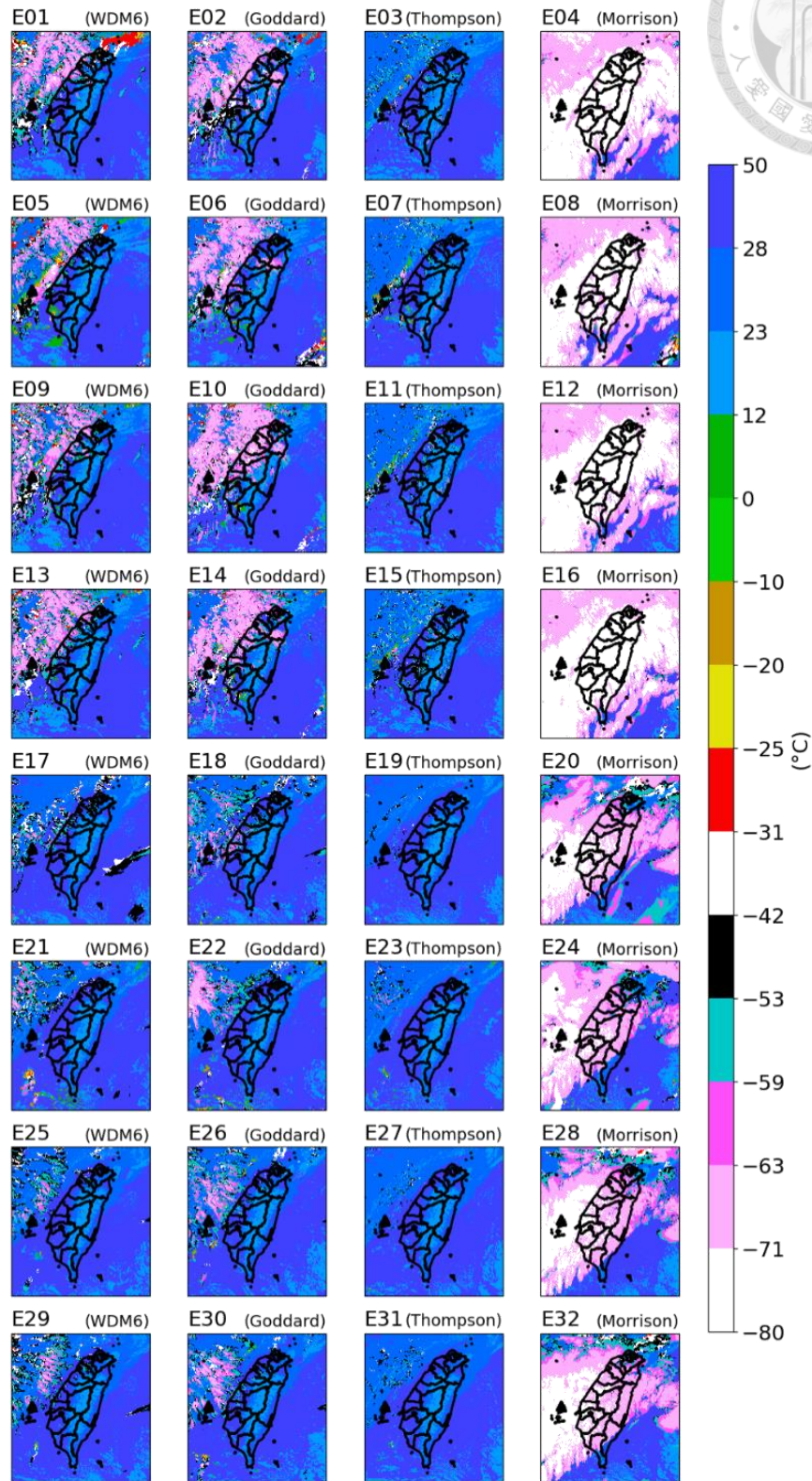


Figure 5.4 Ensemble cloud top temperature at 08 LST (00 UTC) with the microphysics scheme used in each member.

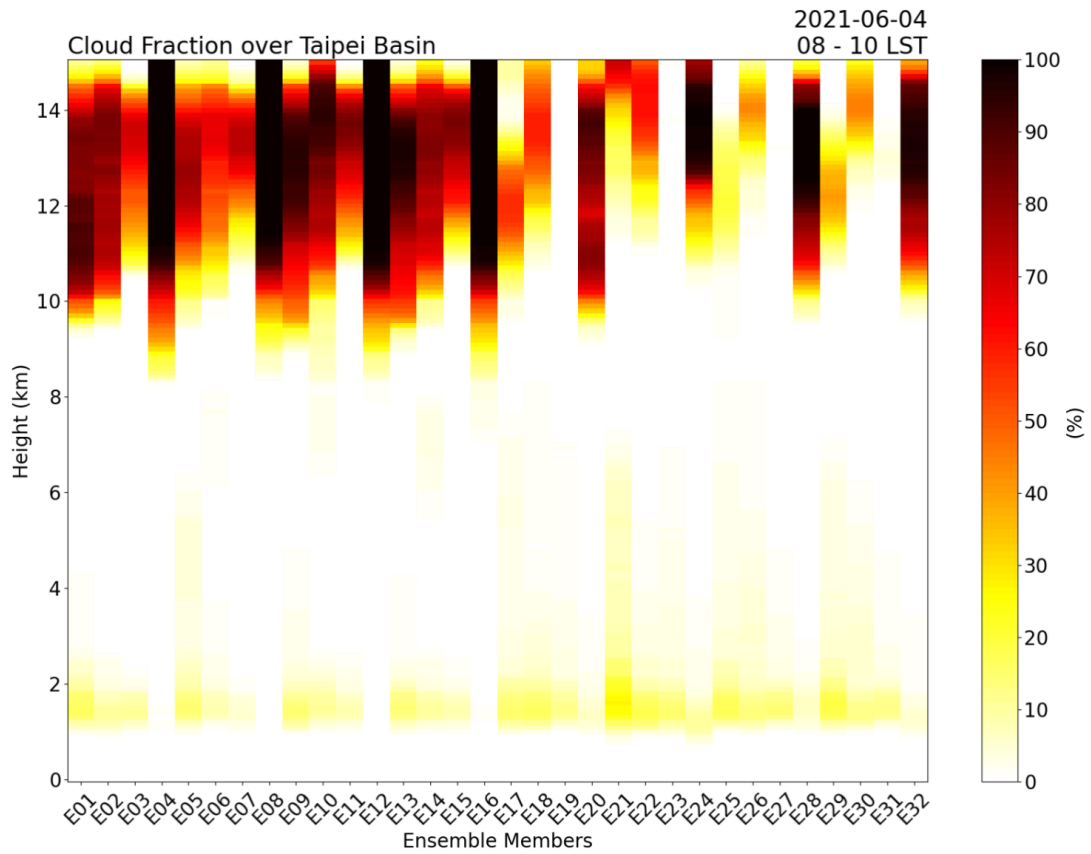


Figure 5.5 Ensemble vertical profile of averaged cloud fraction between 08 LST and 10 LST in Taipei Basin.

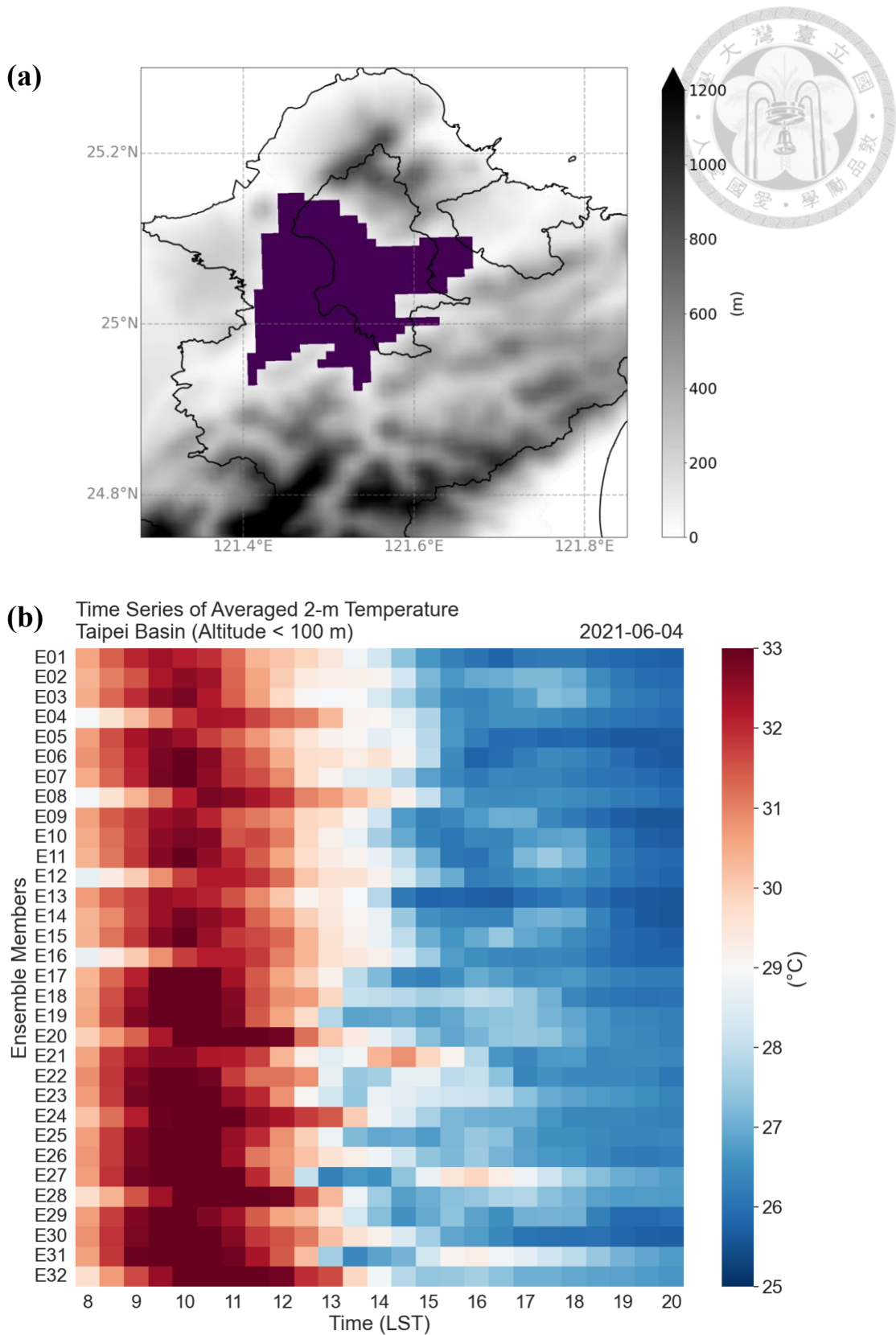


Figure 5.6 (a) The grids lower than 100 meters in Taipei Basin. (b) Ensemble time series of averaged 2-m temperature over the grids of (a) from 08 LST to 20 LST.

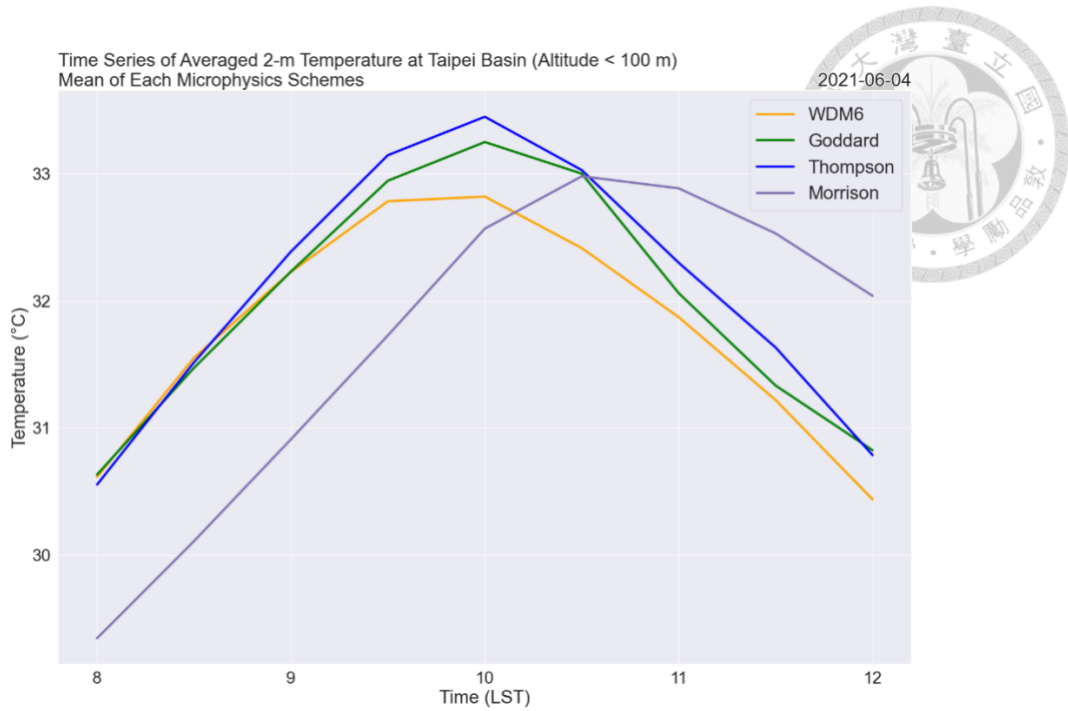


Figure 5.7 The time series of averaged 2-m temperature in the members of WDM6 (yellow), Goddard (green), Thompson (blue), and Morrison (purple) microphysics schemes. The domain is the same as **Fig. 5.6 (a)**.

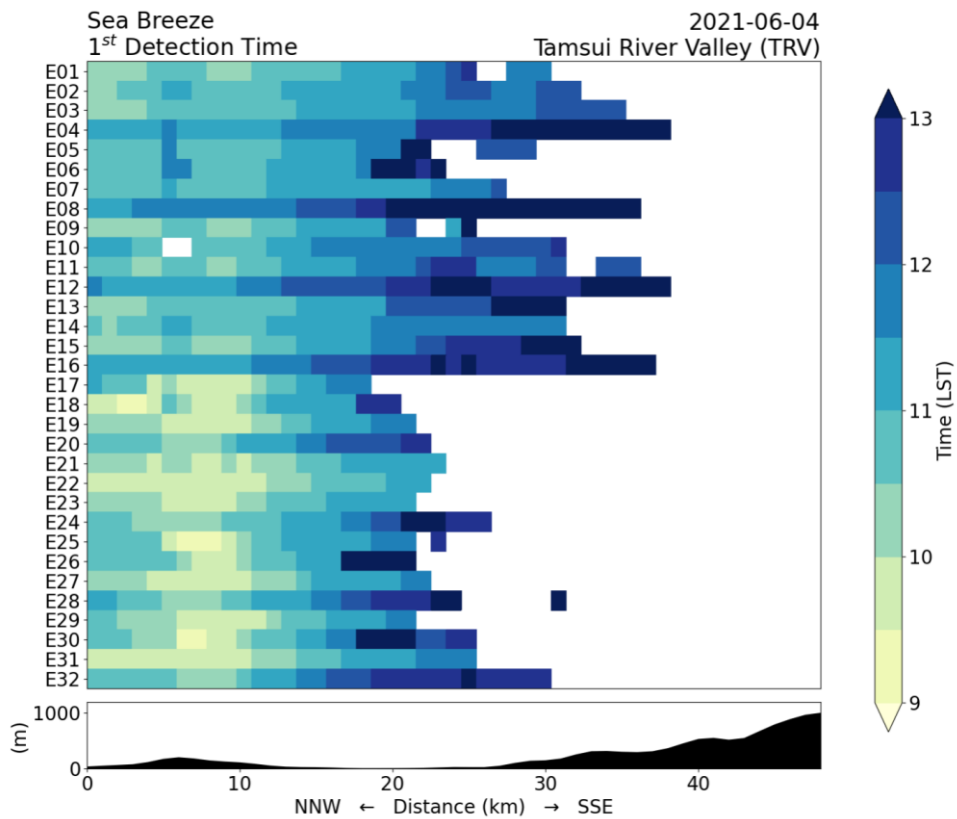


Figure 5.8 The first detection time of sea breeze along the TRV in each member.

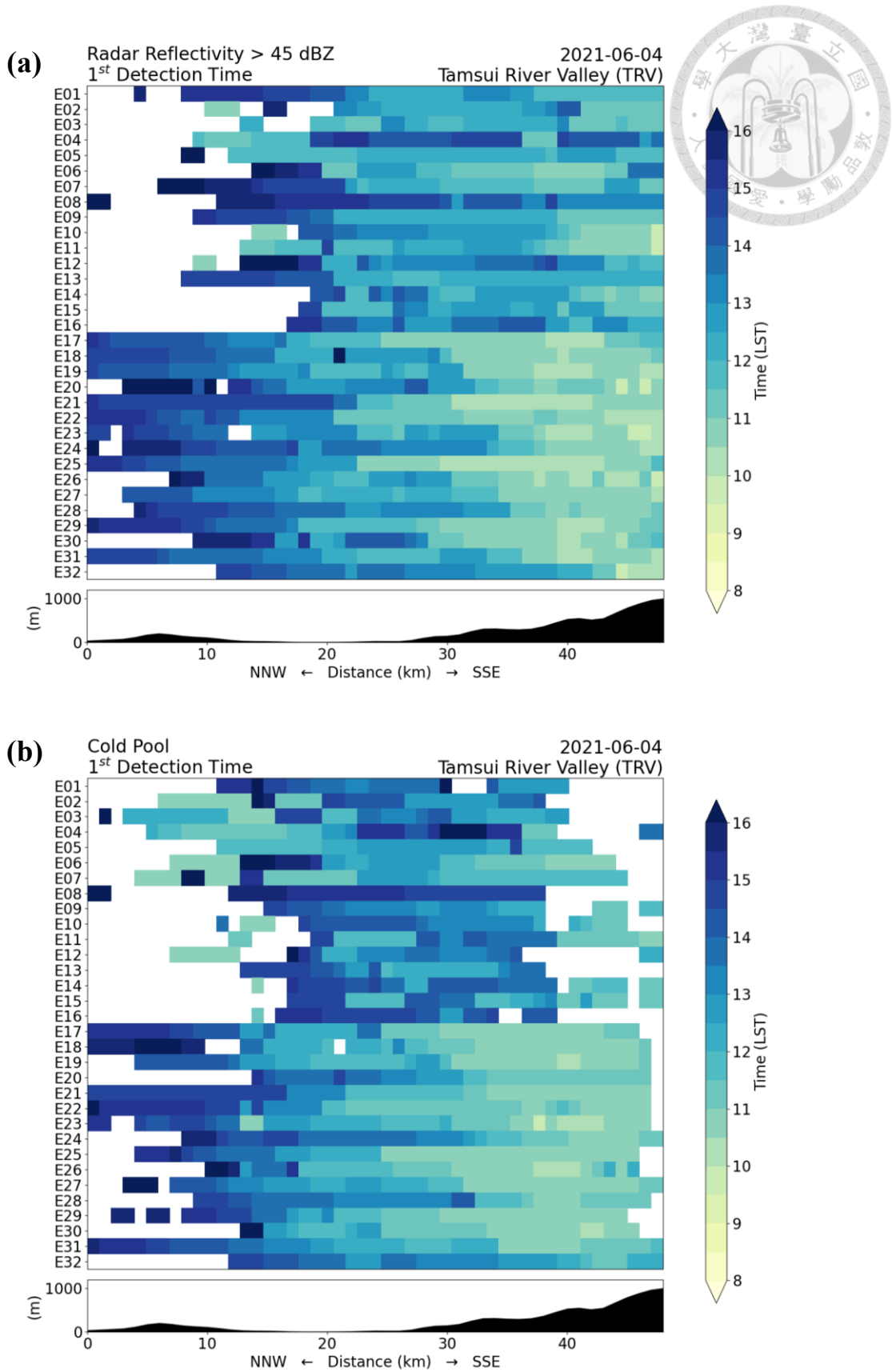


Figure 5.9 The first detection time of (a) the convective cell (>45 dBZ) and (b) the induced thunderstorm cold pool along TRV in each member.

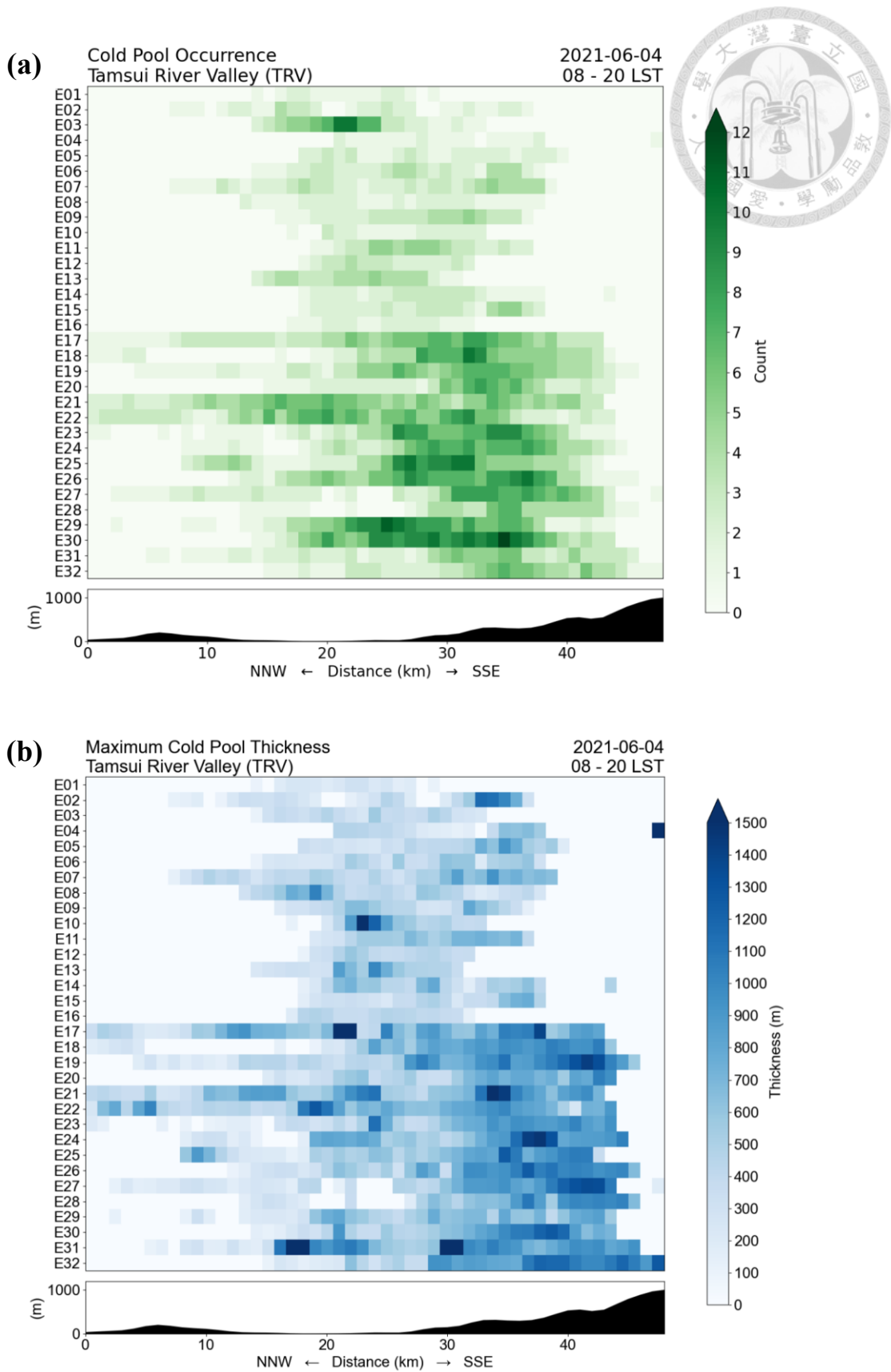


Figure 5.10 (a) The occurrence of cold pool (detected every 30 minutes) and (b) the maximum cold pool thickness along TRV between 08 LST and 20 LST.

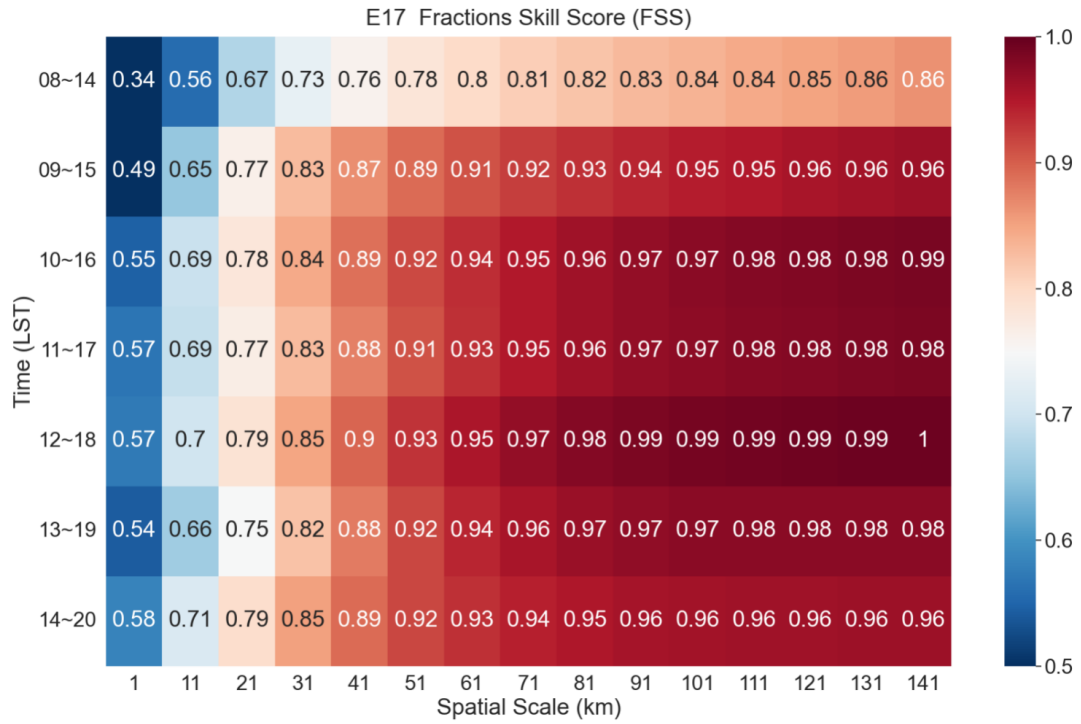


Figure 6.1 The FSS of 6-hour rainfall in E17 from 08 LST to 20 LST under the threshold of 30 mm/6hr and the spatial scale of 1 km to 141 km.

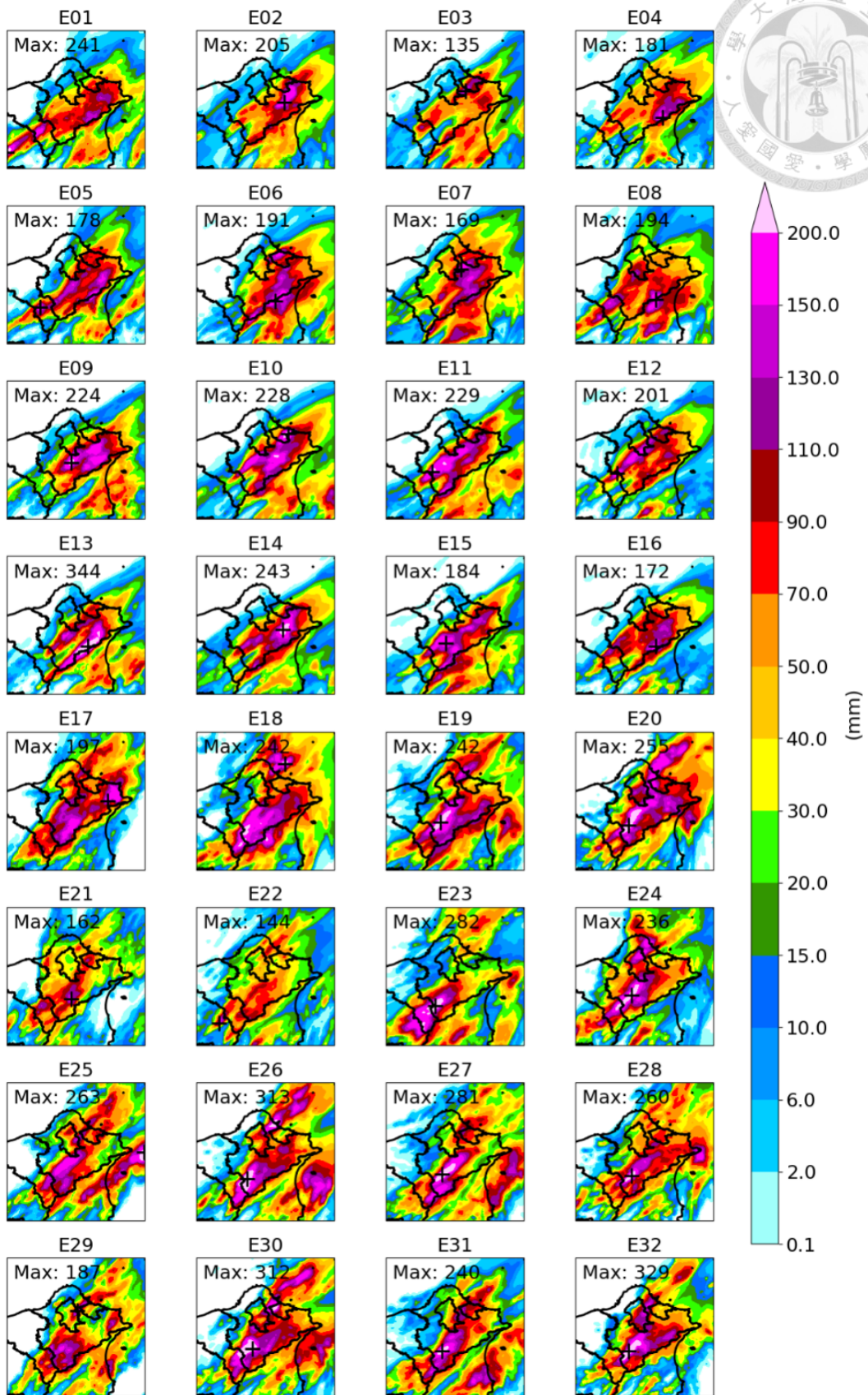


Figure 6.2 Ensemble 6-hour precipitation from 12 LST to 18 LST.

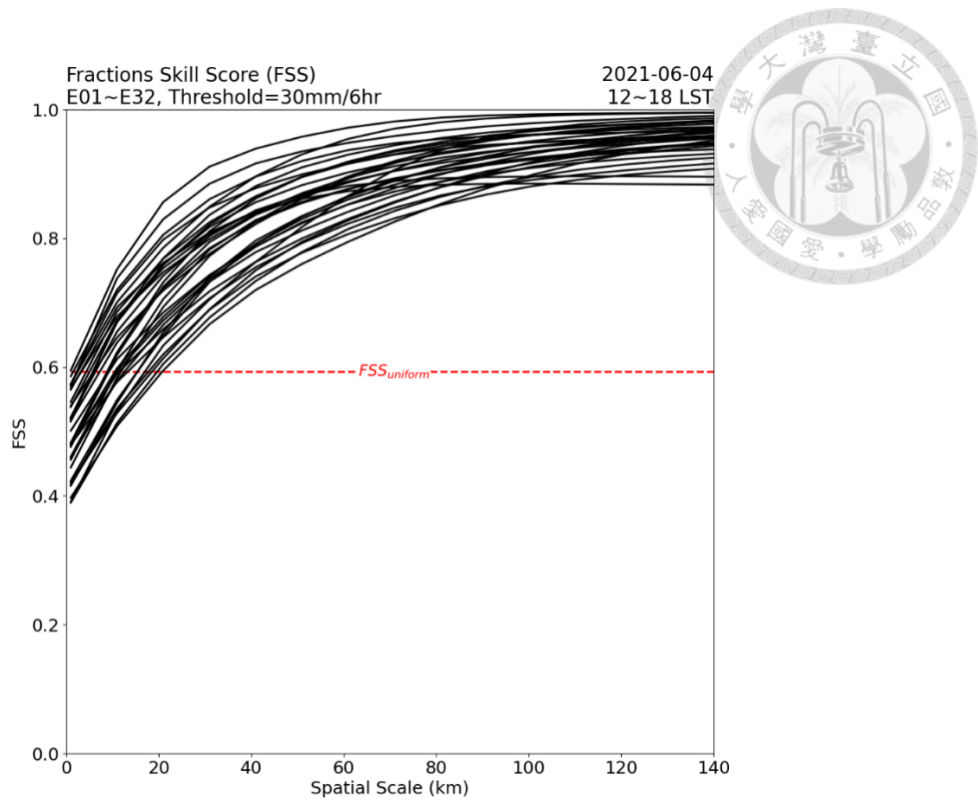


Figure 6.3 Ensemble FSS curves and the corresponding $FSS_{uniform}$ (0.59) for the 6-hour precipitation between 12 LST and 18 LST under the threshold of 30 mm/6hr.

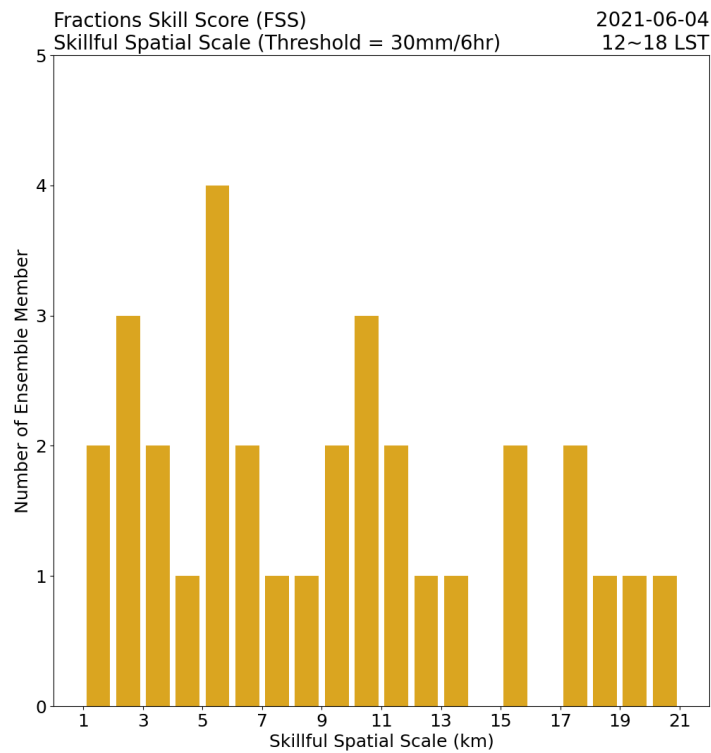


Figure 6.4 The histogram of skillful spatial scales in 32 ensemble members between 12 LST and 18 LST under the threshold of 30 mm/6hr.

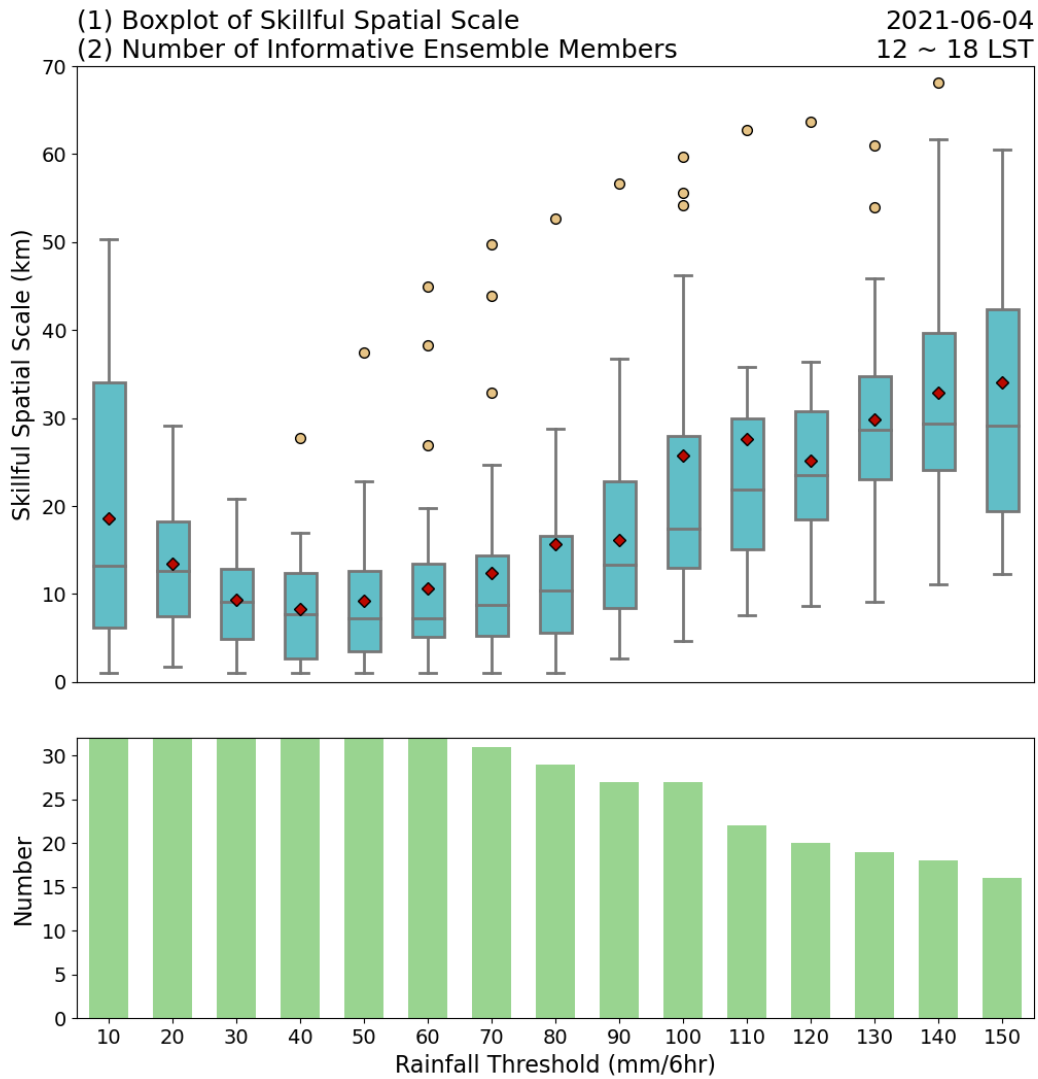


Figure 6.5 The box plot of skillful spatial scale (top) and the number of members (bottom) that can achieve the FSS_{uniform} under different rainfall thresholds (mm/6hr). The red diamonds in the boxplot represent the mean value, and the yellow dots are the outliers.

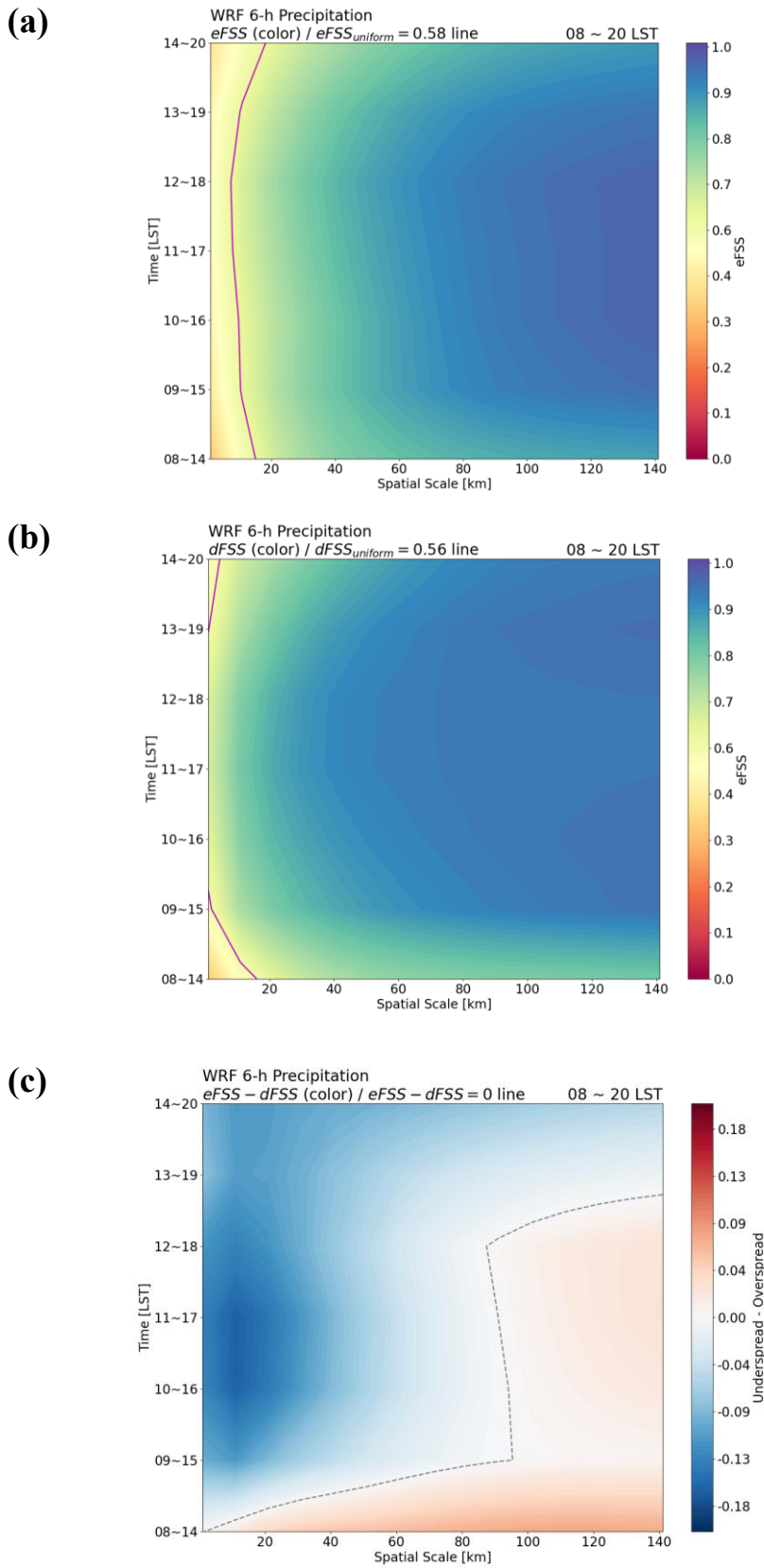


Figure 6.6 The (a) eFSS, (b) dFSS, and (c) eFSS – dFSS of the 6-hour accumulated precipitation from 08 LST to 20 LST under the threshold of 30 mm/6hr.

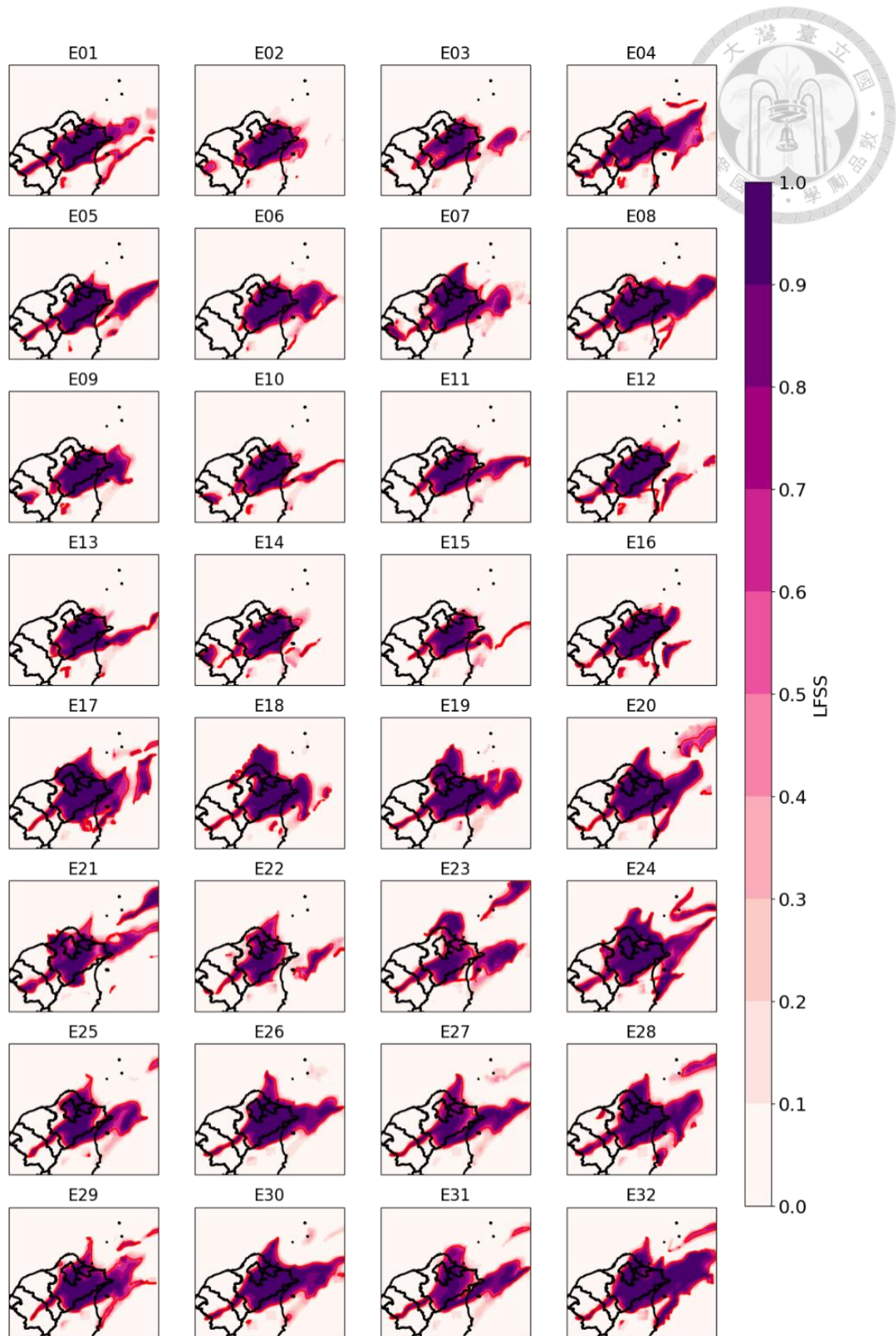


Figure 6.7 The ensemble LFSS of 6-hour accumulated precipitation from 08 LST to 20 LST under the threshold of 30 mm/6hr.

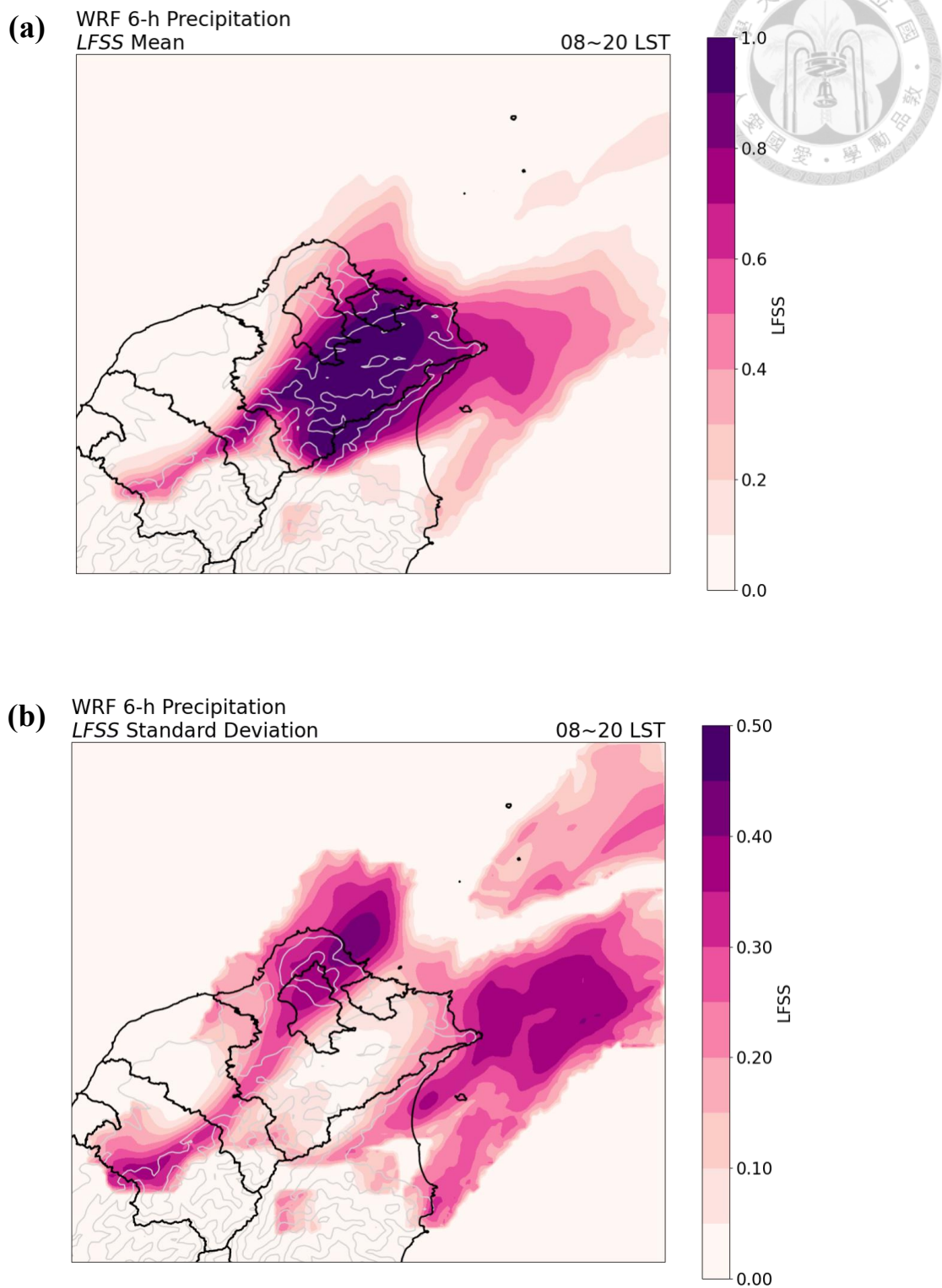


Figure 6.8 The (a) mean value and (b) standard deviation of the LFSS for the 6-hour accumulated precipitation from 08 LST to 20 LST under the threshold of 30 mm/6hr.



Method for Object-Based Diagnostic Evaluation (MODE)
Matching Type of Observation Field

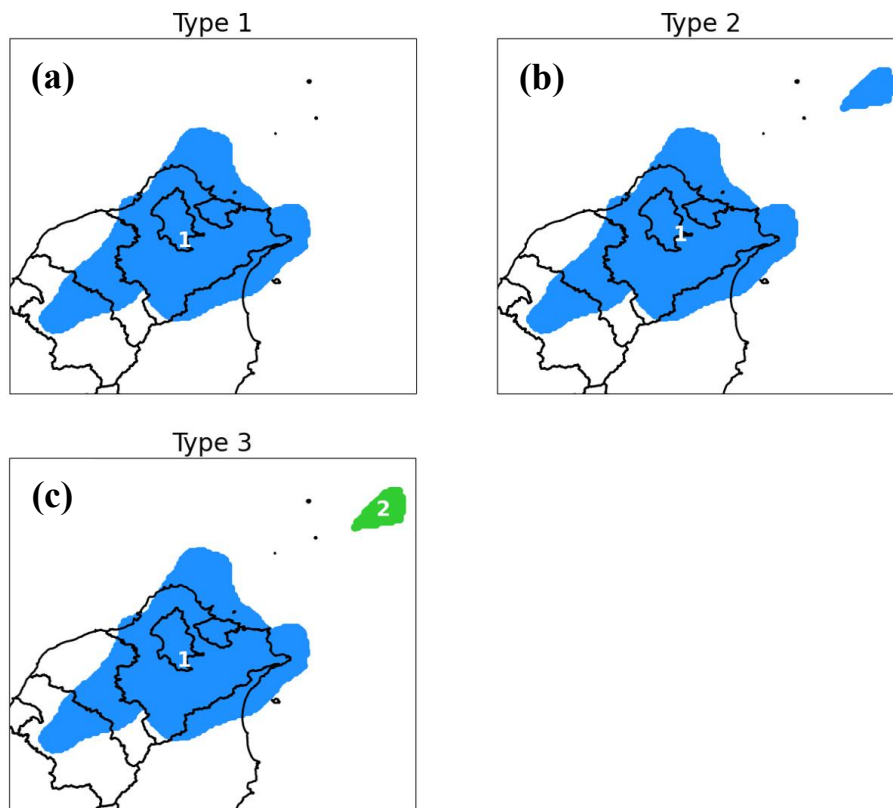


Figure 6.9 Three matching types of the MODE method for the 6-hour observational rainfall from 12 LST to 18 LST.

Method for Object-Based Diagnostic Evaluation (MODE)
 Matching Results of WRF Members

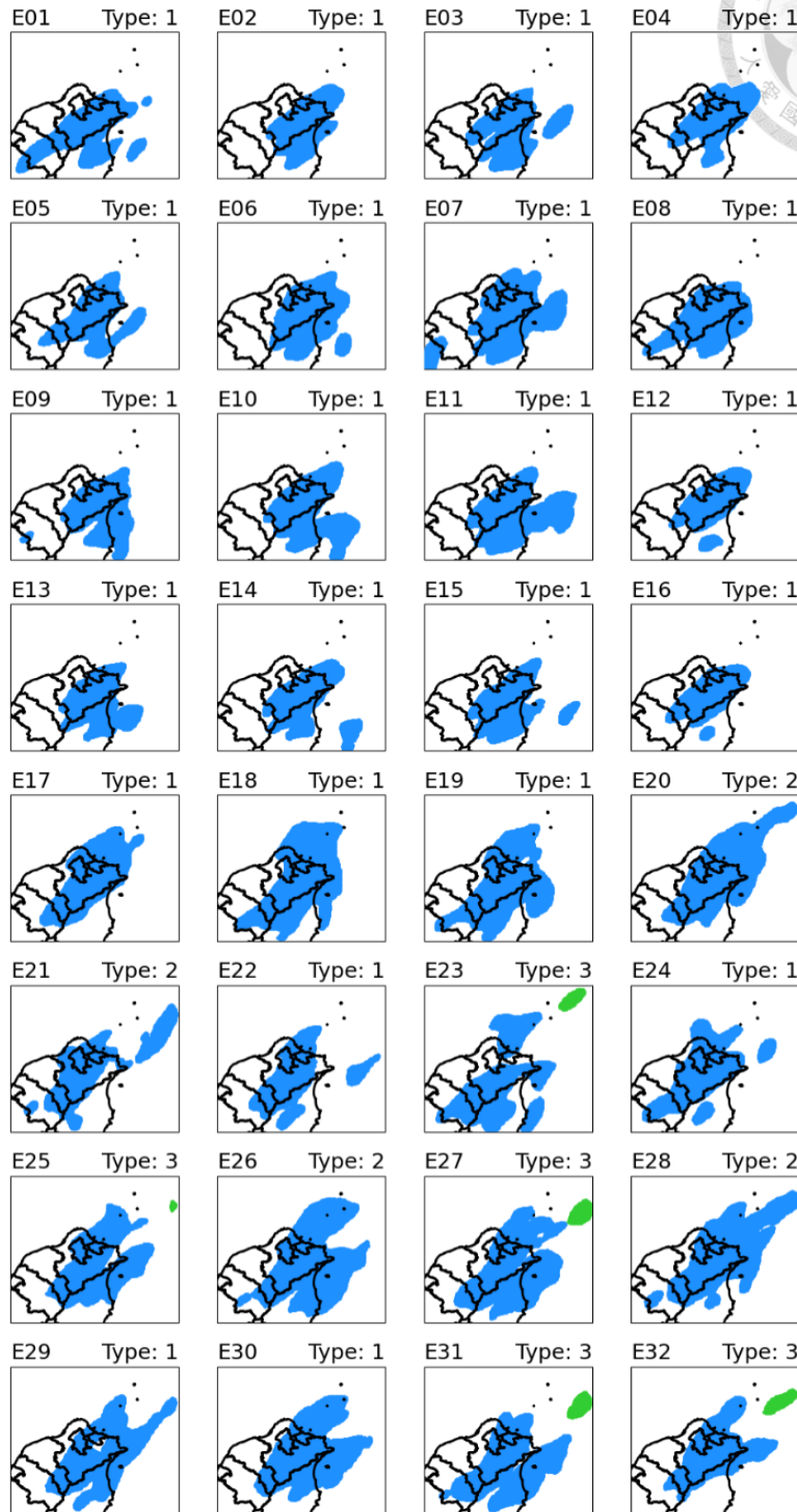
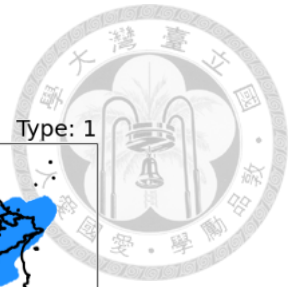


Figure 6.10 The ensemble matching results of the MODE method for the 6-hour rainfall from 12 LST to 18 LST.

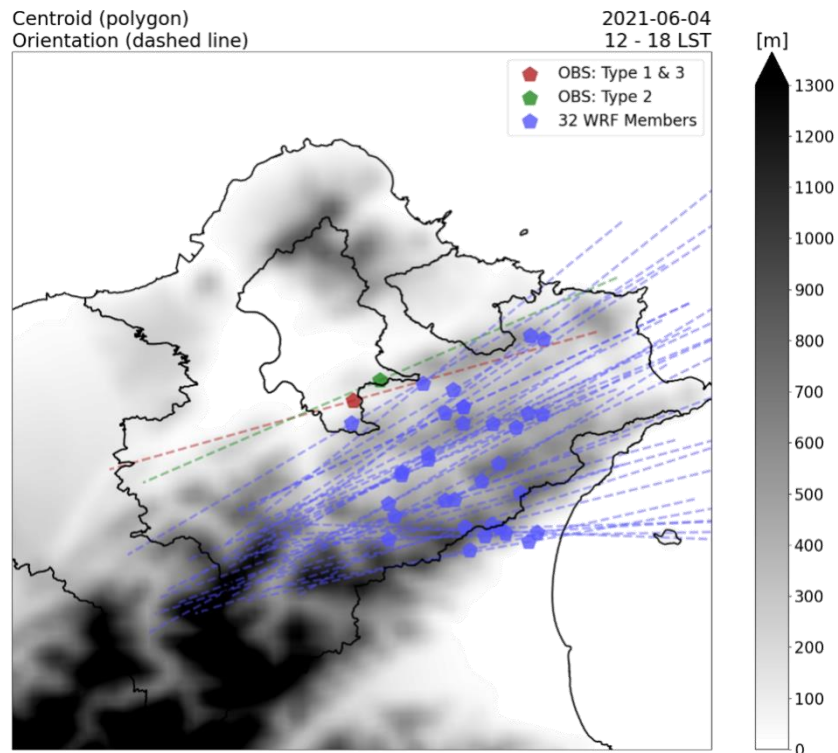


Figure 6.11 The centroids and the corresponding orientation of the observational and forecasted rainfall areas from the MODE method.



QPF Error Verified by MODE
(Location, Size, and Orientation)

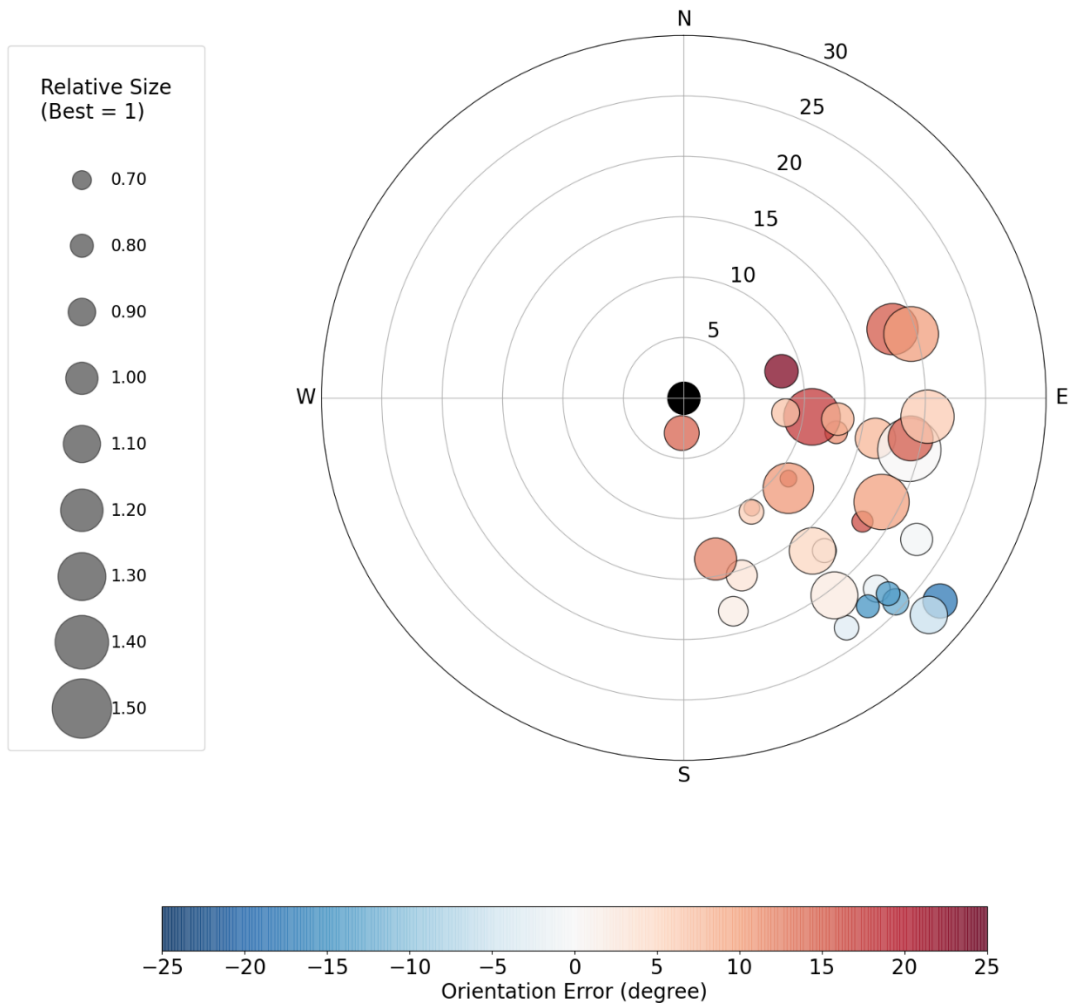


Figure 6.12 Four kinds of geometric bias evaluated by the MODE method. The black dot at the origin represents the observation.

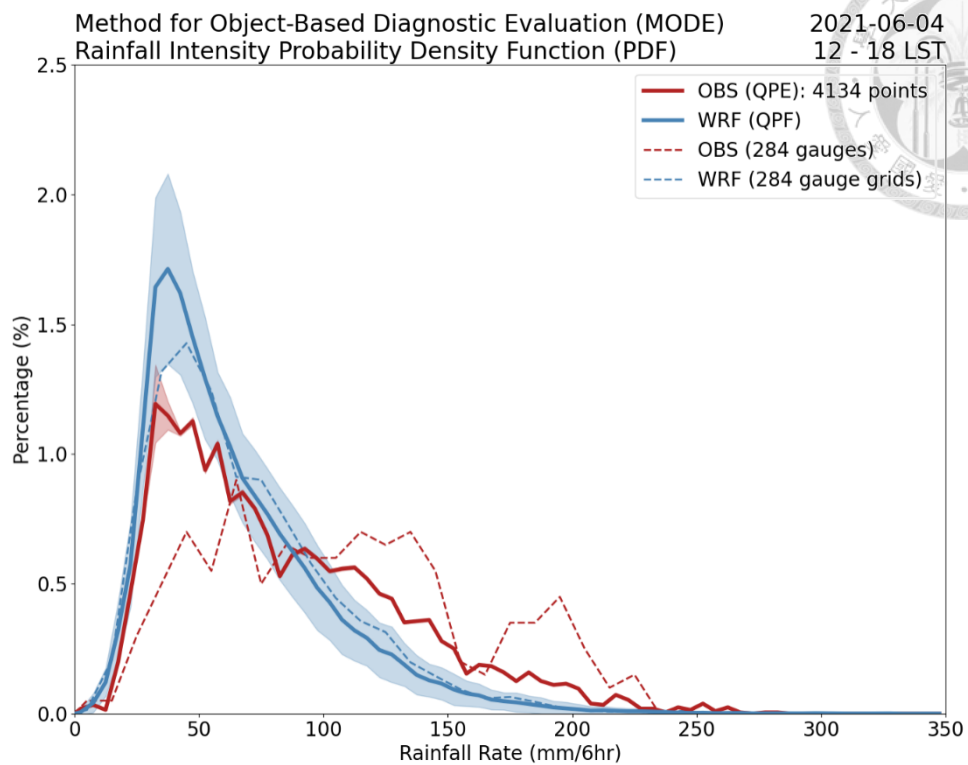


Figure 6.13 The probability density function of the rainfall intensity from gauge-corrected QPE (red solid), gauge data (red dashed), ensemble QPF (blue solid), and the gauge-grid data of the ensemble members (blue dashed). The color shading shows the spread of one standard deviation.

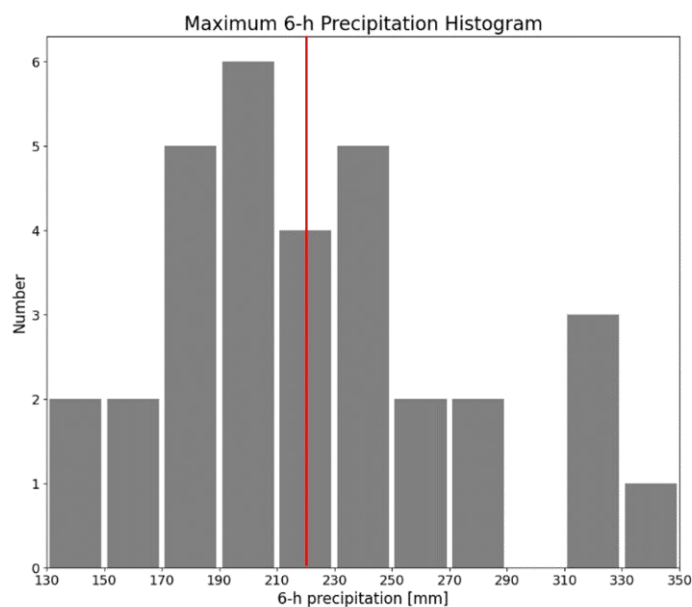


Figure 6.14 The histogram of the forecasted maximum 6-hour accumulated precipitation from 12 LST to 18 LST. The red line is the observational maximum.

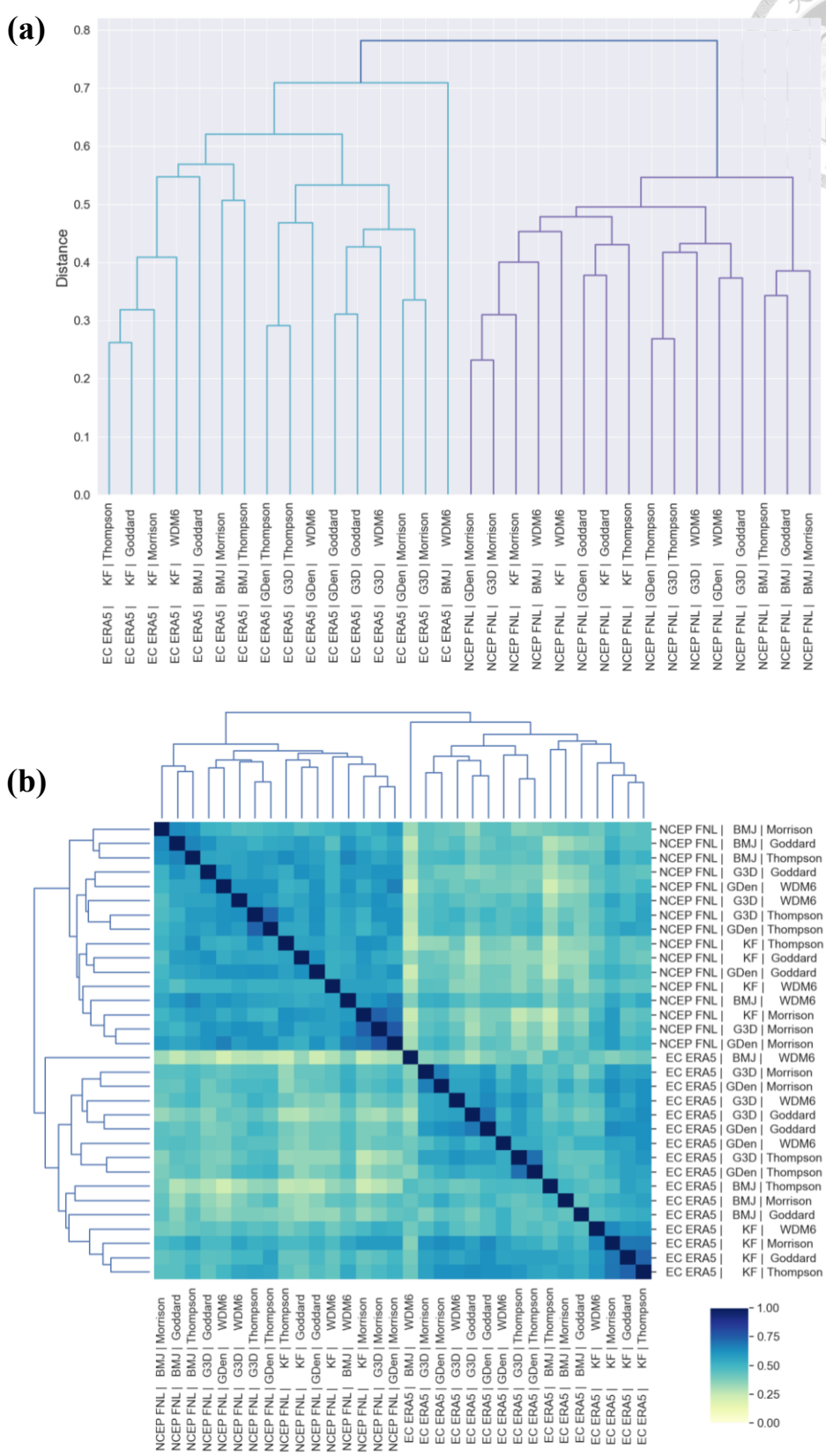


Figure 6.15 The (a) dendrogram and (b) the correlation coefficient matrix from the hierarchical clustering of 6-hour accumulated precipitation from 12 LST to 18 LST.

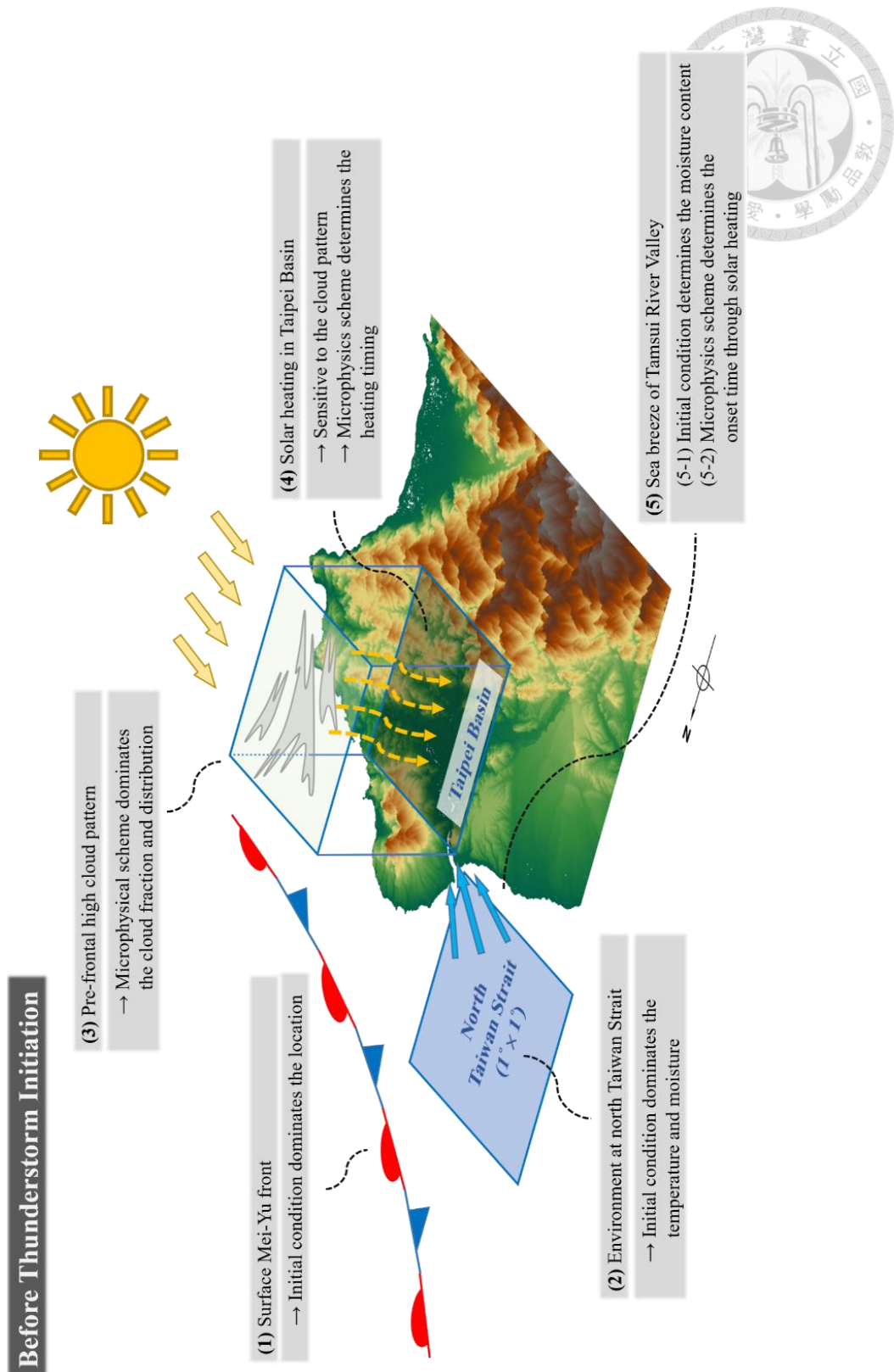


Figure 7.1 The schematic diagram of the physical mechanisms and the factors causing ensemble diversities on the environment before thunderstorm initiation.

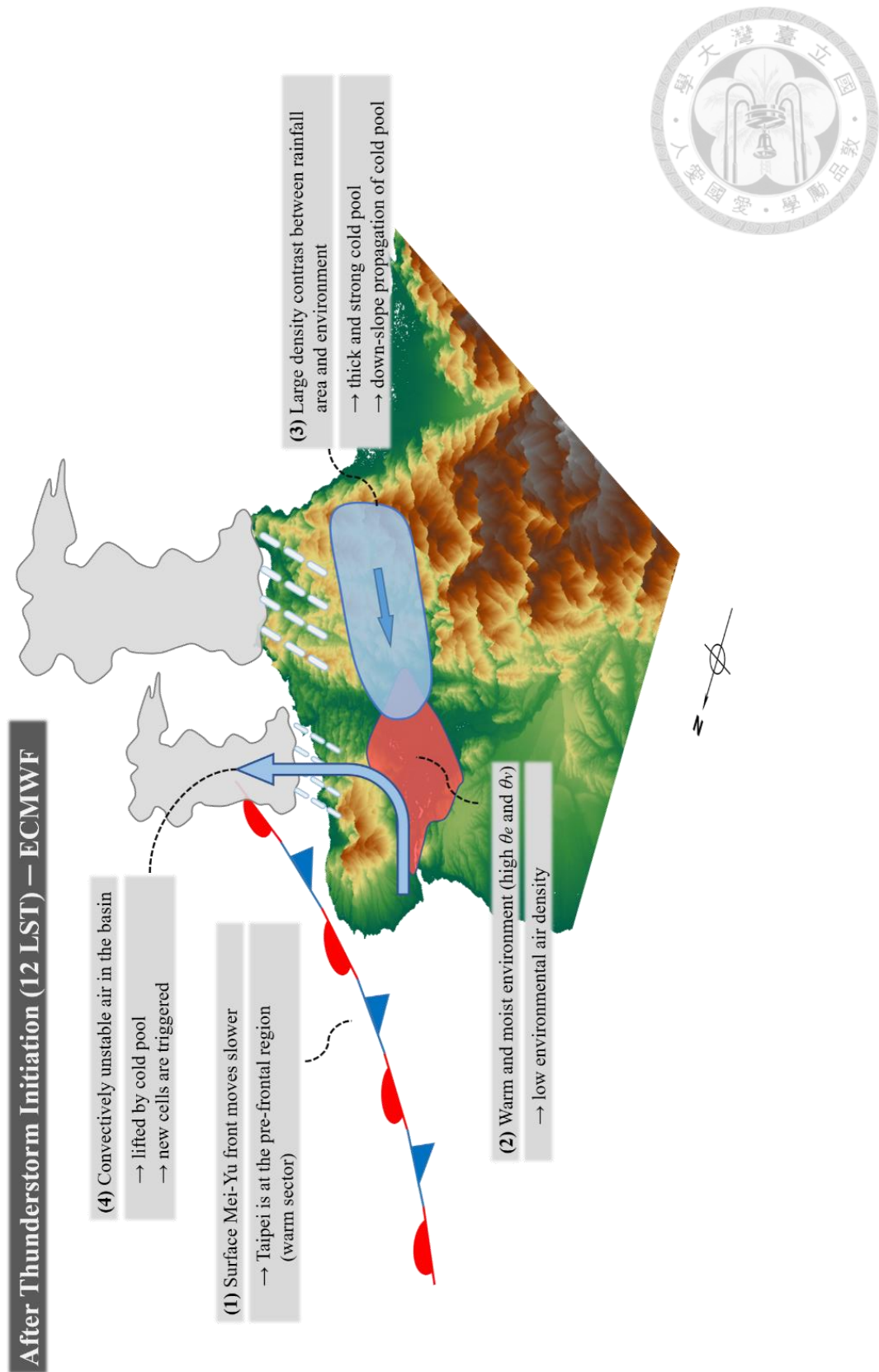


Figure 7.2 The schematic diagram of the thunderstorm development and the factors causing ensemble diversities in the ECMWF members.

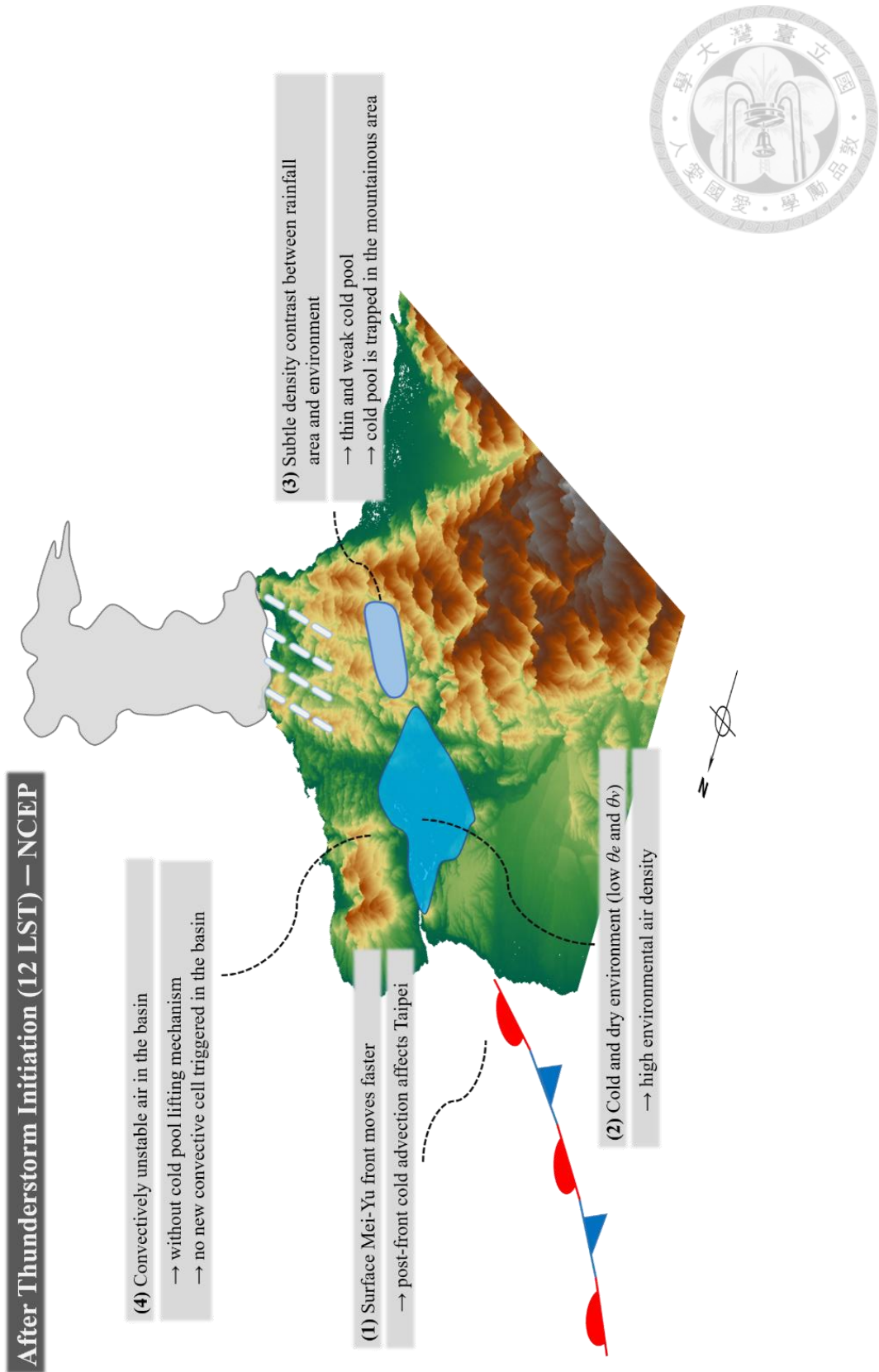


Figure 7.3 The schematic diagram of the thunderstorm development and the factors causing ensemble diversities in the NCEP members.